Ekman currents caused by variable wind in models of upper ocean with depth and time dependent eddy viscosity

Rema Bashir Almelah

Submitted in partial fulfilment of the requirements of the degree of Doctor of Philosophy

Keele University
School of Computing and Mathematics

December 2018

I certify that this thesis submitted for the degree of Doctor of Philosophy is the result of my own research, except where otherwise acknowledged, and that this thesis has not been submitted for a higher degree to any other university or institution.

Acknowledgements

I would like to acknowledge and express my deep gratitude and appreciation to my supervisor Prof Victor Shrira for his patience, advice, guidance and persistent help until this work came to existence.

I would like to acknowledge my gratitude to Prof Jonathan Healey and Dr Sergei Annenkov for their creative and comprehensive advice.

I would like to express my deep gratitude to all members who I interacted with in School of Computing and Mathematics as well as the technical support team and student support team for their generous and persistent help.

I am deeply grateful and would like to acknowledge my gratitude to my beloved parents, brothers and sisters for their continual support, concern and encouragement during my study and my entire life, your love make all my dreams come to reality.

Many thanks to my friends and colleagues for their kind words and encouragement.

Last but not least, I would like to thank the Libyan State for their moral and financial support as well as the staff in cultural affairs in Libyan embassy in London for their help and support.

Abstract

The work examines response of the upper ocean to time-varying winds. In the Ekman paradigm the effect of wind is considered as time-varying horizontally uniform tangential wind stress applied to the ocean surface and the turbulent diffusion of momentum is described employing the Boussinesq closure hypothesis via a single scalar eddy viscosity. In contrast to all previous studies we take into account both its depth and time dependence and examine effects of density stratification.

We found exact general solution to the full Navier-Stokes equations which describes dynamics of the Ekman boundary layer in terms of the Green's function. Several cases of varying eddy viscosity have been examined:

(a) According to the Zikanov et al. [2003] parameterization (justified by LES) the eddy viscosity in non-stratified fluid increases linearly with depth in the upper part of the fluid, reaching the maximum value at some depth specified by the wind speed, and then decreases linearly with depth in the lower layer. For this model the explicit analytic solution describing Ekman response to arbitrary wind has been obtained and thoroughly compared with the available models employing more simple eddy viscosity profiles lacking the LES validation. The range of situations where much simpler models can be used with acceptable accuracy has been identified.

(b) We considered the simplest model of the upper ocean with mixed layer at the top and stratified fluid below, which in terms of the Ekman model reduces to a two-layer model: the top (turbulent) layer is characterized by a high constant value of eddy viscosity, while the bottom layer has a much smaller viscosity also assumed to be constant. Basic scenarios such as sharp increase of wind and switch off of the wind have been analysed from the viewpoint of finding how and when the vertical profile of stratification affects the surface current caused by wind varying in time. It has been found under what conditions the surface velocity vector is noticeably affected by the presence of stratification. The parameter controlling whether the presence of stratification will manifest itself on the surface is shown to be the non-dimensional depth of the pycnocline: the surface velocity field is quite sensitive to the depth of the mixed layer, but is much less sensitive to the strength of stratification. From the perspective of remote sensing of the characteristics of stratification the using HF radars, it has been concluded that these findings open new possibilities.

(c) When the eddy viscosity is assumed to be both time and depth dependent, three basic scenarios have been thoroughly examined: (i) An increase of wind ending up with a plateau; (ii) Switch-off of the wind; (iii) Periodic wind.

Their analysis shows that accounting for time dependence of eddy viscosity substantially changes the response, compared to the predictions of the models with constant in time viscosity.

We also report a severe limitation of the Ekman type models employed in modelling of the oceanic surface boundary layer. The Ekman current caused by a growing wind quickly becomes unstable with respect to inviscid inflectional instability. These instabilities are fast, which suggests spikes of dramatically enhanced mixing in the corresponding parts of the water column. The instabilities also break down a fundamental element of the Ekman-type models the assumed spatial uniformity. The results require a radical revision of the existing paradigm.

Contents

List of Figures

List of Tables

Notations

u, v, w	the velocity component in the directions of x, y, z
u', v', w'	the turbulent component of velocity in the directions of x, y, z
$\rho, \rho_{air}, \rho_0, \rho'$	the water density, air density, reference density and perturbations of density due to turbulent fluctuations
p, p'	pressure and perturbations of pressure due to turbulent fluctuations
g	the gravitational acceleration
$\boldsymbol{\tau}$	the shear stress vector
ν_e	the eddy viscosity coefficient
ν	the molecular viscosity
ν_{ei}	eddy viscosity in the i-th layer (in the Zikanov et al. [2003] and two-layer models)
$\tilde{\nu}_{e1}(t)$	time dependent factor in the models with separable viscosity profiles $\nu_e(z,t) = \tilde{\nu}_{e1}(t)g(z)$
Ω	the Earth's rotation frequency
ϕ	the latitude
$f, \tilde{f}$	the Coriolis parameters ($\tilde{f} = 2\Omega \sin\phi$, $f = 2\Omega \cos\phi$)
K	the vertical diffusivity coefficient
U, V, W	the mean velocities in the directions of x, y, z
T_{sd}	the sidereal day, $T_{sd} = 23\,\mathrm{hr}\,56\,\mathrm{min}\,4.1\mathrm{s}$
T_i	the inertial period
C_D	the drag coefficient, $\tau = \rho_a C_D U_{10}^2$
U_0	the magnitude of the current at the surface
Φ	the deflection angle between the current and wind direction
U_{10}	the wind speed measured at 10 m above the still water level
δ_e	the scale of e-fold decay, $\delta_e = \sqrt{2\nu_e/f}$
D_E	the Ekman depth, $D_E = \pi\delta_e$
l	the typical length (depth) scale

D	the total depth of the fluid
E_z	Ekman number, $E_z = \nu_e/(fl^2)$
$\tilde{t}$	nondimensional time, $\tilde{t} = ft$
$C(.), S(.)$	the Fresnel's integrals
u_*	the friction velocity
κ	the Von Karman's constant
$\boldsymbol{S}$	Ekman transport vector
$\boldsymbol{U}_s$	Stokes drift velocity
$\boldsymbol{k}$	wavenumber vector of surface waves
σ	frequency of monochromatic wave component
η_s	the elevation of the free surface
α	the amplitude of the wave
t	time
ω	frequency
$J_n[.]$	Bessel functions of order n
$N_n[.]$	Neumann functions of order n
$I_n[.]$	modified Bessel functions of the first kind
$K_n[.]$	modified Bessel functions of the second kind
z_j	The sea surface roughness length scale ($j = 0, 1, 2$)
$H(.)$	the Heaviside function
d^*	the depth at which the eddy viscosity (piecewise-linear profile) reaches its maximum value in the Zikanov et al. [2003] model
h	the total thickness of the turbulent boundary layer in the Zikanov et al. [2003] model
δ_R	the relative discrepancy between Zikanov et al. [2003] model and Elipot and Gille [2009] model, $\delta_R = \lvert\tilde{\boldsymbol{U}}_Z - \tilde{\boldsymbol{U}}_{EG}\rvert/\lvert\tilde{\boldsymbol{U}}_Z\rvert$
Ω^*	the diurnal frequency
d	the mixed layer depth
$\delta_j(0)$	the depth scale ($j = 1, 2$) for stratified model, $\delta_j(0) = \sqrt{2\nu_{ej}/f}$
$\delta_j(\omega)$	the modified depth scale for non-zero frequencies ($j = 1, 2$) in stratified model, $\delta_j(\omega) = \sqrt{2\nu_{ej}/(f+\omega)}$
$\tilde{d}$	the nondimensional depth of the mixed layer, $\tilde{d} = d/\delta_1$
$\tilde{z}$	the nondimensional vertical variable, $\tilde{z} = z/\delta_1$
$\boldsymbol{\Delta}_{\{EG-CE\}}$	the normalized discrepancy in the value of surface velocity between Elipot and Gille's model and the classical Ekman model, $\boldsymbol{\Delta}_{\{EG-CE\}} = \left(\lvert\boldsymbol{U}_{EG}(0) - \boldsymbol{U}_{CE}(0)\rvert\right)/\lvert\boldsymbol{U}_{CE}(0)\rvert$

$\boldsymbol{\Delta}_{\{TL-CE\}}$ the discrepancy in the value of surface velocity vector between the two-layer and classical Ekman models, $\boldsymbol{\Delta}_{\{TL-CE\}} = \boldsymbol{U}_{TL}(0) - \boldsymbol{U}_{CE}(0)$

$\boldsymbol{\Delta}_{\{TL-EG\}}$ the discrepancy in the value of surface velocity vector between the two-layer and Elipot and Gille models, $\boldsymbol{\Delta}_{\{TL-EG\}} = \boldsymbol{U}_{TL}(0) - \boldsymbol{U}_{EG}(0)$

$\boldsymbol{\Delta}_{1\{TL-CE\}}$ the normalized discrepancy in the value of surface velocity between two-layer model the classical Ekman model, $\boldsymbol{\Delta}_{1\{TL-CE\}} = \big(\big|\boldsymbol{U}_{TL}(0) - \boldsymbol{U}_{CE}(0)\big|\big)/\big|\boldsymbol{U}_{CE}(0)\big|$

$\boldsymbol{\Delta}_{1\{TL-EG\}}$ the normalized discrepancy in the value of surface velocity between two-layer model and Elipot and Gille's model, $\boldsymbol{\Delta}_{1\{TL-EG\}} = \big(\big|\boldsymbol{U}_{TL}(0) - \boldsymbol{U}_{EG}(0)\big|\big)/\big|\boldsymbol{U}_{EG}(0)\big|$

$\delta_{\{EG-CE\}}$ the approximate value (scalar value) of the normalized discrepancy for different models obtained under the assumption of large $\zeta = (1+i)\tilde{d}$

$\delta_{\{TL-CE\}}$ the approximate value (scalar value) of the normalized discrepancy for different models obtained under the assumption of large $\zeta = (1+i)\tilde{d}$

$\Delta\Phi_{\{EG-CE\}}$ the discrepancy in the angle of current in the Elipot and Gille [2009] and Ekman [1905] models

$\Delta\Phi_{\{TL-CE\}}$ the discrepancy in the angle of current in the two-layer and Ekman [1905] models

$\Delta\Phi_{\{TL-EG\}}$ the discrepancy in the angle of current in the two-layer and Elipot and Gille [2009] models

Ri the Richardson number

T modified time, $T = \int_0^t \nu_{e1}(\xi)d\xi$

k^* the wavenumber of the most unstable mode of transient Ekman current

$\bar{\delta}$ the characteristic depth scale in the separable eddy viscosity profiles with the power depth dependence

$\tilde{\sigma}$ the order of Bessel and Neumann functions, $\tilde{\sigma} = \frac{1}{2}\big|\frac{1-\mu}{1-\mu/2}\big|,\ \mu > 0$

Chapter 1

Introduction

1.1 Background

The ocean-atmosphere system is very sensitive to the processes in the first few meters below the water surface. In particular, the top 2.5m of water column have the same heat capacity as the whole atmosphere above (e.g. Gill [1982]), while 50% of the surface-penetrating solar radiation is absorbed within the first 0.5 m of the ocean and 50% of the breaking surface wave kinetic energy dissipates within 20% of the significant wave height from the surface (Soloviev and Lukas [2013]). Knowledge of the vertical profiles of surface currents is also of prime importance in the context of modelling horizontal transport of dispersed substances (pollutants, algae, chlorophyll, etc). Yet another strong motivation for studying the processes linking the ocean surface processes and its interior is that electromagnetic remote sensing of the ocean effectively allows us to see only the surface. Fortunately, the physical processes below produce distinguishable surface signatures which could be deciphered to reveal the processes beneath. There is a great variety of processes contributing to the formation of the boundary layer in water ranging from molecular scales to hundreds of kilometers which include, inter alia, wind, surface gravity and capillary waves

and their breaking, air entrainment, surface films, solar heating, shear instabilities, formation of turbulence, turbulent diffusion of momentum and heat, formation of density stratification suppressing the turbulence, Langmuir circulations, subsurface near-inertial waves (Soloviev and Lukas [2013]).

The progress in understanding dynamics of the boundary layer was slow. One of the completely unexpected discoveries of Nansen's polar expedition of 1893–96 was that the surface current, and, thus, the drift of the ice, was predominantly directed to the right of the wind direction. Nansen realised that this is a consequence of the Earth's rotation and predicted that the current vector would spiral clockwise with depth (Nansen [1905], Jenkins and Bye [2006]). The first mathematical model of this phenomenon was proposed in pioneering work (Ekman [1905]). Ekman reduced the effect of wind to tangential stress and, *inter alia,* derived a steady solution of the Navier-Stokes equations describing forced uniform horizontal motion on the f plane under the assumptions of a constant eddy viscosity. The Ekman's classical steady solution predicts the deflection of the surface current due to Earth's rotation to be 45° to the right of the wind direction in the Northern hemisphere (45° to the left in the Southern hemisphere) with the flux integrated over entire depth ('the Ekman transport') at ninety degrees to the right/left of wind direction. In (Ekman [1905]) the development of the Ekman boundary layer from rest has been also described analytically. Within the framework of this model the complete analytical description of dynamics of the Ekman current generated by an arbitrarily varying wind was derived in terms of explicit Green's function by (Gonella [1971]). The model was extended to finite depth and shallow fluid assuming the bottom to remains horizontal (Lewis and Belcher [2004]). Jung et al. [2007] developed the time-dependent Ekman solution for a shallow open sea allowing the water depth to vary with time, this variation in depth can be caused by, for example, a tide. An overview by Jenkins and Bye [2006] provides a neat summary of Ekman's work which has a continuing influence on oceanography. According to (Wang and Huang [2004]) the total global energy input into the Ekman layer is massive- 2.4 TW. The detailed measurements of wind-driven currents showed that the mean velocity does exhibit a smooth spiral resembling qualitatively the theoretical Ekman spiral (Price et al. [1987]), but the

spiral is somewhat flatter in appearance (Chereskin [1995]). Substantial quantitative discrepancies between the predictions of the original Ekman model and observations have been reported. In particular, as pointed by (e.g. Madsen [1977], Weber [1981]) and (Lewis and Belcher [2004]), the surface current deflection with respect to wind is usually about $10 - 30°$, i.e. noticeably smaller than $45°$ predicted by the steady Ekman solution, while the currents at relatively small ($\sim$5 - 20 m) depths are deflected significantly stronger compared to the classical Ekman solution. It was also noted by (Chereskin [1995], Price and Sundermeyer [1999]) that the current speed decreases with depth more rapidly than the current vector rotates to the right. This mismatch is important since the all important eddy viscosity is estimated by fitting observations to formulae of either the decay of speed with depth or of the velocity rotation with depth; the estimates obtained by these two ways can differ by an order of magnitude (Weller [1981], Price et al. [1987], Chereskin [1995], Lenn [2006], Elipot and Gille [2009]). Here we do not aim at reviewing the observations of Ekman currents summarized in a good overview in (Price and Sundermeyer [1999]), we just note that there is an inherent difficulty to estimate uncertainty in extracting the forced Ekman component of the current from observations. Much more observations are needed. However, the maturing remote sensing techniques, such as, multi-frequency high-frequency radars (Teague et al. [2001], Zhang and Zebiak [2002]), new generation of ADCPs (Acoustic Doppler Current Profilers) (Guerra and Thomson [2017]) have the potential to revolutionize the observations in near future.

On the modelling side, since the eddy viscosity parameterizations and, especially, the constant eddy viscosity assumption are a strong oversimplification of a very complicated real picture, there were attempts to improve the Ekman model by choosing better parameterizations of turbulence. The understanding of turbulence phenomenology in the boundary layer, which in itself is an area of intense research (see review of experimental studies in (Csanady [2001], Soloviev and Lukas [2013]), can be briefly summarised as follows: (i) adjacent to the surface there is a layer of intense turbulence generated by wave breaking and mechanical mixing caused by breaking, the layer thickness is of order of significant wave height (Terray et al. [1996]); the current shear in this layer is very small (Kudryavtsev et al. [2008]); (ii) below it lies the layer

resembling the wall turbulence one with the eddy viscosity linearly increasing with depth (Soloviev and Lukas [2013]); however, in contrast to the true wall turbulence layer the eddy viscosity is starting to decrease below a depth scaled as u_*/f, where u_* is the friction velocity and f is the Coriolis parameter. The fundamental question on how good are the eddy viscosity closure and the corresponding parametrization of momentum transfer for this boundary layer, nobody has even dared to ask in writing. This crucial issue has been partially addressed by means of large eddy simulations of steady Ekman boundary layers by (Zikanov et al. [2003]). The work does not simulate waves and their breaking and, hence, ignores the layer adjacent to the surface where mechanical mixing caused by breaking waves makes the vertical shear very weak, but it confirms existence of the wall-like layer below and predicts where the eddy viscosity starts to decrease. Thus, at least for steady regimes it provides a simple depth and latitude dependent parametrization of the eddy viscosity which is theoretically justified for depths exceeding significant wave height, but still far above the seasonal pycnocline depth. It is a work in progress to create good models able to take into account the presence of stratification (either due the air bubbles entrainment near the surface, or diurnal and seasonal pycnoclines) which suppresses the turbulence and thus strongly affects the momentum transfer.

On the theoretical side the attempts to modify the Ekman model to improve its performance while retaining its elegance and simplicity have never stopped. Models with vertical eddy viscosity linearly varying with depth have two major advantages: first, the corresponding reduction of the Navier-Stokes equations can be solved exactly in terms of the Bessel functions (e.g. Madsen [1977], Lewis and Belcher [2004]) and, crucially, the solution for the flow velocity yields a logarithmic boundary layer profile, which, in a certain range of depths, agrees well with available observations (e.g. Csanady [2001]). The first model with the linearly depth dependent eddy viscosity was proposed for steady Ekman currents in shallow water by Thomas [1975], eddy viscosity increases linearly with depth from zero at the bottom, it depends on the bottom roughness and the flow itself. This model predicts a logarithmic velocity profile near the bottom. Another model for steady wind-induced currents in shallow water with a more difficult to justify exponential depth-dependent eddy viscosity

was suggested in (Witten and Thomas [1976]). The advantages of models with eddy viscosity linearly growing with depth were further exploited by Madsen [1977] to describe time-dependent Ekman boundary layer in water of infinite depth. Lewis and Belcher [2004] extended the model further by considering eddy viscosity growing linearly with depth with nonzero value at the surface in both deep and finite depth water. Following the idea first put forward by Huang [1979] the authors also took into account the Stokes drift due to waves; the resulting theoretical predictions better agree with observations of the angular deflections of the steady-state current. Note that the classical steady Ekman solution was found to be unstable with respect to finite wavelength perturbations; linear stability analysis carried out by (Leibovich and Lele [1985]) on the non-traditional $f-$plane has identified the critical Reynolds numbers and parameters of the most unstable modes; however, since the analysis is confined to the classical Ekman model with constant eddy viscosity, crucially, assumed to be the same for the basic flow and the perturbations, it is not clear how relevant are these viscous instabilities for realistic situations. The potentially important idea of instability of Ekman layer has not been pursued further.

The ability of the existing models of Ekman currents to capture response of oceanic boundary layer to varying in time wind stress was thoroughly examined by (Elipot and Gille [2009]) by comparing modelling with nine different Ekman-type models (three types of eddy viscosity depth dependence and and three forms of boundary conditions at the bottom of the mixed layer aimed to mimic the effect of stratified layer below) against the Southern ocean drifter observations carried out within the framework of the ongoing Global Drifter Program (Siedler et al. [2001], see also http://www.aoml.noaa.gov/phod/dac/index.php). The ageostrophic component of near-surface velocity was computed by subtracting altimeter-derived geostrophic velocities from observed drifter velocities corresponding to 15-m depth. Then the transfer function was computed to link these ageostrophic velocities to the observed wind stresses. Some of the tested Ekman-type models proved to be surprisingly successful in describing the variability in the drifter data. However, the reasons why the least likely particular models happened to perform better are not clear; the huge scale of this experiment does not allow one to dismiss these findings as a mere coincidence

and calls for further study.

For illustrative purposes, in the next section we provide a summary of a series of Ekman-type models and a brief review of their continuing impact. These models remains an important part in physical oceanography literature and they are considered as a natural start to understand the processes in the upper ocean, although they are considered to be highly idealised models where there is no an explicit buoyancy forcing is taken into account and the turbulent diffusion of momentum is parameterized by adopting the Boussinesq closure hypothesis. Furthermore, the presence of the surface waves and the behaviour of the turbulent flow in the subsurface layer of the ocean, in particular, Stokes drift, can affect the structure of the Ekman currents (the magnitude of the current surface velocity and the angle of its deflection from the wind) (Craik and Leibovich [1976]; Leibovich [1977a]; Leibovich [1977b]; McWilliams et al. [1997]).

1.2 Review of existing Ekman models

This section includes some of Ekman-type models with different eddy viscosity profiles and different boundary conditions at the base of the boundary layer.

1.2.1 The equation of motion

For a stratified, viscous and rotating flow, the governing equations (Stewart [2008]) on the non-traditional f-plane are:

$$x-\text{ momentum}: \quad \rho\left(\frac{du}{dt}+\tilde{f}w-fv\right)=-\frac{\partial p}{\partial x}+\frac{\partial \tau^{xx}}{\partial x}+\frac{\partial \tau^{xy}}{\partial y}+\frac{\partial \tau^{xz}}{\partial z}\,, \tag{1.1a}$$

$$y-\text{momentum}: \quad \rho\left(\frac{dv}{dt}+fu\right)=-\frac{\partial p}{\partial y}+\frac{\partial \tau^{xy}}{\partial x}+\frac{\partial \tau^{yy}}{\partial y}+\frac{\partial \tau^{yz}}{\partial z}\,, \tag{1.1b}$$

$$z-\text{momentum}: \quad \rho\left(\frac{dw}{dt}-\tilde{f}u\right)=-\frac{\partial p}{\partial z}-\rho\, g+\frac{\partial \tau^{xz}}{\partial x}+\frac{\partial \tau^{yz}}{\partial y}+\frac{\partial \tau^{zz}}{\partial z}\,, \tag{1.1c}$$

$$\text{continuity equation}: \quad \frac{d\rho}{dt}+\rho\left(\frac{\partial u}{\partial x}+\frac{\partial v}{\partial y}+\frac{\partial w}{\partial z}\right)=0\,, \tag{1.1d}$$

$$\text{density equation}: \quad \frac{d\rho}{dt}=K\,\nabla^2\rho\,, \tag{1.1e}$$

where the standard Cartesian frame with axis directed: x-eastward, y-northward and z-downward is used, $z = 0$ is chosen to be at the free surface of the ocean. u, v, w are the velocities components in the directions of x, y, z, respectively, τ terms are the normal and shear stresses, ρ is the fluid density, p is the pressure, g is the gravitational acceleration, K is the diffusivity coefficient, $f = 2\Omega \sin\phi$ and $\tilde{f} = 2\Omega \cos\phi$ ($\Omega = 7.292 \times 10^{-5}$ radians/s is the Earth's rotation frequency and ϕ is the latitude) are the vertical and horizontal Coriolis parameters respectively, and

$$\frac{d}{dt} = \frac{\partial}{\partial t} + u\frac{\partial}{\partial x} + v\frac{\partial}{\partial y} + w\frac{\partial}{\partial z}$$

is the material derivative.

If the flow is incompressible, eq.(1.1d) simplifies to:

$$\frac{\partial u}{\partial x} + \frac{\partial v}{\partial y} + \frac{\partial w}{\partial z} = 0\,. \tag{1.2}$$

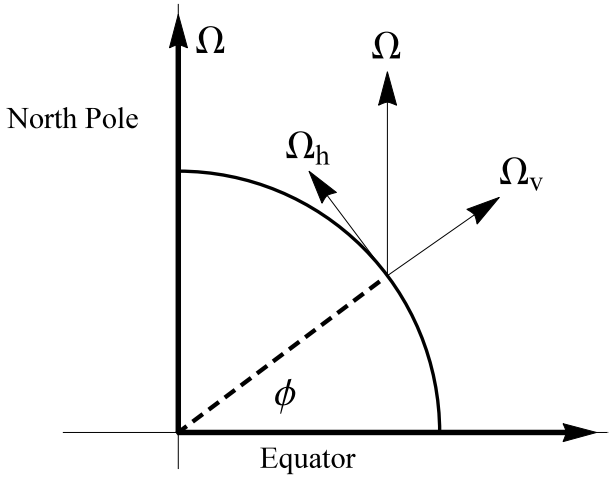

FIGURE 1.1: Sketch of the rotation vector $\mathbf{\Omega}$ at latitude ϕ, giving rise to the Coriolis components $f = 2\mathbf{\Omega}_v$ and $\tilde{f} = 2\mathbf{\Omega}_h$

1.2.2 Approximations

This subsection includes a brief description of some approximations (e.g. Phillips [1977]; Cushman-Roisin and Beckers [2007]).

1.2.2.1 The rigid-lid approximation

The ocean surface is considered to be constant and level and this implies that the elevations of the surface are neglected and there is no flow through it, so that the vertical velocity at the free surface will be zero, $w = 0$, while the horizontal velocities are non-zero and determined by solving the equations. This is the so-called "the rigid-lid approximation".

1.2.2.2 Boussinesq Approximation

The Boussinesq approximation is based on the assumption that the variation in density, $\rho'(x, y, z, t)$, is small compared to its average value, ρ_0, and in this case the actual density ρ, $\rho = \rho_0 + \rho'$; $|\rho'| \ll \rho_0$, can be replaced by its reference value in every term in the momentum equations except when it is multiplied by gravitational acceleration.

1.2.2.3 The Reynolds stresses

Consider a fluid flow of the form:

$$u = U + u'; \qquad v = V + v'; \qquad w = W + w'; \qquad p = P + p' \,. \tag{1.3}$$

where (U, V, W, P, ρ_0) describe the mean flow and (u', v', w', p', ρ') describe the turbulent disturbances. The mean flow velocity, for example U, is found by averaging over time or space:

$$U = \langle u \rangle = \frac{1}{T} \int_0^T u(t)dt \;\text{ or }\; U = \langle u \rangle = \frac{1}{X} \int_0^X u(x)dx \,.$$

Here, there is an implicit assumption that there is a gap between turbulent scales and the scales of the mean flow.

The non-linear terms in the momentum equation in the x-direction can be written

as follows:

$$\left\langle (U+u')\,\frac{\partial (U+u')}{\partial x}\right\rangle = \left\langle U\frac{\partial U}{\partial x}\right\rangle + \left\langle U\frac{\partial u'}{\partial x}\right\rangle + \left\langle u'\frac{\partial U}{\partial x}\right\rangle + \left\langle u'\frac{\partial u'}{\partial x}\right\rangle$$
$$= \left\langle U\frac{\partial U}{\partial x}\right\rangle + \left\langle u'\frac{\partial u'}{\partial x}\right\rangle , \tag{1.4}$$

where

$$\left\langle U\frac{\partial u'}{\partial x}\right\rangle = \left\langle u'\frac{\partial U}{\partial x}\right\rangle = 0\,.$$

and similarly for the other non-linear terms. Substituting the mean and turbulent components (1.3) into the equation (1.1d) gives:

$$\frac{\partial U}{\partial x}+\frac{\partial V}{\partial y}+\frac{\partial W}{\partial z}+\frac{\partial u'}{\partial x}+\frac{\partial v'}{\partial y}+\frac{\partial w'}{\partial z}=0\,. \tag{1.5}$$

The previous equation can be divided to two equations as follows:

$$\frac{\partial U}{\partial x}+\frac{\partial V}{\partial y}+\frac{\partial W}{\partial z}=0\,, \tag{1.6}$$

$$\frac{\partial u'}{\partial x}+\frac{\partial v'}{\partial y}+\frac{\partial w'}{\partial z}=0\,. \tag{1.7}$$

The x- momentum equation for the mean flow is

$$\frac{dU}{dt}-fV=-\frac{1}{\rho_0}\frac{\partial P}{\partial x}+\nu\nabla^2 U-\frac{\partial\langle u'\,u'\rangle}{\partial x}-\frac{\partial\langle u'\,v'\rangle}{\partial y}-\frac{\partial\langle u'\,w'\rangle}{\partial z}\,. \tag{1.8}$$

where ν is the molecular viscosity. The effects of the turbulence fluctuations on the mean flow are presented by the last three terms on the right-hand side of equation (1.8). The previous equation can be rewritten as follows

$$\frac{dU}{dt}-fV=-\frac{1}{\rho_0}\frac{\partial P}{\partial x}+\frac{\partial}{\partial x}\left[\nu\frac{\partial U}{\partial x}-\langle u'\,u'\rangle\right]+\frac{\partial}{\partial y}\left[\nu\frac{\partial U}{\partial y}-\langle u'\,v'\rangle\right]+$$
$$\frac{\partial}{\partial z}\left[\nu\frac{\partial U}{\partial z}-\langle u'\,w'\rangle\right]\,, \tag{1.9}$$

where the term $(\,-\frac{\partial}{\partial x}\langle u'\,u'\rangle-\frac{\partial}{\partial y}\langle u'\,v'\rangle-\frac{\partial}{\partial z}\langle u'\,w'\rangle\,)$ represents an additional frictional force per unit mass caused by the turbulence, the expressions $-\langle u'\,u'\rangle, -\langle u'\,v'\rangle$ and

$-\langle u'\,w'\rangle$ are called Reynolds stresses (turbulent stresses).

Similarly, the average of the momentum equations in the $y-$ and $z-$ direction over the turbulent fluctuations gives:

$$\frac{dV}{dt} + fU = -\frac{1}{\rho_0}\frac{\partial P}{\partial x} + \frac{\partial}{\partial x}\left[\nu\frac{\partial V}{\partial x} - \langle u'\,v'\rangle\right] + \frac{\partial}{\partial y}\left[\nu\frac{\partial V}{\partial y} - \langle v'\,v'\rangle\right] + \frac{\partial}{\partial z}\left[\nu\frac{\partial V}{\partial z} - \langle v'\,w'\rangle\right], \tag{1.10}$$

and,

$$\frac{dW}{dt} - \tilde{f}U = -\frac{1}{\rho_0}\frac{\partial P}{\partial x} - \frac{\rho' g}{\rho_0} + \frac{\partial}{\partial x}\left[\nu\frac{\partial W}{\partial x} - \langle u'\,w'\rangle\right] + \frac{\partial}{\partial y}\left[\nu\frac{\partial W}{\partial y} - \langle v'\,v'\rangle\right] + \frac{\partial}{\partial z}\left[\nu\frac{\partial W}{\partial z} - \langle w'\,w'\rangle\right]. \tag{1.11}$$

To illustrate how these stresses are calculated we consider an example of horizontally uniform and steady mean flow, so that equation (1.9) becomes:

$$fV + \frac{\partial}{\partial z}\left[\nu\frac{\partial U}{\partial z} - \langle u'\,w'\rangle\right] = 0\,. \tag{1.12}$$

We parameterize the Reynolds stresses by adopting the Boussinesq hypothesis,

$$-\rho\langle u'\,w'\rangle = \tau_{xz} = \rho\nu_e\frac{\partial U}{\partial z}\,, \tag{1.13}$$

where ν_e is an eddy viscosity coefficient found from the observations.

Observations from the Eastern Boundary Current (EBC) mooring, which carried out in the coast of the Northern California at $37.1°$ N during a four months period, showed that the vertical viscosity has a value of 274×10^{-4} and $1011\times10^{-4}\,\mathrm{m^2s^{-1}}$ based on the decay of the amplitude and rotation rate respectively (Chereskin [1995]). These values has also been estimated as 60×10^{-4} and $540\times10^{-4}\,\mathrm{m^2s^{-1}}$ from LOTUS3 (the Long Term Upper Ocean Study) measurements which was collected from the Western Sargasso Sea ($34°$ N) for about 160 days. Table (1.1) (from Huang [1979]) gives an idea of the spread of numerical values of the vertical viscosity coefficient and the thickness of the mixed layer as found in observations by various authors in different conditions. The coefficient ranges between $O(10^{-4})$ and $O(10^{-1})$ $\mathrm{m^2s^{-1}}$.

TABLE 1.1: Eddy viscosity values (Huang [1979]).

Location	Layer depth m	$\nu_e, 10^{-4}(m^2 s^{-1})$	Source
Danish Waters	0-15	1.9-3.8	All currents
Arctic Ocean		160	Under ice
Danish Waters		250-1500	All currents
Kuroshio	0-200	680-7500	All currents
Japan Sea	0-200	150-1460	All currents
North Siberian Shelf	0-60	0-1000	Tidal currents
North Sea	0-31	75-1720	Strong tidal currents
Tropical Atlantic Ocean	0-50	320	Temperature fluctuation
North Siberian Shelf	0-60	10-400	Tidal current
Atlantic Ocean $50°S - 10°N$	0-200	7-50	Wind currents
Japan Sea	0-10	100	Tidal currents
Arctic Ocean	0-100	23.8	Ice drift
North Atlantic	0-4	146	Temperature
	4-8	96	fluctuation
	8-12	47	
Open Ocean	0-10	150-225	Surface
Lake Huron	30	65-160	Wind current
Tropical Atlantic Ocean	0-12	420± 84	Temperature fluctuation
Tropical Atlantic Ocean	0-10	62	Temperature
	10-20	68	fluctuation
	20-30	85	
Tropical Atlantic Ocean	0-12	480	Temperature
	20-50	265	fluctuation

1.2.3 Inertial Oscillations

The inertial Oscillations are considered to be the simplest type of time-dependent motion caused only by the Coriolis force (e.g. Stewart [2008]). The inertial Oscillations and the Ekman currents are closely interlinked. Here we consider the basics of the mathematical model of these motions. Often the viscous effects can be neglected

from the momentum equations, which yields:

$$x-\text{momentum}: \quad \rho\left(\frac{du}{dt}+\tilde{f}w-fv\right)=-\frac{\partial p}{\partial x}\,, \tag{1.14a}$$

$$y-\text{momentum}: \quad \rho\left(\frac{dv}{dt}+fu\right)=-\frac{\partial p}{\partial y}\,, \tag{1.14b}$$

$$z-\text{momentum}: \quad \rho\left(\frac{dw}{dt}-\tilde{f}u\right)=-\frac{\partial p}{\partial z}-\rho\, g\,. \tag{1.14c}$$

We consider the limit where the horizontal pressure gradient can be neglected, i.e. the limit of infinitely long inertial wave–the inertial oscillations,

$$\frac{\partial p}{\partial x}=\frac{\partial p}{\partial y}=0\,. \tag{1.15}$$

In this limit the mass of water moves horizontally, hence equations (1.14) become:

$$\frac{\partial u}{\partial t}-f\,v=0\,, \tag{1.16a}$$

$$\frac{\partial v}{\partial t}+f\,u=0\,. \tag{1.16b}$$

These equations can be reduced to a single equation.

$$\frac{d^2u}{dt^2}+f^2\,u=0\,, \tag{1.17}$$

which has the solution:

$$\begin{aligned} u=&V_0\,sin(ft)\,,\\ v=&V_0\,cos(ft)\,,\\ V_0^2=&u^2+v^2\,. \end{aligned} \tag{1.18}$$

Equations (1.18) are the circle equation in a parametric representation with a diameter equal to $2V_0/f$ and period (inertial period) $T_i=(2\pi)/f=T_{sd}/(2\,\sin\phi)$, where

$T_{sd} = 23\,\text{hr}\ 56\,\text{min}\ 4.1\,\text{s}$ is a sidereal day. Inertial oscillations are free motions, while the Ekman currents are forced motions. However, at certain timescales the Ekman currents behave as (almost) free motions as inertial oscillations.

1.2.4 The Ekman Layer

The Ekman layer is a horizontal boundary layer which occurs due to a horizontal frictional shear stress. Its characteristic thickness varies widely, could be a few hundred meters thick. Such layer exists, for example, along the surface and the bottom of the ocean, and also at the atmosphere layer which in a direct contact with the ocean surface (the planetary boundary layer). The dynamics in this layer was first examined by Vagn Walfrid Ekman (Ekman [1905]). Nansen (Nansen [1905]) indicated that the wind stress, frictional force and the Coriolis force are important and must be balanced when icebergs are drifted by wind on a rotating Earth, in which the rotational force is perpendicular to the velocity while the drag must be opposite to the velocity direction (Stewart [2008]).

Here, we describe ocean response to varying wind starting with the Navier-Stokes equations for stratified viscous and horizontally uniform flow on the non-traditional f-plane under the Boussinesq approximation (e.g. Phillips [1977]; Cushman-Roisin and Beckers [2007]). In the Cartesian frame with x directed eastward, y-northward and z-downward, with the origin at the free surface of the ocean the Reynolds averaged Navier-Stokes equations for the the eastward and northward velocities u, v caused by a time-varying horizontally uniform wind stress $\tau_{xz}(0,t)$ take the form

$$\frac{\partial u}{\partial t} - fv = \frac{1}{\rho}\frac{\partial \tau_{xz}(z,t)}{\partial z}, \tag{1.19a}$$

$$\frac{\partial v}{\partial t} + fu = \frac{1}{\rho}\frac{\partial \tau_{yz}(z,t)}{\partial z}, \tag{1.19b}$$

The Reynolds stresses terms $\tau_{xz} \equiv -\rho\langle u'\,w'\rangle$, $\tau_{yz} \equiv -\rho\langle v'\,w'\rangle$ describe the downward transfer of eastward and northward momentum, here u',v' and w' are the turbulent velocities, $\langle \ldots \rangle$ means Reynolds' averaging over turbulent fluctuations. The explicit

effect of the horizontal component of the Earth rotation $\tilde{f} = 2\Omega\cos\phi$ and the non-linear terms vanish identically for horizontally uniform flows we are interested in, while an implicit dependence on $\tilde{f}$ is retained in the Reynolds stresses terms. Taking into account $\tilde{f}$ is also essential for studying stability of the solutions of the Ekman equations (Leibovich and Lele [1985]).

We close the equations for the Reynolds averaged flow by adopting the commonly used Boussinesq hypothesis, i.e. assume the Reynolds stresses to be proportional to the mean velocity gradient, $\partial\boldsymbol{u}/\partial z$, through a single scalar eddy viscosity coefficient, $\nu_e(z,t)$:

$$\rho\nu(z,t)\frac{\partial u}{\partial z} \equiv \tau_{xz} \equiv -\rho\langle u\, w\rangle\,, \quad \rho\nu(z,t)\frac{\partial v}{\partial z} \equiv \tau_{yz} \equiv -\rho\langle v\, w\rangle\,. \tag{1.20}$$

In our context the use of this closure has been justified in (Zikanov et al. [2003]) through the extensive large-eddy simulations, although only for the steady winds. We can also expect it to be applicable for the time dependent winds for the time scales exceeding characteristic scale of the turbulence adjustment.

Upon adopting the Boussinesq closure (1.20) the momentum equations (1.19) can be written as

$$\frac{\partial u}{\partial t} - fv = \frac{1}{\rho}\frac{\partial}{\partial z}\left(\rho\nu_e(z,t)\frac{\partial u}{\partial z}\right), \tag{1.21a}$$

$$\frac{\partial v}{\partial t} + fu = \frac{1}{\rho}\frac{\partial}{\partial z}\left(\rho\nu_e(z,t)\frac{\partial v}{\partial z}\right). \tag{1.21b}$$

Strictly speaking the density ρ depends on z and t and its evolution has to be described by an extra diffusion equation with appropriate boundary condition at the surface specifying the buoyancy fluxes through the surface and direct solar heating in the vicinity of the surface. However, under the Boussinesq approximation we adopt, we can neglect the density dependence on z and t and assume it to be constant. In our consideration the presence of density stratification manifests itself only in depth dependence of the eddy viscosity. We do not assume any particular relation between the stratification and viscosity. Although it is well known that stratification suppresses turbulence, which decreases eddy viscosity, here we do not specify this link.

We will assume vertical dependence of eddy viscosity to be a given function of depth. In §2 and §4 we confine our study to density uniform flows, which makes the equations above independent of density, while the effects of density stratification are the focus of the analysis in §3, where a two-layer model of stratification is considered.

Following the original work by (Ekman [1905]) we introduce complex horizontal velocity $\boldsymbol{U} = u + iv$ and adopt the the Boussinesq approximation which enables us to cast the momentum equations into the following single equation on $\boldsymbol{U}$,

$$\frac{\partial \boldsymbol{U}}{\partial t} + if\boldsymbol{U} = \frac{\partial}{\partial z}\left(\nu_e(z,t)\frac{\partial \boldsymbol{U}}{\partial z}\right). \tag{1.22}$$

The equation represents an exact reduction of the Navier-Stokes equations for the horizontally uniform viscous flows on the f-plane with time and depth dependent viscosity. Different profiles were discussed in the literature, none with time dependent viscosity. Here, the problem is analyzed for cases of eddy viscosity profiles with both temporal and vertical dependence.

The motion has to satisfy the boundary condition of continuity of the shear stress at the free surface: a horizontally uniform time dependent wind produces tangential stress $\boldsymbol{\tau}(t)$ at the ocean surface, so that

$$\left[\nu_e(z,t)\,\frac{\partial \boldsymbol{U}}{\partial z}\right]_{z=0} = \frac{-\boldsymbol{\tau}(t)}{\rho}\,. \tag{1.23}$$

The velocity should vanish at the bottom $z = D$ which requires,

$$\boldsymbol{U}(D) = 0 \tag{1.24}$$

However, throughout the most of our work we will consider only deep fluid, which implies,

$$\frac{\partial \boldsymbol{U}}{\partial z} \to 0 \quad \text{as} \quad z \to \infty\,. \tag{1.25}$$

The initial condition at $t = 0$ is an arbitrary initial distribution $\boldsymbol{U}(z, 0)$.

1.2.4.1 Steady-state solution with a constant viscosity

A good insight into the nature of the Ekman currents provide steady-state solutions of the Ekman equations (1.22, 1.23, 1.24, 1.25). In a steady state, the term, $\boldsymbol{U}_t$, on the left hand side of equation (1.22) vanishes, and assuming that the eddy viscosity to be constant (Ekman [1905]), the momentum equations and boundary conditions mentioned above can be rewritten as

$$\nu_e \frac{d^2 \boldsymbol{U}}{d z^2} - i f \boldsymbol{U} = 0 \,, \tag{1.26}$$

where a steady wind blows tangentially to the surface of the ocean and directed along the positive x-axis

$$\frac{d \boldsymbol{U}}{d z} = \frac{-\boldsymbol{\tau}}{\rho \nu_e} \quad \text{at} \quad z = 0 \,. \tag{1.27}$$

The general solution to equation (1.26) is given by

$$\boldsymbol{U} = c_1 e^{m_1 z} + c_2 e^{-m_1 z} \,, \tag{1.28}$$

where

$$m_{1,2} = \pm \left(\frac{1+i}{\sqrt{2}} \right) \sqrt{\frac{f}{\nu_e}} \,. \tag{1.29}$$

The constants c_1 and c_2 are determined by applying the boundary conditions (1.23 and 1.25).

$$c_1 = 0 \quad \text{and} \quad c_2 = \frac{\boldsymbol{\tau}\, e^{-i\pi/4}}{\rho \sqrt{f\, \nu_e}} \,. \tag{1.30}$$

Thus, the complex velocity takes the form

$$\boldsymbol{U} = u + iv = \frac{\boldsymbol{\tau}\,(1-i)}{\rho\sqrt{2\,f\,\nu_e}}\ \exp\left[-(1+i)z/\delta_e\right]\,. \tag{1.31}$$

It follows that

$$u = U_0\ \exp\left[\frac{z}{\delta_e}\right]\ \sin\left(\frac{\pi}{4} - \frac{z}{\delta_e}\right)\,, \tag{1.32}$$

and,

$$v = U_0\ \exp\left[\frac{z}{\delta_e}\right]\ \cos\left(\frac{\pi}{4} - \frac{z}{\delta_e}\right)\,. \tag{1.33}$$

Where $U_0 = \frac{\tau}{\rho\sqrt{f\,\nu_e}}$ and $\delta_e = \sqrt{\frac{2\,\nu_e}{f}}$ are the magnitude of the flow at the surface and the exponential decay scale respectively. The amplitude of the velocity decays exponentially with depth (see figure 1.2):

$$\left(u^2(z) + v^2(z)\right)^{1/2} = U_0\ \exp\left[-\frac{z}{\delta_e}\right]\,. \tag{1.34}$$

The wind stress is usually parametrized by the following formula (e.g. Stewart [2008]):

$$\tau_x = \tau = \rho_{air}\,C_D\,U_{10}^2\,, \tag{1.35}$$

where $\rho_{air} = 1.25\mathrm{kg/m}^3$ is the air density, $C_D = 1.4\times10^{-3}$ is the drag coefficient, and U_{10} is the speed of the wind, measured 10 m above the unperturbed seawater level. Also, in terms of wind speed U_0 is linked to U_{10} as follows:

$$U_0 = \frac{0.0127U_{10}}{\sqrt{\sin|\phi|}}; \qquad |\phi| \geqslant 10\,. \tag{1.36}$$

The first depth at which the direction of the current velocity is opposite to the velocity direction at the surface, was named by Ekman [1905] as the "the Depth of

Wind-currents":

$$D_E = \pi\, \delta_e = \pi \sqrt{\frac{2\nu_e}{f}}\,, \tag{1.37}$$

with the use of the equations (1.35 and 1.36) and the parameters which are mentioned above, equation (1.37) can be rewritten as:

$$D_E = \frac{7.6\, U_{10}}{\sqrt{\sin|\phi|}}\,. \tag{1.38}$$

The depth of the Ekman layer changes with wind speed and latitude, it ranges between 40 to 598 m. Table (1.2) gives Ekman layer depths according to typical wind speeds and at some latitudes.

TABLE 1.2: Ekman depths

Wind speed: U_{10} m/s	Latitude:	15°	45°	75°
5		75 m	45 m	40 m
10		150 m	90 m	77 m
20		300 m	180 m	155 m
40		598 m	362 m	309 m

The dimensionless ratio of viscous force to the Coriolis force in the momentum (1.26) is called the Ekman number, E_z:

$$E_z = \frac{\text{viscous term}}{\text{Coriolis term}} = \frac{\nu_e \frac{\partial^2 u}{\partial z^2}}{f\, u} \approx \frac{\nu_e \frac{U}{l^2}}{f\, U} = \frac{\nu_e}{f\, l^2}\,, \tag{1.39}$$

where U and l are the typical velocity of the flow and typical length (depth) scale describing the motion respectively. An equivalent form to the Ekman depth form (1.37) is derived from equation (1.39):

$$l = \sqrt{\frac{\nu_e}{f\, E_z}}\,, \tag{1.40}$$

where the depth defined by Ekman is obtained by setting $E_z = 1/(2\pi^2) \approx 0.05$ in the previous equation. For flows with small Ekman numbers the Coriolis is the dominant force in the momentum equations.

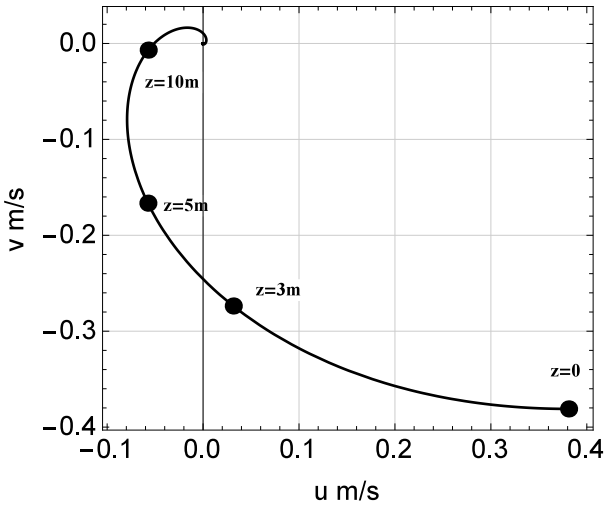

FIGURE 1.2: The classical Ekman spiral. The parametrs values are $f = 10^{-4}\,\mathrm{s}^{-1}$, $\tau = 0.175\,\mathrm{N/m}^2$, $\rho = 1027\mathrm{kg/m}^3$ and $\nu_e = 10^{-3}\,\mathrm{m}^2\mathrm{s}^{-1}$.

The velocity vector direction turns clockwise in the northern hemisphere, while in the southern hemisphere it turns counter-clockwise and the magnitude of the surface velocity decays with depth. The angle between the wind stress and the surface current is 45 degrees and it grows with depth. An example of the horizontal velocity of the classical Ekman spiral is shown in figure (1.2).

The depth averaged velocity in the $x-$direction and the $y-$direction is:

$$S_x = \int_{-\infty}^{0} u\, dz = 0\,, \tag{1.41a}$$

$$S_y = \int_{-\infty}^{0} v\, dz = \frac{\tau}{\rho\, f}\,. \tag{1.41b}$$

The solution to equation (1.26) subjected to the no-slip condition at the bottom ($\boldsymbol{U} = 0 \quad at \quad z = D$) and to the upper condition which is mentioned before in equation (1.27), is given by

$$\boldsymbol{U} = u + iv = \frac{\boldsymbol{\tau}\; e^{-i\pi/4}}{\rho\,\sqrt{f\,\nu_e}}\; \frac{\sinh\left[(1+i)\,(D-z)\,\sqrt{\frac{f}{2\nu_e}}\right]}{\cosh\left[(1+i)\,D\,\sqrt{\frac{f}{2\nu_e}}\right]}\,. \tag{1.42}$$

The previous equation can be written as follows

$$u = A\ \sinh(\hat{\xi}/\delta_e)\ \cos(\hat{\xi}/\delta_e) + B\ \cosh(\hat{\xi}/\delta_e)\ \sin(\hat{\xi}/\delta_e)\,, \tag{1.43a}$$

$$v = A\ \cosh(\hat{\xi}/\delta_e)\ \sin(\hat{\xi}/\delta_e) - B\ \sinh(\hat{\xi}/\delta_e)\ \cos(\hat{\xi}/\delta_e)\,, \tag{1.43b}$$

where

$$\begin{aligned}
\hat{\xi} &= D - z, \quad \delta_e = \sqrt{\frac{2\nu_e}{f}}\,, \\
A &= \frac{\sqrt{2}\,\tau}{\rho\sqrt{f\nu_e}}\,\frac{\cosh(D/\delta_e)\,\cos(D/\delta_e) - \sinh(D/\delta_e)\,\sin(D/\delta_e)}{\cosh(2D/\delta_e) + \cos(2D/\delta_e)}, \\
B &= \frac{\sqrt{2}\,\tau}{\rho\sqrt{f\nu_e}}\,\frac{\cosh(D/\delta_e)\,\cos(D/\delta_e) + \sinh(D/\delta_e)\,\sin(D/\delta_e)}{\cosh(2D/\delta_e) + \cos(2D/\delta_e)}\,.
\end{aligned}$$

Equations (1.43a) and (1.43b) describes the steady state flow of finite Ekman layer, and the resultant Ekman fluxes in the $x-$direction and the $y-$direction are:

$$S_x = \int_0^D u\,dz = \frac{\tau\,D_E^2}{\mu\,\pi^2}\,\frac{\sinh(D/\delta_e)\ \sin(D/\delta_e)}{\cosh(2D/\delta_e) + \cos(2D/\delta_e)}\,, \tag{1.44a}$$

$$S_y = \int_0^D v\,dz = \frac{\tau\,D_E^2}{2\mu\,\pi^2}\,\frac{2\,\cosh(D/\delta_e)\,\cos(D/\delta_e) - \cosh(2D/\delta_e)\ -\ \cos(2D/\delta_e)}{\cosh(2D/\delta_e) + \cos(2D/\delta_e)}\,, \tag{1.44b}$$

where $D_E = \pi\delta_e$. For a finite depth, the deflection angle of the surface current is not precisely equal to 45 degrees to the right of the wind vector, it depends on the ratio of the depth D to the Ekman layer depth D_E,

$$tan(\Phi) = \left(\frac{v}{u}\right)_{z=0} = \frac{\sin(2D/\delta_e) - \sinh(2D/\delta_e)}{\sin(2D/\delta_e) + \sinh(2D/\delta_e)}\ ;\ \ 2D/\delta_e = \frac{2\pi D}{D_E}\,.$$

When $D_E \gg D$, the angle is small, and the flow at the surface is almost in the wind direction. It alternates between less and larger than 45 degrees with increasing depth.

1.2.4.2 Stokes-Ekman layer

The nature of the Ekman layer changes due to the presence of surface waves (e.g. McWilliams et al. [1997], Sullivan and McWilliams [2010]). The horizontal momentum "Stokes-Ekman" equations, which follow from horizontal averaging of the Craik-Leibovich equations, for the case of constant viscosity are as follows

$$\frac{\partial \boldsymbol{U}}{\partial t} + if(\boldsymbol{U} + \boldsymbol{U}_s) = \nu_e \frac{\partial^2 \boldsymbol{U}}{\partial z^2}\,, \tag{1.45}$$

where $\boldsymbol{U}_s(z,t)$ is the Stokes drift velocity. In order to simplify the problem, it is often assumed (e.g. McWilliams et al. [1997]) that there is a single monochromatic deep water wave,

$$\eta_s(x,y,t) = \alpha\, \cos(\boldsymbol{k}.\boldsymbol{x} - \sigma t)\,, \tag{1.46}$$

where η_s is the elevation of the free surface, α is the amplitude, $\boldsymbol{k} = (k_x, k_y)$ is the wave-vector and $\sigma = \sqrt{g|\boldsymbol{k}|}$ is the frequency of linear wave with wave-vector $\boldsymbol{k}$. The corresponding Stokes drift is then

$$\boldsymbol{U}_s(z,t) = U_s\, \boldsymbol{e}_U\, e^{-2|\boldsymbol{k}|z}\,, \tag{1.47}$$

where $U_s = \sigma|\boldsymbol{k}|a^2$ (Phillips [1977]) and $\boldsymbol{e}_U$ is a unit vector aligned with the wind. The equation (1.45) can be rewritten as

$$\frac{\partial \boldsymbol{U}}{\partial t} + if\boldsymbol{U} - \nu_e \frac{\partial^2 \boldsymbol{U}}{\partial z^2} = -i\, f\, U_s e^{-2|\boldsymbol{k}|z}\,, \tag{1.48}$$

subjected to the following boundary conditions:

$$\left[\nu_e \frac{\partial \boldsymbol{U}}{\partial z}\right]_{z=0} = \frac{-\boldsymbol{\tau}(t)}{\rho}\,. \tag{1.49}$$

$$\boldsymbol{U} \to 0 \quad \text{as} \quad z \to \infty\,. \tag{1.50}$$

For a steady-state case, the governing equation reduces to the diffusion equation:

$$if\boldsymbol{U} - \nu_e \frac{d^2\boldsymbol{U}}{dz^2} = -i\, f\, U_s e^{-2|\boldsymbol{k}|z}\,. \tag{1.51}$$

Its general solution is:

$$\boldsymbol{U}(z) = \boldsymbol{U}_h(z) + \boldsymbol{U}_p(z)\,, \tag{1.52}$$

where $\boldsymbol{U}_p(z)$ is a particular solution in the form:

$$\boldsymbol{U}_p(z) = Ae^{-2|\boldsymbol{k}|z}\,, \tag{1.53}$$

where

$$A = \frac{ifUs}{4k^2\nu_e - if}\,, \tag{1.54}$$

so that,

$$\boldsymbol{U}_p(z) = \frac{ifUs}{4k^2\nu_e - if}\, e^{-2|\boldsymbol{k}|z}\,. \tag{1.55}$$

The other part of the solution (the general solution of the homogeneous equation), $\boldsymbol{U}_h$, is:

$$\boldsymbol{U}_h(z) = c_1 \exp\left[\sqrt{\frac{if}{\nu_e}}\, z\right] + c_2 \exp\left[-\sqrt{\frac{if}{\nu_e}}\, z\right]\,. \tag{1.56}$$

The condition $\boldsymbol{U}_h \to 0 \quad \text{as} \quad z \to \infty$ leads to $c_1 = 0$. And by applying the condition at the surface we obtain $c_2 = \sqrt{\frac{\nu_e}{if}}\left(\frac{\boldsymbol{\tau}}{\rho\nu_e} - \frac{2ikfU_s}{4k^2\nu_e - if}\right)$. so that,

$$\boldsymbol{U}_h(z) = \sqrt{\frac{\nu_e}{if}}\left(\frac{\boldsymbol{\tau}}{\rho\nu_e} - \frac{2ikfU_s}{4k^2\nu_e - if}\right) \exp\left[-\sqrt{\frac{if}{\nu_e}}\, z\right]\,. \tag{1.57}$$

The steady-state solution is then

$$\begin{aligned}\boldsymbol{U}(z) &= \boldsymbol{U}_h(z) + \boldsymbol{U}_p(z) \\ &= \sqrt{\frac{\nu_e}{if}}\left(\frac{\boldsymbol{\tau}}{\rho\nu_e} - \frac{2ikfU_s}{4k^2\nu_e - if}\right)\exp\left[-\sqrt{\frac{if}{\nu_e}}\,z\right] + \frac{ifUs}{4k^2\nu_e - if}\,e^{-2|\boldsymbol{k}|z} \\ &= \frac{1-i}{\sqrt{2f\nu_e}}\left(\frac{\boldsymbol{\tau}}{\rho} - 2Ak\nu_e\right)\exp\left[-\sqrt{\frac{if}{\nu_e}}\,z\right] + A\,e^{-2|\boldsymbol{k}|z}\,, \end{aligned} \tag{1.58}$$

where A is given by equation (1.54). Figure (1.3) shows that the current turning is reduced due to the wave effects. The analysis of Stokes-Ekman equations in the literature is confined to strongly idealised cases where time dependent spectrum of surface waves is approximated by monochromatic wave of constant amplitude. Time dependence of eddy viscosity has been also ignored. In this thesis we aim to address this limitation by considering a more realistic situation (time and depth dependent viscosity model with time dependent wind waves).

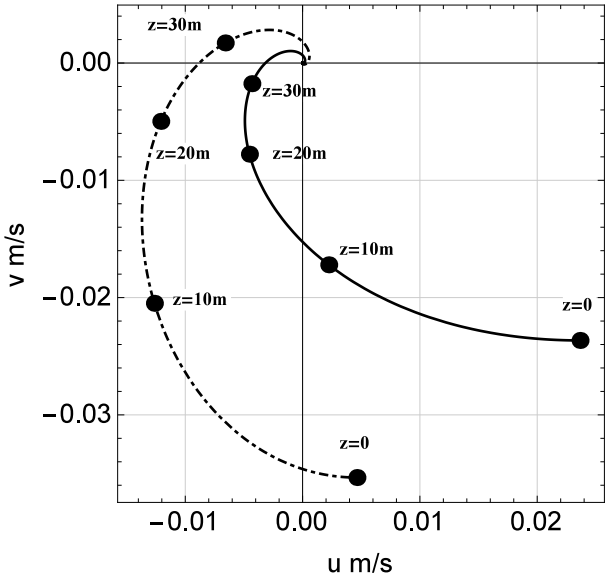

FIGURE 1.3: Compersion between the classical Ekman (solid line) and Stoke-Ekman (dotted-dashed line) models. The parametrs (McWilliams et al. [1997]) values are $f = 10^{-4}\,\mathrm{s}^{-1}$, $\tau = 0.037\,\mathrm{N/m}^2$, $\rho = 1027\mathrm{kg/m}^3$, $\nu_e = 1.16\times10^{-2}\,\mathrm{m}^2\mathrm{s}^{-1}$, $k = 2\pi/60\mathrm{m}^{-1}$ and $U_s = 0.068\mathrm{m\ s}^{-1}$.

1.2.4.3 Time-dependent Ekman solution with a constant eddy viscosity

Under the assumption of constant eddy viscosity, equations (1.22) in the complex form are as follows

$$\frac{\partial \boldsymbol{U}}{\partial t} + i\, f\, \boldsymbol{U} = \nu_e \frac{\partial^2 \boldsymbol{U}}{\partial z^2}\,. \tag{1.59}$$

Taking the Fourier transform of equation (1.59) with respect to t ($\tilde{\boldsymbol{U}}(z,\omega) = \int_{-\infty}^{\infty} \boldsymbol{U}(z,t)\, e^{-i\omega t}\, dt$) converts it to an ordinary equation,

$$\nu_e \frac{d^2 \tilde{\boldsymbol{U}}}{dz^2} - i(\, f + \omega\,)\tilde{\boldsymbol{U}} = 0\,, \tag{1.60}$$

Its general solution is a sum of two exponents:

$$\tilde{\boldsymbol{U}}(z,\omega) = c_1\ \exp\left[\sqrt{\frac{f+\omega}{2\nu_e}}(1+i)z\right] + c_2\ \exp\left[-\sqrt{\frac{f+\omega}{2\nu_e}}(1+i)z\right]\,. \tag{1.61}$$

Applying the bottom boundary condition, $\tilde{\boldsymbol{U}} = 0$ as $z \longrightarrow \infty$, leads to $c_1 = 0$. The remaining free constant c_2 is determined from the surface condition, $\rho\,\nu_e \frac{\partial \tilde{\boldsymbol{U}}}{\partial z} = -\boldsymbol{\tau}(\omega)$ at $z = 0$, which yields $c_2 = \frac{\boldsymbol{\tau}(\omega)\, e^{-i\pi/4}}{\rho\sqrt{\nu_e}\sqrt{f+\omega}}$. Then, finally,

$$\tilde{\boldsymbol{U}}(z,\omega) = \frac{\boldsymbol{\tau}(\omega)\, e^{-i\pi/4}}{\rho\,\sqrt{\nu_e}\,\sqrt{f+\omega}}\ \exp\left[-\sqrt{\frac{f+\omega}{2\nu_e}}(1+i)z\right]\,. \tag{1.62}$$

The time-dependent solution when the initial velocity is zero (e.g. Gonella [1971]; Lewis and Belcher [2004]) is given in terms of the convolution:

$$\boldsymbol{U}(z,t) = \frac{\boldsymbol{\tau}(t)}{\rho\,\sqrt{\nu}} *_{(t)} \frac{e^{-ift}\, e^{-z^2/4\nu_e t}}{\sqrt{\pi}\,\sqrt{t}}\,. \tag{1.63}$$

The behaviour of the solution obtained above (1.63) was examined when the wind blows suddenly and is directed along the x axis, i.e.

$$\boldsymbol{\tau} = \begin{cases} \tau_x & \text{when } t \geq 0 \\ 0 & \text{when } t < 0 \end{cases} \tag{1.64}$$

Then, the solution (1.63) takes the form.

$$\boldsymbol{U}(z,t) = \frac{\tau_x}{\rho\sqrt{\nu_e\,\pi}} \int_0^t \frac{e^{-if\Theta}\, e^{-z^2/4\nu_e\Theta}}{\sqrt{\Theta}}\, d\Theta\,. \tag{1.65}$$

At the surface, $z = 0$, the velocity is:

$$\boldsymbol{U}_0(t) = \frac{\sqrt{2}\,\tau_x}{\rho\sqrt{f\nu_e}} \left[C\left(\sqrt{\frac{2}{\pi}}\sqrt{ft}\right) - iS\left(\sqrt{\frac{2}{\pi}}\sqrt{ft}\right)\right]\,, \tag{1.66}$$

where $C(x) = \int_0^x \cos(\pi x'^2/2)dx'$ and $S(x) = \int_0^x \sin(\pi x'^2/2)dx'$ are the Fresnel's integrals (e.g. Abramowitz and Stegun [1964]). The deflection angle Φ_0 is given by

$$\Phi_0(t) = -\tan^{-1}\left(\frac{S\left(\sqrt{\frac{2}{\pi}}\sqrt{ft}\right)}{C\left(\sqrt{\frac{2}{\pi}}\sqrt{ft}\right)}\right)\,. \tag{1.67}$$

Figure (1.4) illustrates that there are three stages of the development of the current. At early times, say at, $ft \approx 0.1$, the effect of the Coriolis force is negligible so that the current has almost the same direction as the wind. For times $ft \approx 1$, the current diverts southward due to the Coriolis acceleration. and lastly, at large times ($ft \gg 1$) it tends to the steady-state current (Lewis and Belcher [2004]). Figure (1.5) shows the deflection of surface current from wind as a function of time.

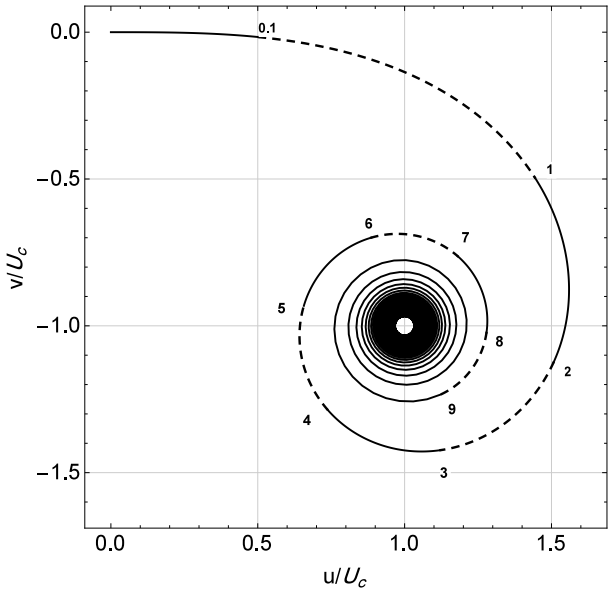

FIGURE 1.4: The normalised drift-current at the surface caused by the wind stress. $U_c = \tau_x/\rho\sqrt{2f\nu_e}$ is the surface velocity scale and the numbers besides the curve represent the non-dimensional time $\tilde{t} = ft$.

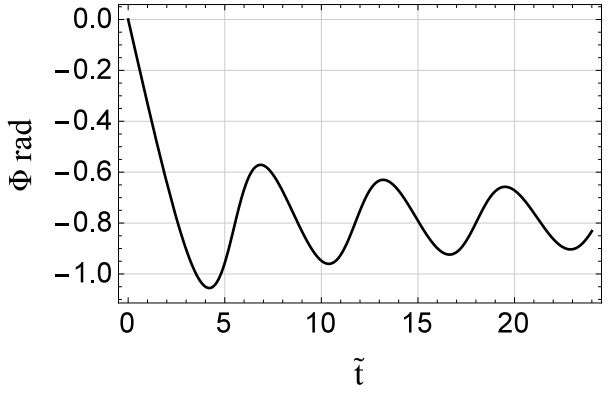

FIGURE 1.5: The deflection angle of surface current to the wind direction.

To find the Ekman transport $\boldsymbol{S}$, the total fluid flux is integrated over the entire depth,

$$\begin{aligned}\boldsymbol{S} &= \frac{\boldsymbol{\tau}(t)}{\rho\sqrt{\nu_e}} * \frac{e^{-ift}}{\sqrt{\pi}\sqrt{t}} \int_0^\infty e^{-z^2/4\nu_e t} dz \\ &= \frac{\tau_x}{\rho f}\, e^{-i\pi/2} \left(e^{-ift} - 1\right) . \end{aligned} \tag{1.68}$$

This result implies that the resultant velocity fluctuates around the value $\frac{\tau_x}{\rho f}\, e^{-i\pi/2}$ (Gonella [1971]).

1.2.4.4 Time-dependent solution with linearly eddy viscosity increasing with depth ($\nu_e(z) = az$)

Since Ekman [1905] there always been an interest in evolving Ekman currents. Numerous attempts were made to find models with more realistic depth dependence of eddy viscosity. one of the first such attempts was made by Madsen [1977]. Here, the vertical eddy viscosity is assumed to be in the form (Madsen [1977]):

$$\nu_e(z) = a\, z\,. \tag{1.69}$$

Equation (1.22) with this form of $\nu_e(z)$ becomes

$$\frac{\partial \boldsymbol{U}}{\partial t} + i\, f\, \boldsymbol{U} = \frac{\partial}{\partial z}\left(a\, z\, \frac{\partial \boldsymbol{U}}{\partial z}\right)\,, \tag{1.70}$$

which is subjected to the boundary conditions (1.23 and 1.25). For simplicity, the ocean is assumed to be initially at rest, $\boldsymbol{U} = 0$ when $t \leq 0$.

The Laplace transform, defined by

$$\hat{\boldsymbol{U}}(z,s) = \mathcal{L}\left\{\boldsymbol{U}(z,t)\right\} = \int_0^\infty e^{-st}\, \boldsymbol{U}(z,t)\, dt\,, \tag{1.71}$$

can be applied to equation (1.70) as it is linear and its coefficients are independent of time, which

$$z\, \frac{\partial^2 \hat{\boldsymbol{U}}}{\partial z^2} + \frac{\partial \hat{\boldsymbol{U}}}{\partial z} - \left(\frac{s + if}{a}\right) \hat{\boldsymbol{U}} = 0\,. \tag{1.72}$$

Also the Laplace transform is applied to the boundary conditions

$$\mathcal{L}\left\{\frac{\boldsymbol{\tau}(t)}{\rho}\right\} = \mathcal{L}\left\{\frac{\tau_x(t)}{\rho} + i\frac{\tau_y(t)}{\rho}\right\} = -a\, z\, \frac{\partial \hat{\boldsymbol{U}}}{\partial z} \quad \text{at} \quad z = 0\,, \tag{1.73}$$

and

$$\hat{\boldsymbol{U}} \to 0 \quad \text{as} \quad z \to \infty \,. \tag{1.74}$$

The governing equation (1.72) can be then written as follows

$$\xi \, \frac{d^2\hat{\boldsymbol{U}}}{d\xi^2} + \frac{d\hat{\boldsymbol{U}}}{d\xi} - \hat{\boldsymbol{U}} = 0 \,, \tag{1.75}$$

where $\xi = \frac{z(s+if)}{a}$ is the non-dimensional vertical variable. The general solution of this equation is given in terms of Bessel functions.

$$\hat{\boldsymbol{U}}(z,s) = c_1 \, I_0 \left(2\sqrt{\xi}\right) + c_2 \, K_0 \left(2\sqrt{\xi}\right) \,, \tag{1.76}$$

where I_0 and K_0 are the modified Bessel function of the first and second kind, respectively.

For deep water case according to equation (1.74), the constant c_1 must be zero, which reduces (1.76) to a simple expression

$$\hat{\boldsymbol{U}}(z,s) = c_2 \, K_0 \left(2\sqrt{\xi}\right) \,. \tag{1.77}$$

To find c_2 we applying the surface boundary condition (1.73) in terms of the dimensionless variable ξ,

$$a\sqrt{\xi} \; c_2 \; K_1 \left(2\sqrt{\xi}\right) = \mathcal{L}\left\{\frac{\tau(t)}{\rho}\right\} \quad as \;\; \xi \to 0 \,. \tag{1.78}$$

Since the assumption of the modified Bessel function of the second kind for small arguments $K_1 \to 1/(2\sqrt{\xi})$, one obtains

$$c_2 = \frac{2}{a} \, \mathcal{L}\left\{\frac{\tau(t)}{\rho}\right\} \,. \tag{1.79}$$

Then, the solution in the Laplace space becomes (Madsen [1977]):

$$\hat{\boldsymbol{U}}(z,s) = \frac{2}{a}\,\mathcal{L}\left\{\frac{\boldsymbol{\tau}(t)}{\rho}\right\} K_0\left(2\sqrt{\xi}\right) . \tag{1.80}$$

Since

$$\mathcal{L}\left\{\frac{1}{2t}\,e^{-ift}\,e^{-z/at}\right\} = K_0\left(2\sqrt{\xi}\right) \quad ; \xi = \frac{z(s+if)}{a} . \tag{1.81}$$

it follows that, the solution for the Ekman current in the convolution form is

$$\boldsymbol{U}(z,t) = \frac{1}{a}\int_0^t \frac{\tau_x(t-\Theta) + i\tau_y(t-\Theta)}{\rho} e^{-if\Theta}\,\frac{1}{\Theta}\,e^{-z/a\Theta}\,d\Theta . \tag{1.82}$$

The behaviour of the solution obtained above (1.82) was examined when the wind stress is the Heaviside step function.

$$\boldsymbol{\tau} = \begin{cases} \tau_x & ; t < 0 \\ 0 & ; t \geq 0 \end{cases} \tag{1.83}$$

which means that the wind blows suddenly on the ocean surface, and it is directed along the x axis.

The given solution by equation (1.82) becomes

$$\boldsymbol{U}(z,t) = u + iv = \frac{\tau_x}{a\,\rho}\int_0^t \frac{1}{\Theta}\,e^{-if\Theta}\,e^{-z/\kappa u_*\Theta}\,d\Theta . \tag{1.84}$$

Although the classical solution and Madsen's solution (1.84) are almost identical in appearance, there is a marked difference in the behaviour of both solutions near the surface ($z \to 0$). At $z = 0$, the classical solution is expressed in terms of convergent Fresnel integrals, while a divergent cosine integral appears in the real part of Madsen's solution and this is because of the assumption of the vertical eddy viscosity. Madsen's

solution shows that the steady state is reached more rapidly than the classical Ekman solution (see figure 1.6).

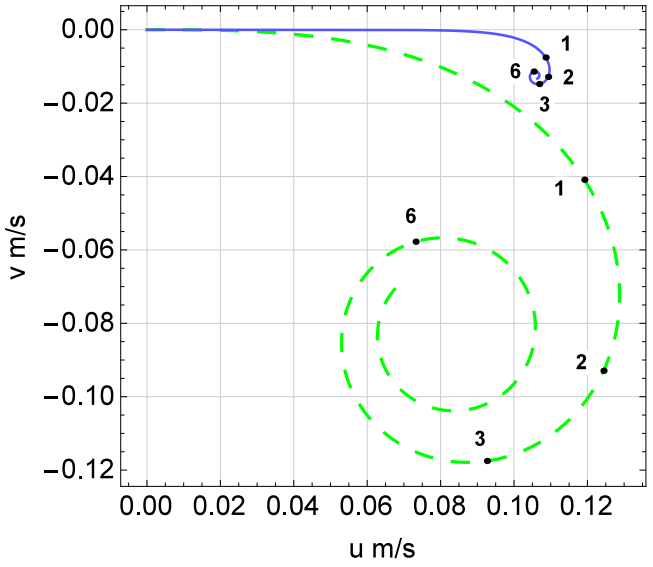

FIGURE 1.6: The development of surface current caused by a sudden increase of wind. The classical Ekman model is shown by dashed line, and Madsen's model is shown by solid line. parameters values are $f = 10^{-4}\text{s}^{-1}$, $\rho = 1027\text{kg m}^{-3}$, $\tau_x = 0.175\text{N m}^{-2}$, and $\nu_e \approx 0.02\ \text{m}^2\text{s}^{-1}$. The numbers besides the curve represent the non-dimensional time $\tilde{t} = ft$.

1.2.4.5 Time-dependent solution in the model with eddy viscosity increasing with depth ($\nu_e(z) = az + b$)

For depth-dependent eddy viscosity profile in the form $\nu_e(z) = az + b = a(z_0 + z)$ (z_0 is the roughness length scale which is introduced to avoid the singularity appearing at the surface in Madsen's model), the equation of motion takes the form (Elipot and Gille [2009]):

$$\frac{\partial \boldsymbol{U}}{\partial t} + i\, f\, \boldsymbol{U} = \frac{\partial}{\partial z}\left(a(z_0 + z)\,\frac{\partial \boldsymbol{U}}{\partial z}\right). \tag{1.85}$$

On taking the Fourier transform with respect to t, equation (1.85) transforms to:

$$a\,(z_0 + z)\frac{\partial^2 \tilde{\boldsymbol{U}}}{\partial z^2} + a\,\frac{\partial \tilde{\boldsymbol{U}}}{\partial z} - i(f + \omega)\,\tilde{\boldsymbol{U}} = 0\,. \tag{1.86}$$

Introducing the nondimensional variable:

$$\bar{\xi} = 2\sqrt{\frac{i(z_0+z)}{\mathtt{n}_2}};\ \ \mathtt{n}_2 = \frac{a}{f+\omega}, \tag{1.87}$$

reduces equation (1.86) to the following form:

$$\frac{d^2\tilde{\boldsymbol{U}}}{d\bar{\xi}^2} + \frac{1}{\bar{\xi}}\frac{d\tilde{\boldsymbol{U}}}{d\bar{\xi}} - \tilde{\boldsymbol{U}} = 0\,. \tag{1.88}$$

The general solution of this equation in terms of Bessel functions is:

$$\tilde{\boldsymbol{U}} = c_1\, I_0[\bar{\xi}] + c_2\, K_0[\bar{\xi}]\,. \tag{1.89}$$

where c_1 and c_2 are arbitrary constants. Elipot and Gille [2009] derived the solution of this model in Fourier space for three different types of conditions at the bottom (velocity vanishes at deep ocean, no-slip condition and shear stress vanishes at the bottom):

Applying the transformed surface condition $(-\rho\,\nu_e(0)\,\tilde{\boldsymbol{U}}' = \boldsymbol{\tau}(\omega))$ and $\boldsymbol{U} \to 0$

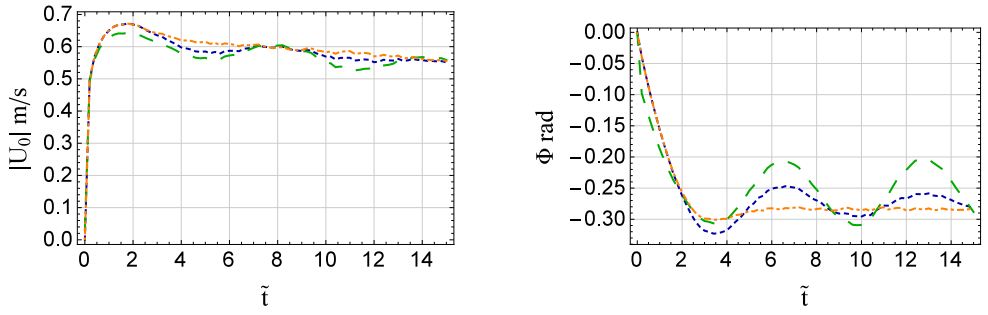

(a) (b)

FIGURE 1.7: Evolution of Ekman current caused by a sharp increase of wind in Elipot and Gille [2009] models: one-layer of infinite depth is shown by blue dotted line, one-layer of finite depth is shown by orange dot-dashed line, and one-layer with shear vanishing at the base is shown by green dashed line. (a) The magnitude of the surface velocity. (b) The angle between the surface current and the wind. The parameters are taken from eddy viscosity profile derived by Zikanov et al. [2003] for wind speed: $U_{10} = 10$ m s^{-1}.

as $z \to \infty$ gives a general solution in the form:

$$\tilde{\boldsymbol{U}}(z,\omega) = \frac{\boldsymbol{\tau}(\omega)\, K_0[\bar{\xi}(z)]}{\rho\,\sqrt{i\,b\,(f+\omega)}\, K_1[\bar{\xi}(0)]}\,. \tag{1.90}$$

and by applying the transformed surface condition ($-\rho\,\nu_e(0)\,\tilde{\boldsymbol{U}}' = \boldsymbol{\tau}(\omega)$) and no-slip conduction ($\boldsymbol{U} = 0$ at $z = D$) gives a general solution in the form:

$$\tilde{\boldsymbol{U}}(z,\omega) = \frac{\boldsymbol{\tau}(\omega)\,\left(I_0[\bar{\xi}(D)]\, K_0[\bar{\xi}(z)] - K_0[\bar{\xi}(D)]\, I_0[\bar{\xi}(z)]\right)}{\rho\,\sqrt{i\,b\,(f+\omega)}\,\left(I_1[\bar{\xi}(0)]\, K_0[\bar{\xi}(D)] + K_1[\bar{\xi}(0)]\, I_0[\bar{\xi}(D)]\right)}\,. \tag{1.91}$$

Also, a general solution in the form:

$$\tilde{\boldsymbol{U}}(z,\omega) = \frac{\boldsymbol{\tau}(\omega)\,\left(I_0[\bar{\xi}(z)]\, K_1[\bar{\xi}(D)] + K_0[\bar{\xi}(z)]\, I_1[\bar{\xi}(D)]\right)}{\rho\,\sqrt{i\,b\,(f+\omega)}\,\left(I_1[\bar{\xi}(D)]\, K_1[\bar{\xi}(0)] - K_1[\bar{\xi}(D)]\, I_1[\bar{\xi}(0)]\right)}\,. \tag{1.92}$$

is derived by applying the transformed surface condition ($-\rho\,\nu_e(0)\,\tilde{\boldsymbol{U}}' = \boldsymbol{\tau}(\omega)$) and $\tilde{\boldsymbol{U}}' = 0$ at $z = D$. For sharp increase of wind, the surface current of these three models is shown in figure (1.7). Figure (1.8) gives the sketches of depth dependent eddy viscosity profiles, and solutions in Fourier space for some of these profiles are provided in table (1.3).

The drawbacks of these models are easy to see:

1. obviously the eddy viscosity can not increase to infinity.
2. The choice of the boundary conditions at the bottom of the mixed layer is not justified.
3. The eddy viscosity is assumed to be linear in z and constant in time, these assumptions are very restrictive.

In the next chapters we will address these shortcomings by studying non-steady dynamics in Zikanov et al. [2003] model which is justified by LES, we will also model the stratified flow by considering two-layer model with different constant viscosities, and time and depth dependent eddy viscosity will also be considered.

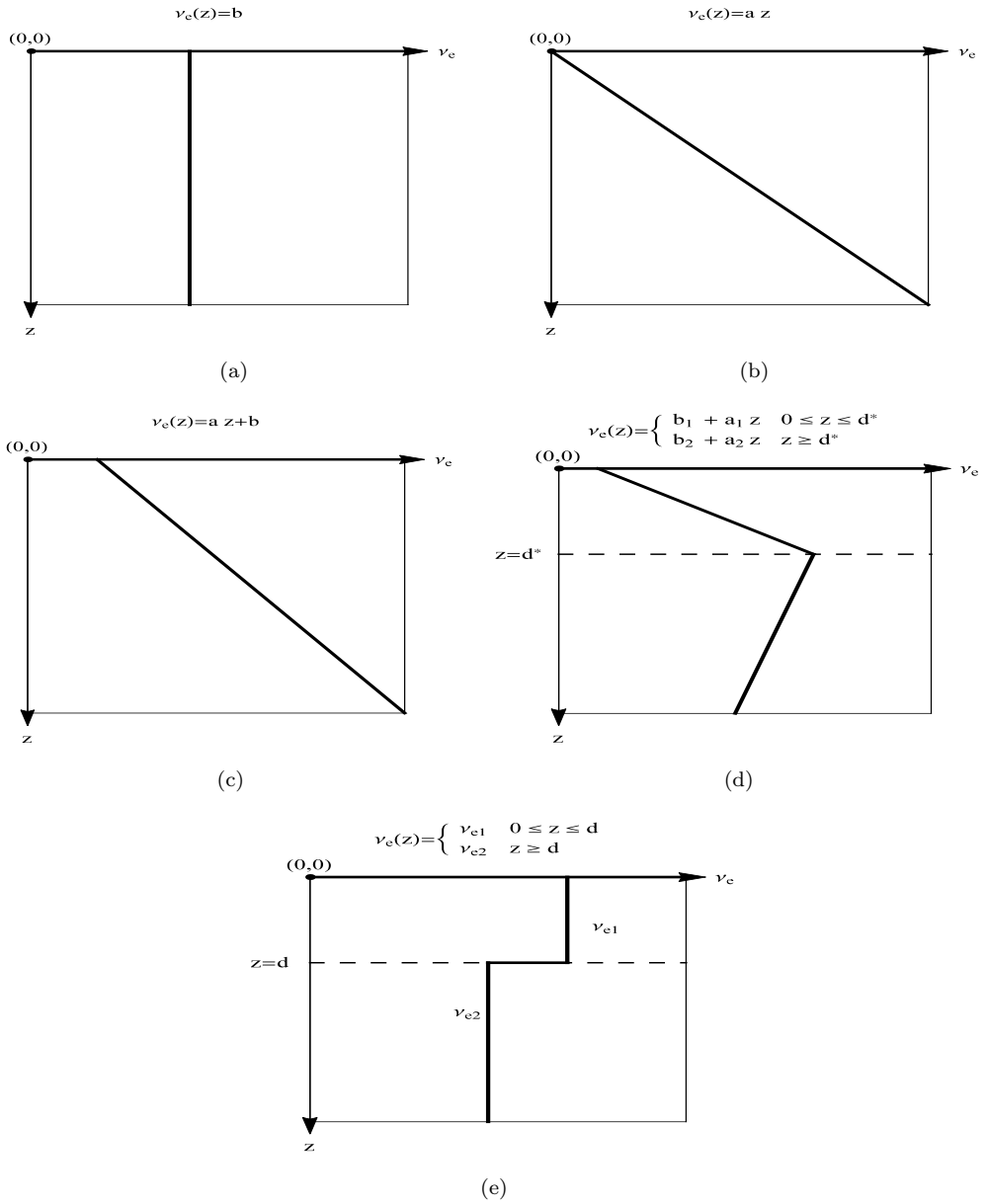

FIGURE 1.8: Sketch of uniform and depth-dependence eddy viscosity profiles considered in the thesis. (a) Eddy viscosity is constant in both time and depth (Ekman [1905]). (b) Eddy viscosity is constant in time and linear in depth with zero value at the surface (Madsen [1977]). (c) Viscosity linearly dependent on depth with a finite surface value (modification of Madsen's model) (Elipot and Gille [2009]). (d) Eddy viscosity predicted by LES and approximated by a piecewise-linear profile (Zikanov et al. [2003]), this profile is considered in §2. (e) Depth-dependent eddy viscosity profile in two-layer model considered in §3.

TABLE 1.3: The solution of equation (1.22) in Fourier space for different profiles of eddy viscosity and different boundary condition at the base (Ekman [1905], Madsen [1977], Lewis and Belcher [2004], Elipot and Gille [2009]). $\boldsymbol{\mathcal{U}}_c = \boldsymbol{\tau}(\omega)/(\rho\sqrt{ib(f+\omega)})$, $\mathtt{n}_1 = \sqrt{2b/(f+\omega)}$, $\bar{\xi} = 2\sqrt{i(z_0+z)/\mathtt{n}_2}$ and $\mathtt{n}_2 = a/(f+\omega)$

eddy viscosity profile	velocity vanishes at deep ocean	no-slip condition	shear vanishes at the bottom of the layer
$\nu_e(z) = b$	$\boldsymbol{\mathcal{U}}_c e^{-z(1+i)/\mathtt{n}_1}$	$\boldsymbol{\mathcal{U}}_c \frac{\sinh\left[(1+i)(D-z)/\mathtt{n}_1\right]}{\cosh\left[(1+i)D/\mathtt{n}_1\right]}$	$\boldsymbol{\mathcal{U}}_c \frac{\cosh\left[(1+i)(D-z)/\mathtt{n}_1\right]}{\sinh\left[(1+i)D/\mathtt{n}_1\right]}$
$\nu_e(z) = az$	$\frac{2}{\rho a} K_0\left[2\sqrt{\frac{iz}{\mathtt{n}_2}}\right]$	$\frac{2}{\rho a}\left(K_0\left[2\sqrt{\frac{iz}{\mathtt{n}_2}}\right] - \frac{K_0\left[2\sqrt{\frac{iD}{\mathtt{n}_2}}\right] I_0\left[2\sqrt{\frac{iz}{\mathtt{n}_2}}\right]}{I_0\left[2\sqrt{\frac{iD}{\mathtt{n}_2}}\right]}\right)$	$\frac{2}{\rho a}\left(K_0\left[2\sqrt{\frac{iz}{\mathtt{n}_2}}\right] + \frac{K_1\left[2\sqrt{\frac{iD}{\mathtt{n}_2}}\right] I_0\left[2\sqrt{\frac{iz}{\mathtt{n}_2}}\right]}{I_1\left[2\sqrt{\frac{iD}{\mathtt{n}_2}}\right]}\right)$
$\nu_e(z) = az + b$	$\boldsymbol{\mathcal{U}}_c \frac{K_0\left[\bar{\xi}(z)\right]}{K_1\left[\bar{\xi}(0)\right]}$	$\boldsymbol{\mathcal{U}}_c \frac{I_0\left[\bar{\xi}(D)\right] K_0\left[\bar{\xi}(z)\right] - K_0\left[\bar{\xi}(D)\right] I_0\left[\bar{\xi}(z)\right]}{I_1\left[\bar{\xi}(0)\right] K_0\left[\bar{\xi}(D)\right] + K_1\left[\bar{\xi}(0)\right] I_0\left[\bar{\xi}(D)\right]}$	$\boldsymbol{\mathcal{U}}_c \frac{I_0\left[\bar{\xi}(z)\right] K_1\left[\bar{\xi}(D)\right] + K_0\left[\bar{\xi}(z)\right] I_1\left[\bar{\xi}(D)\right]}{I_1\left[\bar{\xi}(D)\right] K_1\left[\bar{\xi}(0)\right] - K_1\left[\bar{\xi}(D)\right] I_1\left[\bar{\xi}(0)\right]}$

1.3 Open questions

Despite more than a century of numerous theoretical and observational studies of Ekman currents, a number of basic questions remain open which we attempt to address in this thesis.

(i) In his original work Ekman assumed the eddy viscosity to be constant in time and space. Although a number of models with vertically varying viscosity has been considered, it is not clear what is the right model and, moreover, whether such simple parameterisations capture reality well. Zikanov et al. [2003] put forward a parameterisation of vertical viscosity profile supported by Large Eddy simulations for steady conditions (and under other additional assumptions). The degree of applicability of the Zikanov et al. [2003] parametirisation to non-steady winds is not clear, but this is a reasonable hypothesis we adopt. The basic question we try to address is whether the use of this more advanced model supported by LES simulations yields noticeable advantages over more simple models commonly used in the literature (e.g. Elipot and Gille [2009]; Lewis and Belcher [2004]).

(ii) The second fundamental question we will attempt to address is how density stratification (diurnal or seasonal pycnocline) affects the Ekman surface currents and whether it might be possible to probe remotely the presence and characteristics of the upper ocean stratification.

(iii) All existing models of the Ekman current response to varying wind employ (at best) only depth dependent eddy viscosity. This is an obvious oversimplification, but its implications are not clear. We will examine the implications of this assumption within the framework of the Ekman type models.

(iv) It is known that the Stokes drift can strongly affect Ekman currents and this was considered in the literature. However, this consideration was confined to the models of constant in time and depth eddy viscosity or only linearly depth dependent eddy viscosity (constant in time), while the spectrum of surface

waves was parameterized by a single harmonic not dependent on time. We will address these major shortcomings of the existing models. We will analyse the effects of the Stokes drift on the Ekman current dynamics without these restrictive assumptions by considering time and depth dependent eddy viscosity profiles with the Stokes drift evolving as an arbitrary function of time.

(v) It is known that the steady Ekman current is unstable and can evolve into rolls. It is not clear whether the eddy viscosity employed in the Ekman models assumes spatial averaging over such patterns. It is also not clear how the emergence of rolls obtained numerically by many authors (e.g. Leibovich and Lele [1985]; Wirth [2010]) can be compatible with the LES simulations by Zikanov et al. [2003] resulting in steady Ekman currents. We will try to shed new light on the issue of what spatial and temporal scales are being averaged out in the commonly adopted picture of Ekman currents.

1.4 Structure of the thesis

The present chapter gives a review of the existing Ekamn models which we consider a natural starting point to understand an essential aspect of the upper ocean physics.

1. In chapter 2, an explicit analytic solution of Navier-Stokes equations, based upon Zikanov et al. [2003] parameterisation of eddy viscosity, is derived. This chapter also provides a comparison between our refined model and the existing models with a simpler depth dependent eddy viscosity profile.

2. In chapter 3, we extend the classical one-layer model with a constant eddy viscosity by considering two layers: the top one (turbulent mixed layer) is characterized by a constant eddy viscosity, while the laminar flow below (stratified layer) has a much smaller constant value of eddy viscosity. This chapter also includes analyses for both steady and unsteady solutions.

3. In chapter 4, both time and depth dependent of the eddy viscosity is considered, the exact general solution of Navier-Stokes equations for non-stratified

deep ocean has been found and analysed for basic situations of varying wind: periodic wind, increasing wind, and switch off of the wind. Also in this chapter, the Stokes-Ekman equations with time and depth dependent viscosity, an arbitrary time dependent Stokes drift and an arbitrary wave spectrum are analysed. General solution has been derived for separable time and depth dependent eddy viscosity. Finally, concluding remarks are presented in chapter 5.

Chapter 2

Ekman currents under variable wind in non-stratified deep ocean

2.1 Introduction

The upper ocean Ekman Boundary layer has long been the subject of numerous observational and theoretical studies, a variety of parametrizations and estimated values of eddy viscosity ν_e were provided by these studies. Huang [1979] and Santiago-Mandujano and Firing [1990] present extended reviews of earlier studies. Observations showed that the structure of the mean current in the upper ocean has a spiral shape in which the current decreases and turns to the right with depth. These spirals resemble the theoretical Ekman spirals, the essential difference is that the decaying rate of the current with increasing depth exceeds its rotating rate to the right which means these spirals are flatter than the classical Ekman spirals (e.g Price et al. [1987]; Price and Sundermeyer [1999]; Chereskin [1995]). The observed deflection of the current at the surface ranges between $10 - 45^\circ$ (Huang [1979]) while the current vector below the surface (from about 5 to 20 m depth) is shifted to around 75° from the wind stress (Price and Sundermeyer [1999]). The vertical mixing in the upper

ocean occurs due to turbulence. In the Ekman [1905] theory transfer of momentum could be modelled as a diffusion of momentum with an effective eddy viscosity, ν_e, orders of magnitude larger than the molecular viscosity. This has been justified, at least for a steady-state case, by Zikanov et al. [2003]. In this chapter we assume this to be true for unsteady case as well. Additionally, the large eddy simulations (LES) (Zikanov et al. [2003]) of the ocean mixed layer suggest that the eddy viscosity profile is more complicated than it is commonly assumed, the computed eddy viscosity varies substantially in the turbulent boundary layer and has a convex shape (e.g Large et al. [1994]; McWilliams et al. [1997]; Zikanov et al. [2003]) where in the lower half of the mixed layer it roughly decreases linearly. Zikanov et al. [2003] have shown that the eddy viscosity profile obtained numerically with Large Eddy Simulations approach can be well approximated by a piecewise-linear profile of viscosity in the form $\nu_e(z) = a\,z + b$. The coefficients of this parametrisation depend on the surface tangential stress parametrised by u_* (friction velocity) and on the latitude through Coriolis parameters. Furthermore, a direct numerical study (DNS) of the planetary Ekman layer also showed that the flow is affected by latitude and wind direction (Coleman et al. [1990]). Note that although only the Coriolis parameter f enters explicitly into the formula, the horizontal component of the Coriolis $\tilde{f}$ affects the turbulence and dependence on it is implicit in this formula. The effects of the surface waves and the density stratification are not considered in the Zikanov's model. An analytical solution of the problem for an infinitely deep ocean with an eddy viscosity that varies linearly with depth was examined first by Madsen [1977]. Madsen suggested that the viscosity increases linearly from zero at the free surface and it takes the form $\nu_e = \kappa\, u_*\, z$ where $u_* = \sqrt{\tau/\rho}$ is the friction velocity and $\kappa = 0.4$ is the Von Karman's constant. Madsen [1977] avoided the logarithmic singularity which appears in the solution at $z = 0$ by introducing a sea surface roughness length scale z_0 and evaluating the surface velocity at this value instead. Although from the mathematical perspective this leads to an inconsistency between the surface current and the shear stress boundary conditions at the surface, the physical results are reasonable (Lewis and Belcher [2004]). The surface current in Madsen's model is deflected to the right by approximately 10° from the wind direction and this is

much lower than the (45°) angle predicted by Ekman [1905]. Furthermore, for different depth-dependent viscosity profiles (constant, linear, exponential, varying as a power) the problem was also theoretically investigated by Jordan and Baker [1980]. Modification of the eddy viscosity dependence on depth directly by adding the vertical roughness length scale to it $(\nu_e(z) = a(z_0 + z))$ eliminates the singularity (the velocity at the surface becomes finite quantity) which appeared in Madsen's model. Using the correspondingly modified eddy viscosity profile, the problem was examined for three different conditions at the base of the mixed layer (Elipot and Gille [2009]). A steady-state solution of the problem for a more complicated depth-dependent eddy viscosity profile, piecewise-linear, was investigated by Zikanov et al. [2003], it showed that the angle between the surface current and the wind stress is 28.5°. Our aim is to clarify the following open questions:

(i) What are the main features of the Ekman current for the numerically justified eddy viscosity profile by Zikanov et al. [2003] under time dependent wind (under the adopted assumptions)?

(ii) What are the differences in behaviour of the solution for different viscosity profiles and for what parameters the differences are essential?

(iii) When Zikanov's parameterisation can be approximated by a one-layer model with linear viscosity profile?

(iv) Are Ekman currents stable with respect to short scale perturbations?

This chapter is organised as follows: §2.2 presents the problem formulation. §2.3 provides the exact general solution of the model in terms of Green functions. This section also includes a comparisons between the present solution and other models with linear viscosity profile. Lastly, the conclusion is provided in §2.4.

2.2 The mathematical model

We consider a horizontally uniform motions of an incompressible rotating non-stratified viscous deep fluid of uniform depth h, which describes by equation (1.22) with a piecewise-linear eddy viscosity profile (see figure 2.1):

$$\nu_e(z) = a_j z + b_j = a_j(z_j + z); \quad j = 1, 2\,. \tag{2.1}$$

where z_1 and z_2 are the roughness length scales of sea surface, subjected to the surface boundary condition (1.22). The shear and the velocity are assumed to be continuous at the maximum of the eddy viscosity ($z = d^*$). At deep ocean, $z \gg h$, the velocity vanishes. By taking Fourier transform with respect to t, equation (1.22) transforms into the following ordinary differential equation:

$$\frac{\partial}{\partial z}\left(\nu_{ej}(z)\,\frac{\partial \tilde{\boldsymbol{U}}_j}{\partial z}\right) - i(f+\omega)\,\tilde{\boldsymbol{U}}_j = 0, \qquad \text{where} \qquad \tilde{\boldsymbol{U}}_j(z,\omega) = \int_{-\infty}^{\infty} \boldsymbol{U}_j(z,t) e^{-i\omega t}\,dt\,. \tag{2.2}$$

Subjected to the following boundary conditions:

$$\nu_{e1}(z)\frac{\partial \tilde{\boldsymbol{U}}_1}{\partial z}\bigg|_{z=0} = \frac{-\boldsymbol{\tau}(\omega)}{\rho}, \tag{2.3a}$$

$$\tilde{\boldsymbol{U}}_1|_{z=d^*} = \tilde{\boldsymbol{U}}_2|_{z=d^*}, \tag{2.3b}$$

$$\nu_{e1}(z)\frac{\partial \tilde{\boldsymbol{U}}_1}{\partial z}\bigg|_{z=d^*} = \nu_{e2}(z)\frac{\partial \tilde{\boldsymbol{U}}_2}{\partial z}\bigg|_{z=d^*}, \tag{2.3c}$$

$$\tilde{\boldsymbol{U}}_2|_{z=h} = 0. \tag{2.3d}$$

Under the Zikanov et al. [2003] parametrisation it reduces to

$$a_j\,(z_j + z)\frac{\partial^2 \tilde{\boldsymbol{U}}_j}{\partial z^2} + a_j\,\frac{\partial \tilde{\boldsymbol{U}}_j}{\partial z} - i(f+\omega)\,\tilde{\boldsymbol{U}}_j = 0\,. \tag{2.4}$$

In the next sections we derive and analyse solutions of these equations. We show that these solutions are exact solutions of the Navier-Stokes equations for the chosen ν_e.

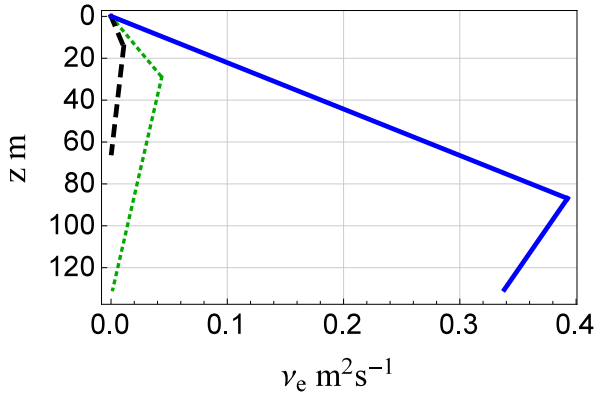

FIGURE 2.1: The Zikanov et al. [2003] viscosity profile for three different wind speeds: black dashed line: $U_{10} = 5\,\mathrm{m\ s^{-1}}$, $a_1 \approx 7.5 \times 10^{-4}$, $b_1 \approx 8.41 \times 10^{-6}$, $a_2 \approx -2.1 \times 10^{-4}$, $b_2 \approx 1.4 \times 10^{-2}$ and $d^* \approx 14.5\,\mathrm{m}$, green dotted line: $U_{10} = 10\,\mathrm{m\ s^{-1}}$, $a_1 \approx 1.5 \times 10^{-3}$, $b_1 \approx 3.4 \times 10^{-5}$, $a_2 \approx -4.2 \times 10^{-4}$, $b_2 \approx 55.7 \times 10^{-3}$, and $d^* \approx 28.98\,\mathrm{m}$, and blue solid line: $U_{10} = 30\,\mathrm{m\ s^{-1}}$, $a_1 \approx 4.5 \times 10^{-3}$, $b_1 \approx 3.02 \times 10^{-4}$, $a_2 \approx -1.2 \times 10^{-3}$, $b_2 \approx 5.01 \times 10^{-1}$, and $d^* \approx 86.9\,\mathrm{m}$ (Zikanov et al. [2003]).

2.3 General solution

To solve the Ekman equations (2.4) subjected to the boundary conditions (2.3), it is convenient to introduce the dimensionless vertical variable:

$$\xi = 2\sqrt{\frac{i(z_j + z)}{\alpha_j}};\ \ \alpha_j = \frac{a_j}{f + \omega}\,. \tag{2.5}$$

Then the equation of motion (2.4) takes the form

$$\frac{d^2\tilde{\boldsymbol{U}}_j}{d\xi^2} + \frac{1}{\xi}\frac{d\tilde{\boldsymbol{U}}_j}{d\xi} - \tilde{\boldsymbol{U}}_j = 0\,. \tag{2.6}$$

Its general solution in terms of Bessel functions can be presented as

$$\tilde{\boldsymbol{U}} = c_1\, I_0[\xi] + c_2\, K_0[\xi]\,, \tag{2.7}$$

where $I_0[.]$ is the zeroth order modified Bessel function of the first kind, $K_0[.]$ is the zeroth order modified Bessel function of the second kind and ξ is given by equation (2.5).

Here, $\nu_{e1} = a_1(z_1 + z)$ and $\nu_{e2} = a_2(z_2 + z)$ where z_1 and z_2 are the roughness length scales for the corresponding layer.

The general solution of the equation (2.6) subject to the boundary conditions (2.3) can be written as

$$\tilde{\boldsymbol{U}}_1 = A_1\, I_0[\xi_1] + B_1\, K_0[\xi_1]; \quad 0 \le z \le d^*\,, \tag{2.8a}$$

$$\tilde{\boldsymbol{U}}_2 = A_2\, I_0[\xi_2] + B_2\, K_0[\xi_2]; \quad d^* \le z \le h\,, \tag{2.8b}$$

where

$$\xi_1 = 2\sqrt{\frac{i(z_1+z)}{\alpha_1}};\;\; \alpha_1 = \frac{a_1}{f+\omega}\,,$$
$$\xi_2 = 2\sqrt{\frac{i(z_2+z)}{\alpha_2}};\;\; \alpha_2 = \frac{a_2}{f+\omega}\,.$$

The general solution for $z \le d^*$ satisfying the boundary conditions takes the form:

$$\boldsymbol{U}_1(z,t) = \frac{1}{2\,\pi}\int_{-\infty}^{\infty} \tilde{\boldsymbol{U}}_1(z,\omega)\, e^{i\,\omega\, t}\, d\omega, \tag{2.9a}$$

where

$$\tilde{\boldsymbol{U}}_1(z,\omega) = \frac{2\,\boldsymbol{\tau}(\omega)\Big(C_1\, I_0[\xi_1(z)] + C_2\, K_0[\xi_1(z)]\Big)}{a_1\;\rho\;\xi_1(0)\;(C_3+C_4)}, \tag{2.9b}$$

and

$$C_1 = \frac{a_1}{2}\,\xi_1(d^*)\,K_1[\xi_1(d^*)]\,(\,K_0[\xi_2(d^*)]\,I_0[\xi_2(h)] - I_0[\xi_2(d^*)]\,K_0[\xi_2(h)]\,)$$
$$-\,\frac{a_2}{2}\,\xi_2(d^*)\,K_0[\xi_1(d^*)]\,(\,I_1[\xi_2(d^*)]\,K_0[\xi_2(h)] + K_1[\xi_2(d^*)]\,I_0[\xi_2(h)]\,);$$

$$C_2 = \frac{a_1}{2}\,\xi_1(d^*)\,I_1[\xi_1(d^*)]\,(\,K_0[\xi_2(d^*)]I_0[\xi_2(h)] - I_0[\xi_2(d^*)]\,K_0[\xi_2(h))]\,)+$$
$$\frac{a_2}{2}\,\xi_2(d^*)\,I_0[\xi_1(d^*)]\,(I_1[\xi_2(d^*)]\,K_0[\xi_2(h)] + K_1[\xi_2(d^*)]\,I_0[\xi_2(h)]\,);$$

$$C_3 = \frac{a_1}{2}\,\xi_1(d^*)\,(\,K_1[\xi_1(0)]\,I_1[\xi_1(d^*)] - I_1[\xi_1(0)]\,K_1[\xi_1(d^*)]\,)\times$$
$$(K_0[\xi_2(d^*)]\,I_0[\xi_2(h)] - I_0[\xi_2(d^*)]\,K_0[\xi_2(h)]\,);$$

$$C_4 = \frac{a_2}{2}\,\xi_2(d^*)\,(I_1[\xi_1(0)]\,K_0[\xi_1(d^*)] + K_1[\xi_1(0)]\,I_0[\xi_1(d^*)]\,)\times$$
$$(\,I_1[\xi_2(d^*)]K_0[\xi_2(h)] + K_1[\xi_2(d^*)]\,I_0[\xi_2(h)]\,)\,.$$

Similarly, the general solution in the interval $d^* \leqslant z \leqslant h$ reads:

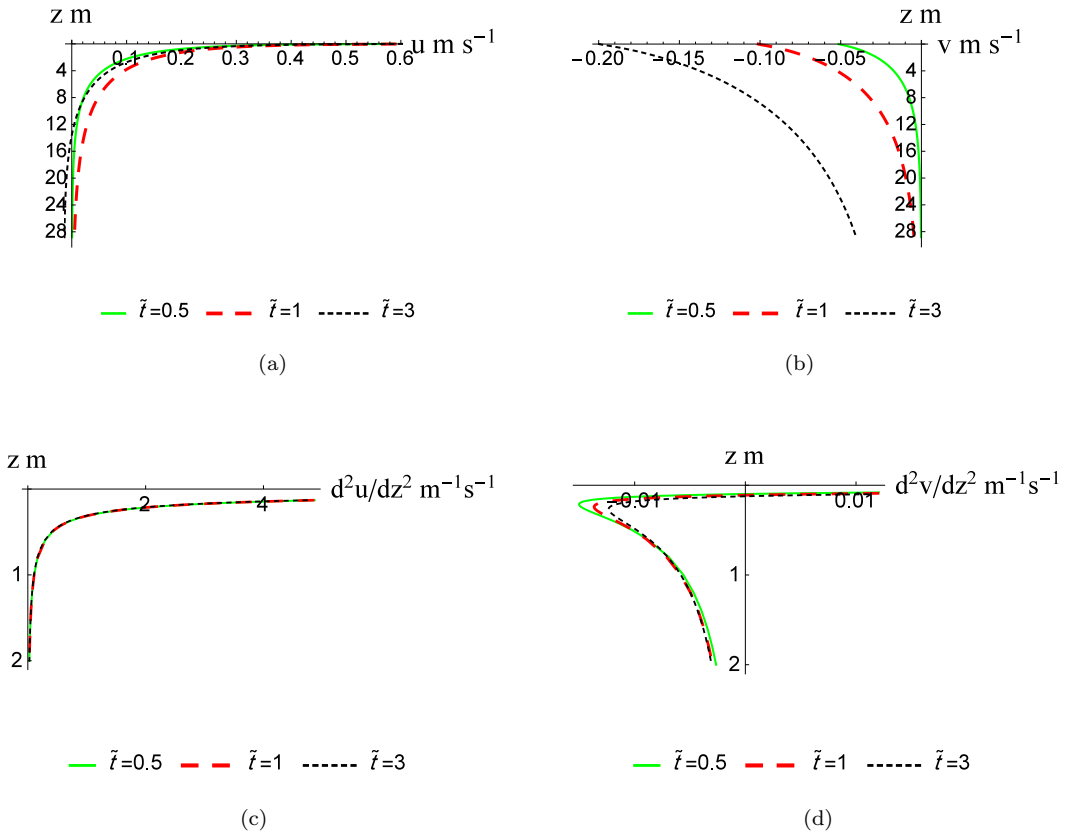

FIGURE 2.2: (a,b) The velocity components in the direction of x and y, respectively. (c,d) The second derivative of x and y velocity components. Parameters values are $\tau = 0.175\,\mathrm{N\ m^{-2}}$, $f = 10^{-4}\,\mathrm{s^{-1}}$, $\rho = 1027\,\mathrm{kg\ m^{-3}}$, $U_{10} = 10\,\mathrm{m\ s^{-1}}$, $a_1 \approx 1.5 \times 10^{-3}$, $b_1 \approx 3.4 \times 10^{-5}$, $a_2 \approx -4.2 \times 10^{-4}$, $b_2 \approx 55.7 \times 10^{-3}$, and $d^* \approx 28.98\,\mathrm{m}$.

$$\boldsymbol{U}_2(z,t) = \frac{1}{2\,\pi}\int_{-\infty}^{\infty} \tilde{\boldsymbol{U}}_2(z,\omega)\,e^{i\,\omega\,t}\,d\omega\,, \tag{2.10a}$$

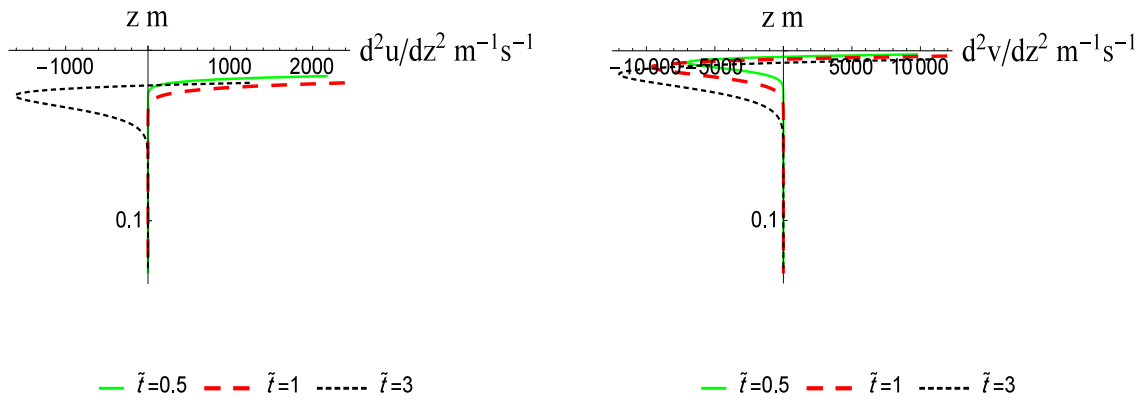

(a) (b)

FIGURE 2.3: (a,b) The second derivative of x and y velocity components for the classical Ekman model. Parameters values are $\tau = 0.175\,\mathrm{N\ m^{-2}}$, $f = 10^{-4}\,\mathrm{s^{-1}}$, $\rho = 1027\,\mathrm{kg\ m^{-3}}$, $U_{10} = 10\,\mathrm{m\ s^{-1}}$, $\nu_e = b_1 \approx 3.4 \times 10^{-5}$.

where

$$\tilde{\boldsymbol{U}}_2(z,\omega) = \frac{\boldsymbol{\tau}(\omega)\left(I_0\left[\xi_2(h)\right]\ K_0[\xi_2(z)] - K_0\left[\xi_2(h)\right)\ I_0\left[\xi_2(z)\right]\right)}{\rho\ \xi_1(0)\ (C_3 + C_4)}\,, \tag{2.10b}$$

and C_3, C_4 are constants given above.

Figure (2.2) shows examples of vertical profiles of both horizontal velocity components and their second derivative at certain times and under a sharp increase of wind. The changing sign of the second derivative suggests that the current caused by sharp increase of wind becomes unstable with respect to inviscid inflectional instabilities. For a comparison, figure (2.3) presents the second derivative of horizontal velocity components of the classical Ekman model. This change of curvature is more pronounced in the classical Ekman model, therefore we expect stronger instability in the classical Ekman model.

2.3.1 The behavior of the transform function

We compare our refined model based upon Zikanov et al. [2003] parameterisation of eddy viscosity with two models with linearly varying eddy viscosity of Elipot and

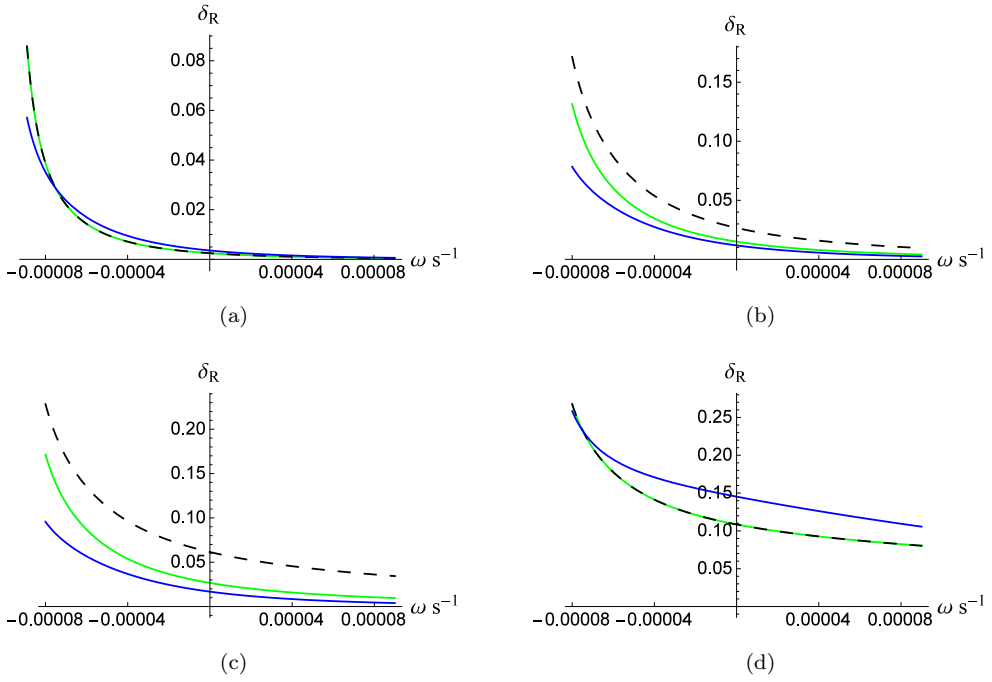

FIGURE 2.4: Dependence of the normalised discrepancy $\delta_R = |\tilde{\boldsymbol{U}}_Z - \tilde{\boldsymbol{U}}_{EG(1)}|/|\tilde{\boldsymbol{U}}_Z|$ on frequency at different depths ((a): $z = 0$, (b): $z = 5$ m, (c): $z = 10$ m, (d): $z = d^*$ m) for different wind speeds: $U_{10} = 5\,\mathrm{m\,s^{-1}}$(black dashed line), $U_{10} = 10\,\mathrm{m\,s^{-1}}$(green solid line), and $U_{10} = 30\,\mathrm{m\,s^{-1}}$(blue solid line). d^* depends on wind strength: $d^* \approx 14.5$ m for $U_{10} = 5\,\mathrm{m\,s^{-1}}$, $d^* \approx 29$ m for $U_{10} = 10\,\mathrm{m\,s^{-1}}$, and $d^* \approx 86.9$ m for $U_{10} = 30\,\mathrm{m\,s^{-1}}$. $\tilde{\boldsymbol{U}}_Z$ and $\tilde{\boldsymbol{U}}_{EG(1)}$ refer to the solution in Fourier space for: a piecewise-linear eddy viscosity model and linear viscosity model ($\nu_1(z) = a_1(z_1 + z)$) for infinitely deep ocean (Elipot and Gille [2009]) respectively.

Gille [2009] with infinitely deep one layer, $\tilde{\boldsymbol{U}}_{EG(1)}$, and shear vanishing at $z = d^*$, $\tilde{\boldsymbol{U}}_{EG(2)}$. By introducing a quantity $\delta_R = |\tilde{\boldsymbol{U}}_Z - \tilde{\boldsymbol{U}}_{EG}|/|\tilde{\boldsymbol{U}}_Z|$ (relative discrepancy) we identify the range of cases where the δ_R is less than a threshold we choose for certainty to be 0.1 for most depths (see figure 2.4) and it exceeds 0.1 (see figure 2.5). We have found that the discrepancy between the refined model and $\tilde{\boldsymbol{U}}_{EG(1)}$, $\tilde{\boldsymbol{U}}_{EG(2)}$ increases with depths and decreases with frequency. It is small for all frequencies outside a vicinity of inertial frequency. It is much smaller for $\tilde{\boldsymbol{U}}_{EG(1)}$ where it exceeds the 0.1 threshold only for large depths and small frequencies. At the surface the discrepancy has been found to be negligible.

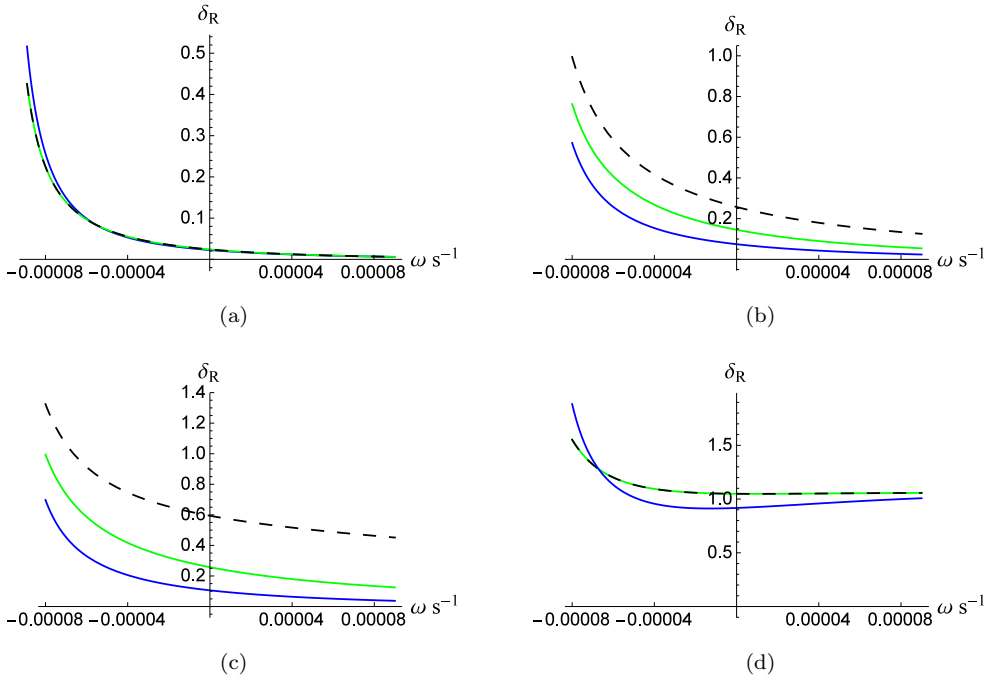

FIGURE 2.5: Dependence of the normalised discrepancy $\delta_R = |\tilde{\boldsymbol{U}}_Z - \tilde{\boldsymbol{U}}_{EG(2)}|/|\tilde{\boldsymbol{U}}_Z|$ on frequency at different depths ((a): $z = 0$, (b): $z = 5$ m, (c): $z = 10$ m, (d): $z = d^*$ m) and for different wind speeds: $U_{10} = 5\,\mathrm{m\ s^{-1}}$(black dashed line), $U_{10} = 10\,\mathrm{m\ s^{-1}}$(green solid line)and $U_{10} = 30\,\mathrm{m\ s^{-1}}$(blue solid line). d^* depends on wind strength: $d^* \approx 14.5$ m for $U_{10} = 5\,\mathrm{m\ s^{-1}}$, $d^* \approx 29$ m for $U_{10} = 10\,\mathrm{m\ s^{-1}}$, and $d^* \approx 86.9$ m for $U_{10} = 30\,\mathrm{m\ s^{-1}}$. $\tilde{\boldsymbol{U}}_Z$ and $\tilde{\boldsymbol{U}}_{EG(2)}$ refer to the solution in Fourier space for: a piecewise-linear eddy viscosity model and linear viscosity model ($\nu_1(z) = a_1(z_1 + z)$) with shear vanishing at $z = d^*$ (Elipot and Gille [2009]) respectively.

2.4 Conclusions

In this chapter we examined depth dependent eddy viscosity model with eddy viscosity profile parameterised on the basis of Large Eddy Simulations (LES) of steady state case (Zikanov et al. [2003]), in which the eddy viscosity changes strongly within the non-stratified fluid. It increases linearly with depth in the upper part of the layer reaching a maximum value at a particular depth depending on wind speed, then it starts to decrease linearly with depth in the lower part.

1. For an arbitrary tangential stress $\boldsymbol{\tau}(t)$, we have found a general solution which describes dynamics of deep non-stratified ocean, this solution is an exact solution to the full Navier-Stokes equations. Since the employed eddy viscosity

model is more sophisticated than those reported in the literature, it is expected that the derived solution will describe reality much more faithfully.

2. Comparisons between the present model and other existing models with a simple form of linearly-depth varying eddy viscosity, show that a reasonable accuracy for a wide range of situations can be obtained from simpler models (one-layer models with linear viscosity profiles). The discrepancy between predictions of our refined model and Elipot and Gille [2009] models with linear eddy viscosity profile is small near the surface, while it proved to be O(1) at the depth d^*, the depth where eddy viscosity attains its maximal value.

3. We have found that all types of Ekman models develop inflection points, which suggests strong instabilities. These instabilities for unsteady Ekman currents have not been reported in the literature. Note that for the examined class of eddy viscosity profile these inflection of profiles invariably occur near the surface where the difference between the models is small.

Analysis of these instabilities for time dependent flows requires massive numerical effort to solve Orr-Sommerfeld equations for wide range of profiles, which goes beyond the scopes of present work. In section §2.3 the parameters of instabilities will be quantified and discussed for a few examples.

Chapter 3

Dynamics of the Ekman currents under varying wind in the two-layer model of stratified ocean

3.1 Introduction

In the upper ocean, the mixed layer and seasonal pycnocline are its most prominent features (e.g. Phillips [1977], Soloviev and Lukas [2013]). In the mixed layer between the ocean free surface and the seasonal pycknocline the temperature and salinity is nearly uniform, which led to the term "mixed layer". The mixed layer depth is influenced by processes that change the stratification: winds, radiative heating and cooling. The thickness of the mixed layer varies with season. During the spring and summer (strong stratification), the mixed layer is relatively shallow, while it is deeper and less prominent in the autumn and much deeper in winter (the seasonal pycnocline disappears in winter and the mixed layer extends to the main pycnocline). The typical depth of the the seasonal pycnocline ranges between 20 m and 200 m. At higher latitudes, the mixed layer depth increases as a result of stronger winds and cooling poleward. Furthermore, the mixed layer in the Southern Hemisphere is thicker than in the Northern Hemisphere. The mixed layer is the layer in direct contact with

the atmosphere and most active in the air-sea interaction. There is very significant momentum and heat exchange with the atmosphere. Its correct modelling is crucial for weather prediction and climate modelling. There is an extensive literature on theoretical, numerical and experimental studies on the variety of physical processes in the mixed layer partly reviewed in the chapter 1, see also (Soloviev and Lukas [2013]). However, at present a number of fundamental questions remain open.

Here we will attempt to address these questions employing an extension of the Ekman model. In the Ekman type models the turbulence is characterized by a single parameter - turbulent viscosity ν_e ,which can, in principle, be both depth and time dependent. It is well known that stratification strongly suppresses turbulence (e.g. Price et al. [1987]; Price et al. [1986]; Price and Sundermeyer [1999]). Thus the value of eddy viscosity in the mixed layer is much larger than in the pycknocline (e.g D'Asaro and Dairiki [1997]; Weller and Price [1988]; McWilliams et al. [1997]). On this basis one layer models were put forward with a constant eddy viscosity in the mixed layer and zero viscosity below (e.g. Lewis and Belcher [2004]; Elipot and Gille [2009]). At the bottom of the mixed layer a variety of boundary conditions were attempted, a comparison of all the possibilities with observation was carried by Elipot and Gille [2009]. Surprisingly, the analysis of the available data did not show a convincing advantage of employing the vanishing shear stress, the most natural boundary condition at the interface, over two other possibilities: no slip condition or moving the interface to infinity. There might be multiple reasons behind, which we will discuss later. Clearly there is an open question on what is the right model for the Ekman currents in the mixed layer. Here, to capture the effect of the pycnocline on the momentum transfer as a first step we adopt the simplest two layer model: with two vastly different values of the eddy viscosity.

The second outstanding problem of major interest is how the vertical structure of stratification manifests itself in the surface current under variable wind. Under what conditions can we expect discernible manifestations? Could we employ the surface manifestations for remote sensing of the depth of the mixed layer? It is known that during the passage of hurricanes the mixed layer dramatically deepens, could we explain this phenomenon within the paradigm of the Ekman type-model and link it

to the dynamics of surface current? We are not aware of any work addressing these issues. This chapter is aimed to address them within the framework of the Ekman type model.

The key open questions we aim to clarify are as follows:

(i) Under what conditions and with what accuracy the two-layer Ekman model can be well approximated by a one layer Ekman model with appropriate boundary conditions at the bottom of the mixed layer? What are the appropriate boundary conditions?

(ii) What are the specific effects of stratification on the surface Ekman currents caused by variable wind? What characteristics of the Ekman current in the near-surface layer depend on the mixed layer thickness? How sensitive is the near surface Ekman current to the value of viscosity in the stratified layer?

(iii) Under what conditions there are noticeable surface manifestations of the presence of stratification? How do these manifestations depend on the temporal scales under consideration?

(iv) Is it possible to find depth of the mixed layer having only observations of the surface currents? Could it be possible to estimate the strength of the stratification in the pycnocline?

Here, to address the above questions we will model the dynamics of the mixed layer caused by time dependent atmosphere forcing upon momentum transfer to the upper ocean within the framework of the Navier-Stokes equations with depth-dependent eddy viscosity. The model is an extension of the classical one-layer model with a constant eddy viscosity. Here we consider two layers, the upper one is of depth d with a constant eddy viscosity ν_{e1}, it is supposed to model the mixed layer; the second layer is characterised by a different constant eddy viscosity ν_{e2}. We assume the lower layer to be stratified and since stratification suppresses turbulence, the eddy viscosity there is much smaller than in the upper layer, i.e. $\nu_{e1} \gg \nu_{e2}$. To focus on the effects due to the presence of stratification, we adopt the simplest model of the

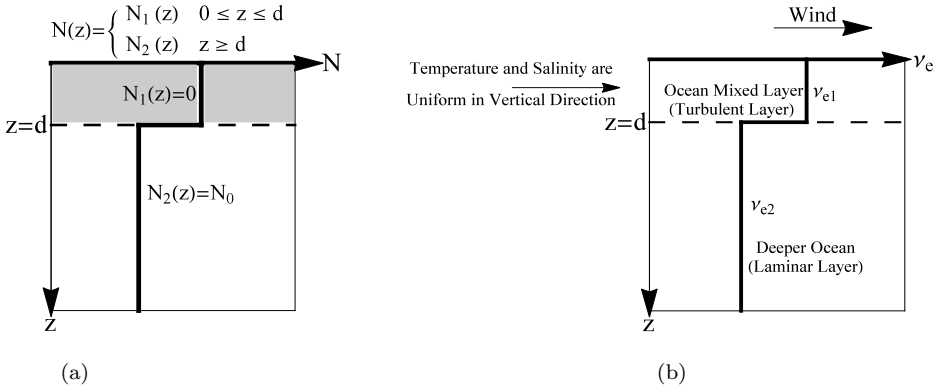

FIGURE 3.1: (a) Stratification profile . (b) Viscosity profile.

mixed layer, assuming the eddy viscosity to be constant both in depth and and time. This could be justified if we understand ν_{e1} as a bulk viscosity and do not consider too rapid variations of wind. Since we are primarily interested in the processes in the mixed layer and the transfer of momentum into the ocean interior is very small, we assume the second layer to be infinitely deep (See the sketch in figure 3.1). We leave aside the issue of relationship between the strength of stratification in the second layer characterised by the Brunt-Väisälä frequency N and eddy viscosity ν_2. One can use any of the widely used empirical relationships, but here we just assume the value of ν_{e2} to be known and will not consider its relationship with N. According to observations, the the eddy viscosity in the mixed layer ranges between $O(10^{-4})$ and $O(10^{-1})$ $\mathrm{m^2 s^{-1}}$ (see table 1.1), while in the pycnocline it is much smaller varying from $O(10^{-6})$ to $O(10^{-4})$ $\mathrm{m^2 s^{-1}}$.

This chapter is organized as follows: §3.2 gives the formulation of the mathematical model (a brief description of the equations and boundary conditions governing drift currents caused by a time-varying wind). §3.3 presents the general solution in terms of Green function, for an arbitrary wind shear stress. §3.4 provides comparisons with one-layer solutions derived by Ekman [1905]; Lewis and Belcher [2004]; Elipot and Gille [2009]. In §3.5 we discuss behaviour of the solution of the system derived in §3.2 for the case of decreasing wind. Finally, a summary and discussion are provided in §3.6.

3.2 The mathematical model

We begin with the Ekman model (1.22). Here, the fluid is assumed to consist of two layers: the upper layer of thickness d is adjacent to the surface, it is supposed to model the mixed layer with high eddy viscosity ν_{e1}. The second layer with eddy viscosity ν_{e2} suppressed by stratification is taken to be infinite, since, as it will be shown below, the horizontal motions caused by varying winds do not penetrate far into the stratified fluid and, therefore, the thickness of the stratified fluid could be assumed infinite without much loss of generality. We recall that for horizontally uniform motions the corresponding exact reduction of the Navier-Stokes equations reads

$$\frac{\partial \boldsymbol{U}_1}{\partial t} + i\,f\,\boldsymbol{U}_1 = \nu_{e1}\frac{\partial^2 \boldsymbol{U}_1}{\partial z^2}, \quad 0 \le z \le d\,, \tag{3.1a}$$

$$\frac{\partial \boldsymbol{U}_2}{\partial t} + i\,f\,\boldsymbol{U}_2 = \nu_{e2}\frac{\partial^2 \boldsymbol{U}_2}{\partial z^2}, \quad d \le z < \infty\,. \tag{3.1b}$$

where $\boldsymbol{U}_1 = u_1 + iv_1$ and $\boldsymbol{U}_2 = u_2 + iv_2$ are the horizontal complex velocities for the surface layer and the lower layer respectively. The motion has to satisfy the surface boundary condition (1.23), at the interface the current and the stress are continuous and the lower boundary condition (1.25) closes the system:

$$\nu_{e1}\frac{\partial \boldsymbol{U}_1(z,t)}{\partial z} = \frac{-\boldsymbol{\tau}(t)}{\rho}\,, \qquad \text{at} \quad z = 0\,, \tag{3.2a}$$

$$\boldsymbol{U}_1(z,t) = \boldsymbol{U}_2(z,t)\,, \qquad \text{at} \quad z = d\,, \tag{3.2b}$$

$$\nu_{e1}\frac{\partial \boldsymbol{U}_1(z,t)}{\partial z} = \nu_{e2}\frac{\partial \boldsymbol{U}_2(z,t)}{\partial z}\,, \qquad \text{at} \quad z = d\,, \tag{3.2c}$$

$$\boldsymbol{U}_2'(z,t) = 0\,, \qquad \text{as} \quad z \to \infty\,. \tag{3.2d}$$

We stress that in the adopted model ν_{e1}, ν_{e2} are both constants. In the next section we derive the exact general solution of the system defined above.

3.3 General solution

The equations of motion (3.1) can be easily solved by applying the Fourier transform with respect to t,

$$\tilde{\boldsymbol{U}}_j(z,\omega) = \int_{-\infty}^{\infty} \boldsymbol{U}_j(z,t) e^{-i\omega t} dt; \quad j = 1,2\,. \tag{3.3}$$

which converts the partial differential equations (3.1) into ordinary equations with respect to z:

$$i(f+\omega)\tilde{\boldsymbol{U}}_1(z,\omega) - \nu_{e1}\frac{d^2\tilde{\boldsymbol{U}}_1(z,\omega)}{dz^2} = 0\,, \tag{3.4}$$

$$i(f+\omega)\tilde{\boldsymbol{U}}_2(z,\omega) - \nu_{e2}\frac{d^2\tilde{\boldsymbol{U}}_2(z,\omega)}{dz^2} = 0\,. \tag{3.5}$$

By using the Fourier transformed boundary conditions:

$$\nu_{e1}\frac{\partial\tilde{\boldsymbol{U}}_1(z,\omega)}{\partial z} = \frac{-\boldsymbol{\tau}(\omega)}{\rho}\,, \qquad \text{at} \quad z = 0\,, \tag{3.6a}$$

$$\tilde{\boldsymbol{U}}_1(z,\omega) = \tilde{\boldsymbol{U}}_2(z,\omega)\,, \qquad \text{at} \quad z = d\,, \tag{3.6b}$$

$$\nu_{e1}\frac{\partial\tilde{\boldsymbol{U}}_1(z,\omega)}{\partial z} = \nu_{e2}\frac{\partial\tilde{\boldsymbol{U}}_2(z,\omega)}{\partial z}\,, \qquad \text{at} \quad z = d\,, \tag{3.6c}$$

$$\tilde{\boldsymbol{U}}_2'(z,\omega) = 0\,, \qquad \text{as} \quad z \to \infty\,, \tag{3.6d}$$

solutions for $\tilde{\boldsymbol{U}}_1(z,\omega)$ and $\tilde{\boldsymbol{U}}_2(z,\omega)$ are found in the form:

$$\tilde{\boldsymbol{U}}_1(z,\omega) = \boldsymbol{\tau}(\omega)\boldsymbol{K}_1(z,\omega)\,, \tag{3.7}$$

$$\tilde{\boldsymbol{U}}_2(z,\omega) = \boldsymbol{\tau}(\omega)\boldsymbol{K}_2(z,\omega)\,. \tag{3.8}$$

Then the general solution of equations (3.1) is given by the inverse Fourier transform:

$$\boldsymbol{U}_j(z,t) = \frac{1}{2\pi}\int_{-\infty}^{\infty} \tilde{\boldsymbol{U}}_j(z,\omega)e^{i\omega t}d\omega; \quad j=1,2. \tag{3.9}$$

The general solution to the equations of motion (3.4, 3.5) can be written in the form

$$\tilde{\boldsymbol{U}}_1(z,\omega) = A\,\exp\left[(1+i)\,z/\delta_1(\omega)\right] + B\,\exp\left[-(1+i)\,z/\delta_1(\omega)\right]\,, \tag{3.10a}$$

$$\tilde{\boldsymbol{U}}_2(z,\omega) = c_1\,\exp\left[(1+i)\,z/\delta_2(\omega)\right] + c_2\,\exp\left[-(1+i)\,z/\delta_2(\omega)\right]\,, \tag{3.10b}$$

where

$$\delta_1(\omega) = \sqrt{\frac{2\nu_{e1}}{f+\omega}} \;\text{ and }\; \delta_2(\omega) = \sqrt{\frac{2\nu_{e2}}{f+\omega}}.$$

By applying the transformed boundary conditions at the surface and at infinity, the general solution can be rewritten as:

$$\tilde{\boldsymbol{U}}_1 = 2B\,\cosh\left[(1+i)\,z/\delta_1(\omega)\right] + \frac{\boldsymbol{\tau}(\omega)\,e^{-i\pi/4}}{\rho\sqrt{\nu_1}\sqrt{f+\omega}}\,\exp\left[-(1+i)\,z/\delta_1(\omega)\right], \tag{3.11}$$

and,

$$\tilde{\boldsymbol{U}}_2(z,\omega) = c_2\,\exp\left[-(1+i)\,z/\delta_2(\omega)\right]\,. \tag{3.12}$$

The unspecified yet arbitrary constants B and c_2 are determined from the boundary conditions at the internal interface:

$$B = \frac{\left(\sqrt{\nu_{e1}}+\sqrt{\nu_{e2}}\right)\,\boldsymbol{\tau}(\omega)\,e^{-i\pi/4}\,\exp\left[(1+i)\,d/\delta_1(\omega)\right]}{2\,\rho\sqrt{\nu_{e1}}\sqrt{f+\omega}\,\left(\sqrt{\nu_{e2}}\,\cosh\left[(1+i)\,d/\delta_1(\omega)\right]+\sqrt{\nu_{e1}}\,\sinh\left[(1+i)\,d/\delta_1(\omega)\right]\right)}\,, \tag{3.13a}$$

$$c_2 = \frac{\boldsymbol{\tau}(\omega)\,e^{-i\pi/4}\,\exp\left[(1+i)\,d/\delta_2(\omega)\right]}{\rho\sqrt{f+\omega}\,\left(\sqrt{\nu_{e2}}\,\cosh\left[(1+i)\,d/\delta_1(\omega)\right]+\sqrt{\nu_{e1}}\,\sinh\left[(1+i)\,d/\delta_1(\omega)\right]\right)}\,. \tag{3.13b}$$

Finally, the general solution in the upper and lower layers is as follows:

$$\boldsymbol{U}_1(z,t) = \frac{1}{2\pi}\int_{-\infty}^{\infty} \tilde{\boldsymbol{U}}_1(z,\omega)\, e^{i\omega t}\, d\omega, \quad \boldsymbol{U}_2(z,t) = \frac{1}{2\pi}\int_{-\infty}^{\infty} \tilde{\boldsymbol{U}}_2(z,\omega)\, e^{i\omega t}\, d\omega, \quad (3.14a)$$

where

$$\tilde{\boldsymbol{U}}_1(z,\omega) = \frac{e^{-i\pi/4}\,\boldsymbol{\tau}(\omega)\,\left(\sqrt{\nu_{e1}}\,\cosh\left[(1+i)\,(d-z)/\delta_1(\omega)\right] + \sqrt{\nu_{e2}}\,\sinh\left[(1+i)\,(d-z)/\delta_1(\omega)\right]\right)}{\rho\,\sqrt{\nu_{e1}}\,\sqrt{f+\omega}\,\left(\sqrt{\nu_{e2}}\,\cosh\left[(1+i)\,d/\delta_1(\omega)\right] + \sqrt{\nu_{e1}}\,\sinh\left[(1+i)\,d/\delta_1(\omega)\right]\right)}, \quad (3.14b)$$

and,

$$\tilde{\boldsymbol{U}}_2(z,\omega) = \frac{e^{-i\pi/4}\,\boldsymbol{\tau}(\omega)\,\exp\left[(1+i)\,(d-z)/\delta_2(\omega)\right]}{\rho\,\sqrt{f+\omega}\,\left(\sqrt{\nu_{e2}}\,\cosh\left[(1+i)\,d/\delta_1(\omega)\right] + \sqrt{\nu_{e1}}\,\sinh\left[(1+i)\,d/\delta_1(\omega)\right]\right)}. \quad (3.15)$$

The Ekman flux $\boldsymbol{S}$, i.e. the flux integrated over entire depth, is

$$\begin{aligned}
\boldsymbol{S} &= \int_0^{\infty} \tilde{\boldsymbol{U}}(z,\omega)dz && (3.16)\\
&= \int_0^{d} \tilde{\boldsymbol{U}}_1(z,\omega)dz + \int_d^{\infty} \tilde{\boldsymbol{U}}_2(z,\omega) && (3.17)\\
&= \frac{i\boldsymbol{\tau}(\omega)}{\rho(f+\omega)}. && (3.18)
\end{aligned}$$

This result serves as a self check aimed to verify that the total flow provided by integration of the obtained general solution is indeed independent of viscosity distribution, and, therefore, it is identical to that given by the classical Ekman model. A stronger validation is provided by the observation that the obtained solution in the limit $\nu_2 \to 0$, tends to the one-layer solution with the boundary condition $\boldsymbol{U}' = 0$ at the bottom of the mixed layer derived by (Elipot and Gille [2009]).

In the next sections we will analyse particular cases and implications of the solution defined above.

3.3.1 The solution limiting behavior in the frequency domain

So far we have not made any explicit assumptions regarding smallness of ν_2 compared to ν_{e1}. Here we consider $\nu_{e2}/\nu_{e1} \ll 1$ and, in particular, examine behaviour of the Ekman response in the limit $\nu_{e2}/\nu_{e1} \to 0$.

General case

The constants B and c_2 (equations 3.13) simplify to:

$$B = \frac{\boldsymbol{\tau}(\omega)\, e^{-i\pi/4}\, \exp\left[(1+i)\, d/\delta_1(\omega)\right]}{2\,\rho\,\sqrt{f+\omega}\,\sqrt{\nu_{e1}}\,\sinh\left[(1+i)\, d/\delta_1(\omega)\right]}\,, \tag{3.19a}$$

$$c_2 = \frac{\boldsymbol{\tau}(\omega)\, e^{-i\pi/4}\, \exp\left[(1+i)\, d/\delta_2(\omega)\right]}{\rho\,\sqrt{f+\omega}\,\sqrt{\nu_{e1}}\,\sinh\left[(1+i)\, d/\delta_1(\omega)\right]}\,, \tag{3.19b}$$

so that, the general solution of the upper and lower layer in the Fourier space is as follows:

$$\tilde{\boldsymbol{U}}_1(z,\omega) = \frac{\boldsymbol{\tau}(\omega)\, e^{-i\pi/4}\, \cosh\left[(1+i)\,(d-z)/\delta_1(\omega)\right]}{\sqrt{\nu_{e1}}\,\sqrt{f+\omega}\,\sinh\left[(1+i)\, d/\delta_1(\omega)\right]}\,. \tag{3.20a}$$

and,

$$\tilde{\boldsymbol{U}}_2(z,\omega) = \frac{\boldsymbol{\tau}(\omega)\, e^{-i\pi/4}\, \exp\left[(1+i)\,(d-z)/\delta_2(\omega)\right]}{\sqrt{\nu_{e1}}\,\sqrt{f+\omega}\,\sinh\left[(1+i)\, d/\delta_1(\omega)\right]}\,. \tag{3.20b}$$

The resulting transfer function in the upper layer is the same as the obtained solution for the one-layer model with velocity shear vanishing at prescribed depth $z = d$ (Elipot and Gille [2009]) (see figure 3.17). Also, the solution in the lower layer reduces to the given form (3.20b). Note that the solution of Elipot and Gille [2009] model under assumption of the total suppression of turbulence in the stratified layer was also derived in an explicit form for the case of a sharp increase of wind by Lewis and Belcher [2004].

Shallow mixed layer $(z, d \ll \delta_1(\omega))$

The solution of the upper layer, $\tilde{\boldsymbol{U}}_1$, with an arbitrary ν_{e1} and ν_{e2} (no assumptions have been made on ν_{e1} and ν_{e2} yet) becomes:

$$\begin{aligned}\tilde{\boldsymbol{U}}_1(z,\omega) =& \frac{\boldsymbol{\tau}(\omega)\, e^{-i\pi/4}\, \left(\sqrt{\nu_{e1}} + \sqrt{\nu_{e2}}(1+i)(d-z)/\delta_1 \right)}{\rho \sqrt{\nu_{e1}}\, \sqrt{f+\omega}\, \left(\sqrt{\nu_{e2}} + \sqrt{\nu_{e1}}\,(1+i)d/\delta_1 \right)} \\ =& \frac{\boldsymbol{\tau}(\omega)\, e^{-i\pi/4}\, \left(\sqrt{\nu_{e1}} + \sqrt{\nu_{e2}/\nu_{e1}}\, e^{i\pi/4}\,(d-z)\, \sqrt{f+\omega} \right)}{\rho \sqrt{\nu_{e1}}\, \sqrt{f+\omega}\, \left(\sqrt{\nu_{e2}} + e^{i\pi/4}\, d\, \sqrt{f+\omega} \right)}\,. \end{aligned} \tag{3.21}$$

For $\nu_{e1} \gg \nu_{e2}$, the previous equation can be rewritten as

$$\begin{aligned}\tilde{\boldsymbol{U}}_1(z,\omega) =& \frac{\boldsymbol{\tau}(\omega)\, e^{-i\pi/4}}{\rho \sqrt{f+\omega}\, \left(\sqrt{\nu_{e2}} + e^{i\pi/4}\, d\, \sqrt{f+\omega} \right)} \\ =& \frac{\boldsymbol{\tau}(\omega)\, e^{-i\pi/2}}{\rho\,(f+\omega)\, d} \left(1 - \frac{e^{-i\pi/4}\, \sqrt{\nu_{e2}}}{d\, \sqrt{f+\omega}} \right). \end{aligned} \tag{3.22}$$

and, for shallow mixed layer, $(d/\delta_1 \to 0)$ and $\nu_{e1} \gg \nu_{e2}$, we recover the classical Ekman solution:

$$B = \frac{\boldsymbol{\tau}(\omega) e^{-i\pi/4}}{2\rho\sqrt{\nu_{e2}(f+\omega)}}\,. \tag{3.23}$$

It follows that $\tilde{U}_2 = 2B$. and,

$$c_1 = \frac{\boldsymbol{\tau}(\omega) e^{-i\pi/4}}{\rho\sqrt{\nu_{e2}(f+\omega)}} = 2B\,, \tag{3.24}$$

then,

$$\tilde{\boldsymbol{U}}_2 = \frac{\boldsymbol{\tau}(\omega) e^{-i\pi/4}}{\rho\sqrt{\nu_{e2}(f+\omega)}} \exp\left[-(1+i) z \sqrt{\frac{f+\omega}{2\nu_{e2}}} \right], \tag{3.25}$$

which coincides with the classical Ekman solution in Fourier space and $\tilde{U}_2 \mid_{z=0} = 2B$. For large time scale $\omega \ll f$ the solution can be written as:

$$\tilde{\boldsymbol{U}}_1 = \frac{\boldsymbol{\tau}(\omega) e^{-i\pi/4}}{\rho\sqrt{\nu_{e2} f}}\,, \tag{3.26}$$

$$\tilde{\boldsymbol{U}}_2 = \frac{\boldsymbol{\tau}(\omega) e^{-i\pi/4}}{\rho\sqrt{\nu_{e2} f}} \exp\left[-(1+i)z\sqrt{\frac{f}{2\nu_{e2}}}\right]. \tag{3.27}$$

Deep mixed layer ($d \gg \delta_1$)

The equation (3.13a) specifying constant B reduces to:

$$B = \frac{\boldsymbol{\tau}(\omega) e^{-i\pi/4}}{\rho\sqrt{\nu_{e1}(f+\omega)}}, \tag{3.28}$$

so that the transfer function of the upper layer becomes:

$$\tilde{\boldsymbol{U}}_1(z,\omega) = \frac{\boldsymbol{\tau}(\omega) e^{-i\pi/4}}{\rho\sqrt{\nu_{e1}(f+\omega)}} \exp\left[-(1+i)z\sqrt{\frac{f+\omega}{2\nu_{e1}}}\right], \tag{3.29}$$

which coincides with the classical Ekman model. For small time, the frequency, ω, is large ($\omega \gg f$) and in this regime the effect of rotation is negligible so that the flow is unidirectional.

$$\tilde{\boldsymbol{U}}_2(z,\omega) = \frac{\boldsymbol{\tau}(\omega) e^{-i\pi/4}}{\rho\sqrt{\nu_{e1}(f+\omega)}} \frac{\exp\left[(1+i)(d-z)/\delta_2(\omega)\right]}{\exp\left[(1+i)d/\delta_1(\omega)\right]}\,. \tag{3.30}$$

3.3.2 Steady-state solution

Under a constant wind ($\boldsymbol{\tau} = \boldsymbol{\tau}_0$), the general solution to the problem (figure 3.2) simplifies to become

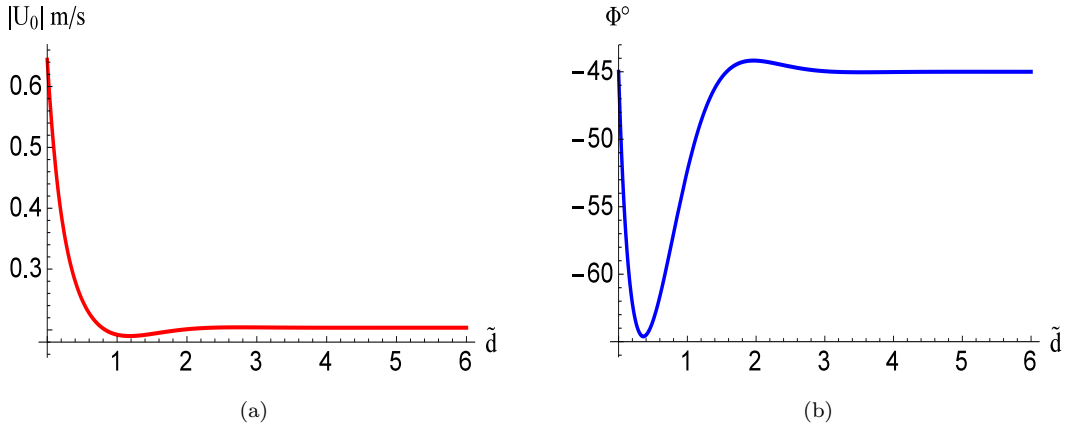

FIGURE 3.2: Dependence of steady Ekman current on mixed layer non-dimensional depth d/δ_1: (a) Surface current speed. (b) Deflection of the direction of current at the surface with respect to wind. The sample parameters are $\nu_{e1} = 7 \times 10^{-3} m^2 s^{-1}$ (which corresponds to 10m s^{-1} wind) , $\nu_{e2} = 7 \times 10^{-4} \mathrm{m^2 s^{-1}}$, $f = 10^{-4} \mathrm{s^{-1}}$, $\rho = 1027 \mathrm{kg\ m^{-3}}$ and $\tau_0 = 0.175 \mathrm{N\ m^{-2}}$.

$$\boldsymbol{U}_1(z) = \frac{\boldsymbol{\tau}_0\, e^{-i\pi/4}\ \left(\sqrt{\nu_{e1}}\,\cosh\left[(1+i)\,(d-z)/\delta_1(0)\right] + \sqrt{\nu_{e2}}\,\sinh\left[(1+i)\,(d-z)/\delta_1(0)\right]\right)}{\rho\,\sqrt{\nu_{e1} f}\ \left(\sqrt{\nu_{e2}}\,\cosh\left[(1+i)\,d/\delta_1(0)\right] + \sqrt{\nu_{e1}}\,\sinh\left[(1+i)\,d/\delta_1(0)\right]\right)}\,, \tag{3.31a}$$

$$\boldsymbol{U}_2(z) = \frac{\boldsymbol{\tau}_0\, e^{-i\pi/4}\ \exp\left[(1+i)\,(d-z)/\delta_2(0)\right]}{\rho\,\sqrt{f}\ \left(\sqrt{\nu_{e2}}\,\cosh\left[(1+i)\,d/\delta_1(0)\right] + \sqrt{\nu_{e1}}\,\sinh\left[(1+i)\,d/\delta_1(0)\right]\right)}\,. \tag{3.31b}$$

When $z, d \ll \delta_1(0)$, equation (3.22) becomes:

$$\boldsymbol{U}_1 = \frac{\boldsymbol{\tau}_0\, e^{-i\pi/2}}{\rho\, f\, d}\left(1 - \frac{e^{-i\pi/4}\sqrt{\nu_{e2}}}{d\sqrt{f}}\right)\,, \tag{3.32}$$

and,

$$\Phi = tan^{-1}\left(d\sqrt{\frac{2f}{\nu_{e2}}} - 1\right)\,. \tag{3.33}$$

Figure (3.2) shows sensitivity of the Ekman current on the surface to the non-dimensional depth of the mixed layer d/δ_1. Since δ_1 scales as u_*^2 or U_{10}^2, the surface currents starts to feel the stratification under stronger winds. Typical samples of

velocity components (u, v) and their second derivative are shown in figure (3.3). The change of sign of the second derivative suggests inflection instabilities and mixing.

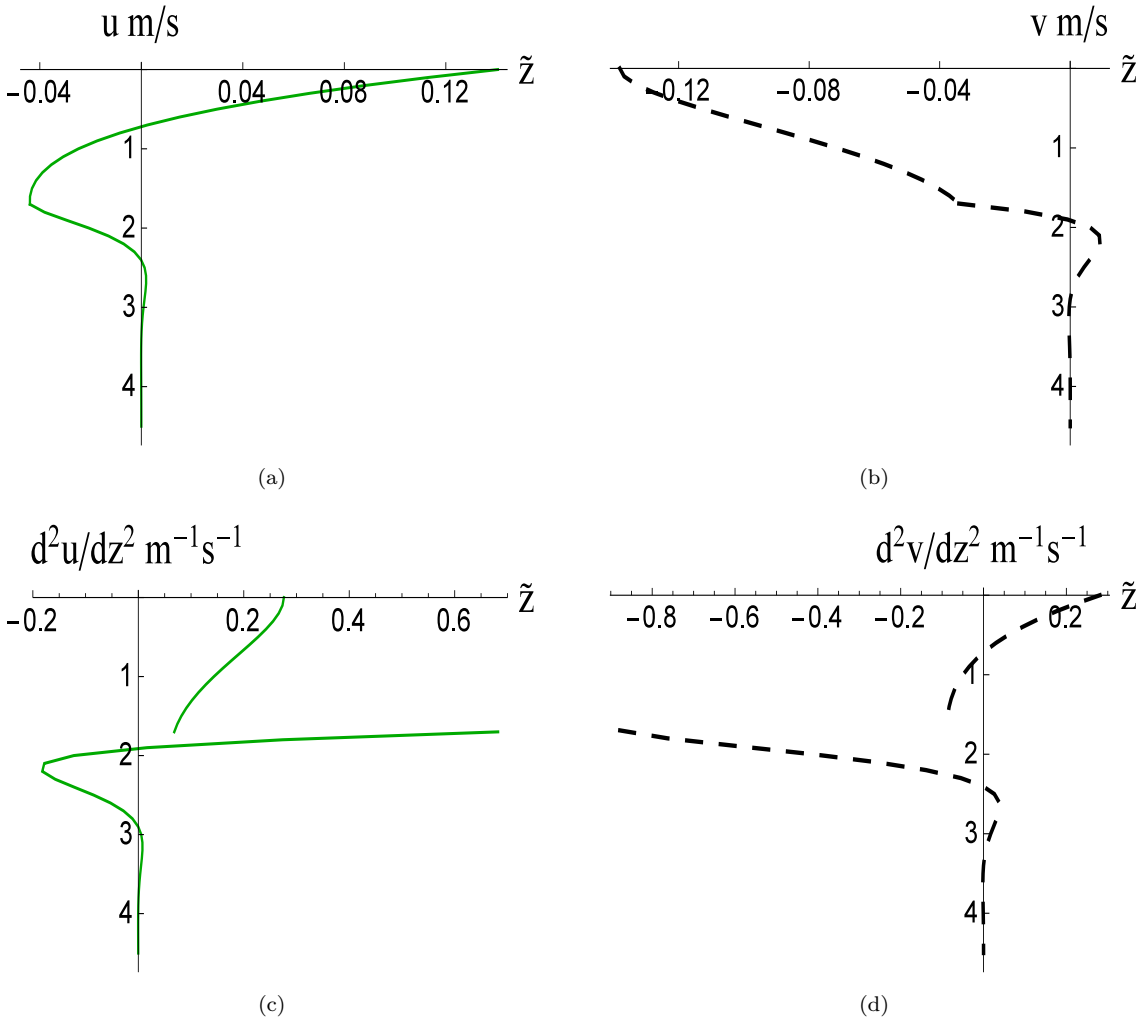

FIGURE 3.3: (a,b) The velocity components in the direction of x and y, respectively. (c,d) The second derivative of x and y velocity components. parameters values are $\nu_{e1} = 7 \times 10^{-3}$, $\nu_{e2} = 7 \times 10^{-4}$, $\tilde{d} = 1.7$, $f = 10^{-4}\,\mathrm{s}^{-1}$, $\rho = 1027\,\mathrm{kg\ m}^{-3}$ and $\tau_0 = 0.175\,\mathrm{N\ m}^{-2}$.

3.3.3 Comparison between the two-layer model and the other existing models

In this section we present in figures (3.4, 3.5, 3.6) a comparison between the results of two-layer model and the other existing models: (a) Elipot and Gille [2009] model which assumed unfinitely strong stratification ($\nu_{e2} = 0$), (b) the classical Ekman model where there is no stratification. Note that d is given as a normalized depth and it is different for different values of ν_{e1}.

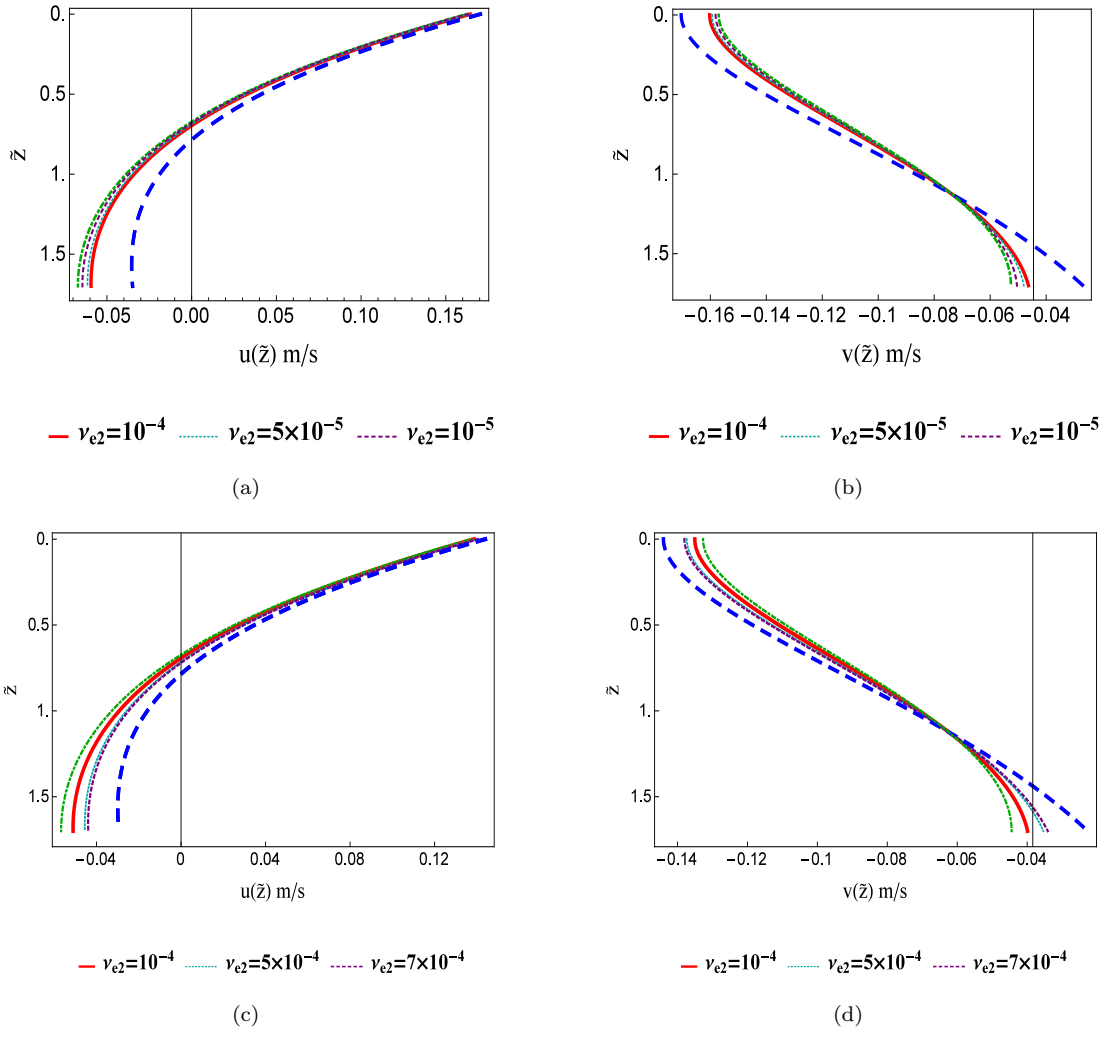

FIGURE 3.4: Sensitivity of vertical profiles of velocity components u, v to strength of stratification characterised by ν_{e2}. Classical Ekman model (blue dashed line), Elipot and Gille model (green dot-dashed line). (a,b): $\nu_{e1} = 5 \times 10^{-3}$. (c,d): $\nu_{e1} = 7 \times 10^{-3}$. $\tilde{d} = 1.7$, $f = 10^{-4}\,\mathrm{s}^{-1}$, $\rho = 1027\,\mathrm{kg\ m}^{-3}$ and $\tau_0 = 0.175\,\mathrm{N\ m}^{-2}$.

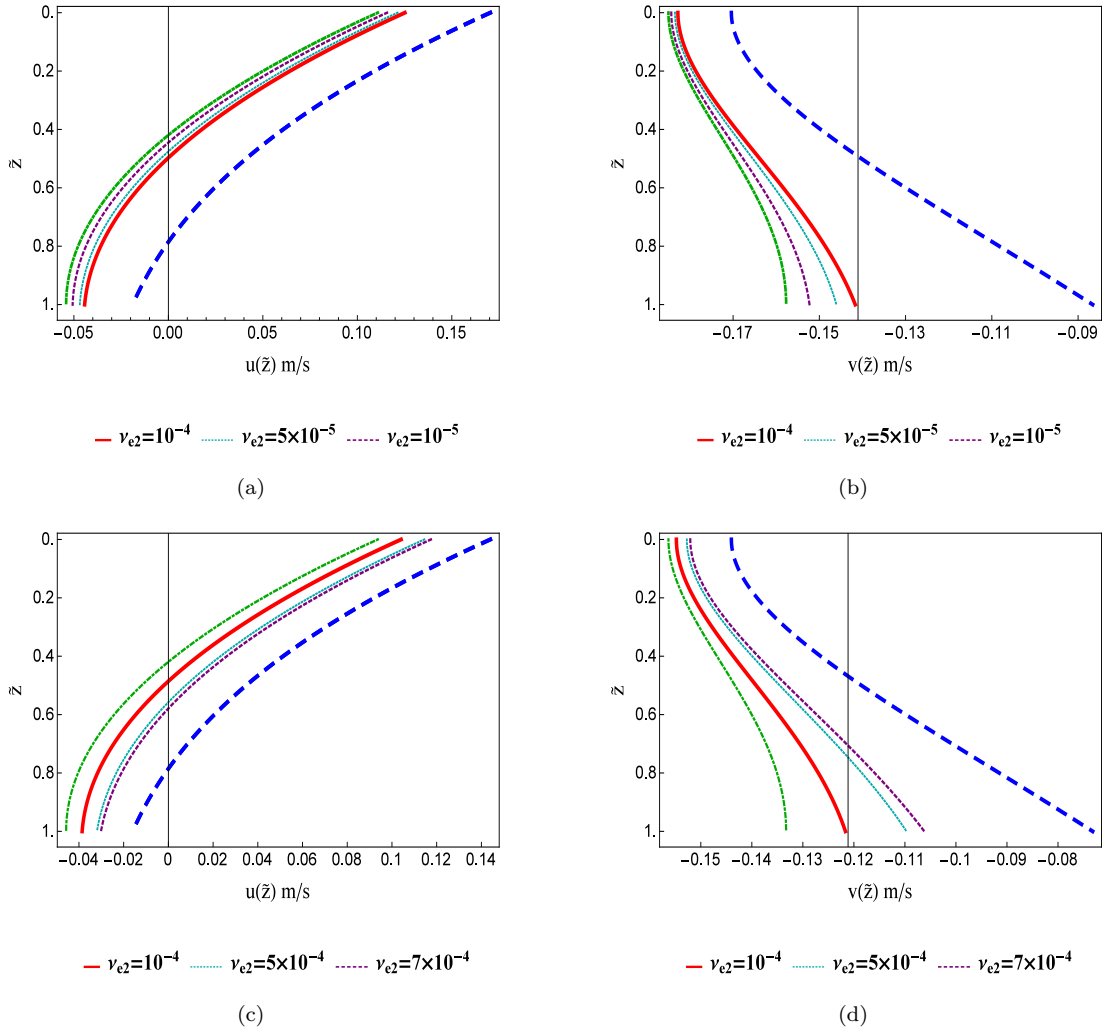

FIGURE 3.5: Sensitivity of vertical profiles of velocity components u, v to strength of stratification characterised by ν_{e2}. Classical Ekman model (blue dashed line), Elipot and Gille model (green dot-dashed line). (a,b): $\nu_{e1} = 5 \times 10^{-3}$. (c,d): $\nu_{e1} = 7 \times 10^{-3}$. $\tilde{d} = 1$, $f = 10^{-4}\,\mathrm{s}^{-1}$, $\rho = 1027\,\mathrm{kg\ m}^{-3}$ and $\tau_0 = 0.175\,\mathrm{N\ m}^{-2}$.

As expected the results of the two-layer model are in between the Elipot and Gille [2009] model corresponding to infinite stratification in the second layer and Ekman [1905] model which corresponds to zero stratification, and overall the dependence on ν_{e2} is not strong (see figures 3.4, 3.5).

Comparison of two-layer model with that of Elipot and Gille's model

In this part, we find the difference ($\boldsymbol{\Delta}$) between the Elipot and Gille solution and classical Ekman solution at the surface which is normalized by the Ekman solution.

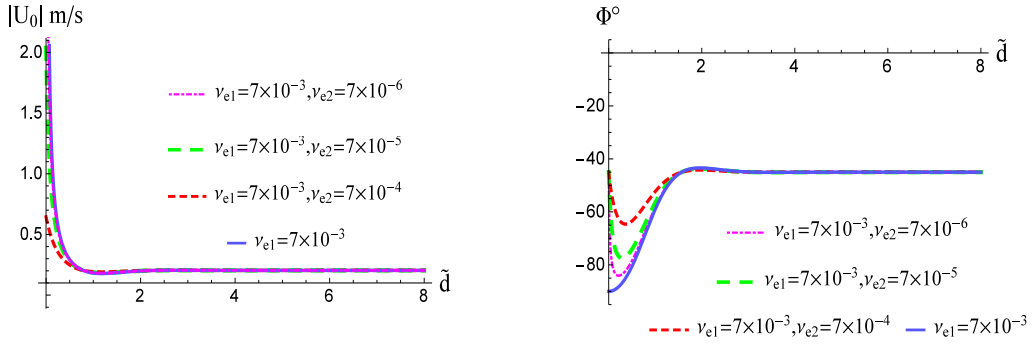

(a) (b)

FIGURE 3.6: Sensitivity of surface current dependence on the thickness of the mixed layer and the stratification. Comparison between the steady-state solutions for Elipot and Gille's model (solid line) and two-layer model(dashed and dot-dashed lines): (a),(b) Dependence of the Ekman current speed and direction at the surface on nondimensional mixed layer depth for the two-layer model with a sample set of parameters : $f = 10^{-4}\,\mathrm{s}^{-1}$, $\rho = 1027\,\mathrm{kg\ m}^{-3}$ and $\tau_0 = 0.175\,\mathrm{N\ m}^{-2}$.

First we recall these solutions:

Classical Ekman solution ($\boldsymbol{U}_{CE}$):

$$\boldsymbol{U}_{CE}(z) = \frac{\boldsymbol{\tau}_0 e^{-i\pi/4}}{\rho\sqrt{\nu_{e1} f}} \exp[-(1+i)\tilde{z}]\,. \tag{3.34}$$

Elipot and Gille [2009] solution ($\boldsymbol{U}_{EG}$):

$$\boldsymbol{U}_{EG}(z) = \frac{\boldsymbol{\tau}_0 e^{-i\pi/4}}{\rho\sqrt{\nu_{e1} f}} \frac{\cosh[(1+i)(\tilde{d}-\tilde{z})]}{\sinh[(1+i)\tilde{d}]}\,, \tag{3.35}$$

where

$$\tilde{z} = z/\delta_1(0) \quad \text{and} \quad \tilde{d} = d/\delta_1(0)\,.$$

The solution (3.35) at the surface, $z = 0$:

$$\begin{aligned}\boldsymbol{U}_{EG}(0) =& \frac{\boldsymbol{\tau}_0\, e^{-i\pi/4}}{\rho\sqrt{f\nu_{e1}}} \coth[(1+i)\tilde{d}] \\ =& \frac{\boldsymbol{\tau}_0\, e^{-i\pi/4}}{\rho\sqrt{f\nu_{e1}}} \left(\frac{i\sin(2\tilde{d}) - \sinh(2\tilde{d})}{\cos(2\tilde{d}) - \cosh(2\tilde{d})}\right), \end{aligned} \tag{3.36}$$

where the surface current speed is given by

$$|\boldsymbol{U}_{EG}(\tilde{d})| = \frac{\boldsymbol{\tau}_0}{\rho\sqrt{f\nu_{e1}}} \left(\frac{\cosh(2\tilde{d}) + \cos(2\tilde{d})}{\cosh(2\tilde{d}) - \cos(2\tilde{d})}\right)^{1/2}, \tag{3.37}$$

and the angle of its deflection from wind direction is

$$\tan\left(\Phi_{EG}(\tilde{d})\right) = \frac{\sin(2\tilde{d}) + \sinh(2\tilde{d})}{\sin(2\tilde{d}) - \sinh(2\tilde{d})}\,. \tag{3.38}$$

The difference between the angle given by equation (3.38) and the angle at the surface for the classical Ekman is shown in figure (3.8). To compare Elipot and Gille [2009] model with the classical Ekman model we introduce a relative discrepancy $\boldsymbol{\Delta}_{\{EG-CE\}}$:

$$\begin{aligned}\boldsymbol{\Delta}_{\{EG-CE\}} =& \frac{|\boldsymbol{U}_{EG}(0) - \boldsymbol{U}_{CE}(0)|}{|\boldsymbol{U}_{CE}(0)|} = \left|\frac{2e^{-\zeta}}{e^{\zeta} - e^{-\zeta}}\right|; \qquad \zeta = (1+i)\tilde{d}\,, \\ \approx& \left|2e^{-2\zeta}(1 + e^{-2\zeta})\right| = \delta_{\{EG-CE\}}\,. \end{aligned} \tag{3.39}$$

By taking the leading order term only, one obtains

$$\begin{aligned} |e^{-2\zeta}| = \frac{\delta_{\{EG-CE\}}}{2} \quad &\Longrightarrow e^{-2\tilde{d}} = \frac{\delta_{\{EG-CE\}}}{2} \\ &\Longrightarrow \tilde{d} = \frac{1}{2}\ln\left(\frac{2}{\delta_{\{EG-CE\}}}\right). \end{aligned} \tag{3.40}$$

If we choose the threshold value of $\delta_{\{EG-CE\}}$ to be 0.1, the equation (3.40) shows that the surface current will be sensitive to stratification when $\tilde{d} \approx 1.5$, and since $\tilde{d}$ depends on ν_1, which scales as u_*^2 or U_{10}^2, the current at the surface feels stratification at different depths depending on wind strength.

TABLE 3.1: Estimated eddy viscosity coefficients and the depth scale of the Ekman layer where $\delta_1 = \sqrt{2\nu_{e1}/f}$, $\nu_{e1} = cu_\star^2/f$, $c = 0.03$, $u_\star = \sqrt{\tau/\rho_w}$, $\tau = \rho_a U_{10}^2 C_D$, $\rho_a = 1.25\,\mathrm{kg\ m^{-3}}$, $C_D = 1.4 \times 10^{-3}$, $\rho_w = 1027\,\mathrm{kg\ m^{-3}}$, and $f = 10^{-4}\,\mathrm{s^{-1}}$ (Coleman et al. [1990]).

U_{10} (m s^{-1})	τ (N m^{-2})	$u_\star$ (m s^{-1})	ν_e m^{2}s^{-1}	δ_1 (m)
5	0.044	0.007	0.01	16
10	0.175	0.013	0.05	30
30	1.575	0.039	0.5	100
50	4.375	0.065	1.3	160

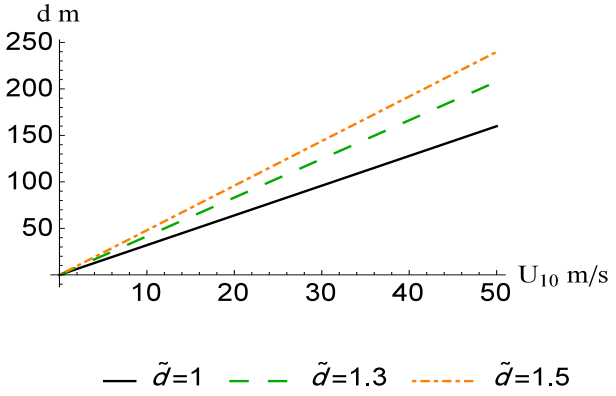

FIGURE 3.7: The depth of the mixed layer for a particular values of $\tilde{d} = d/\delta_1(0)$ where $\delta_1(0)$ scales as u_*^2 or U_{10}^2.

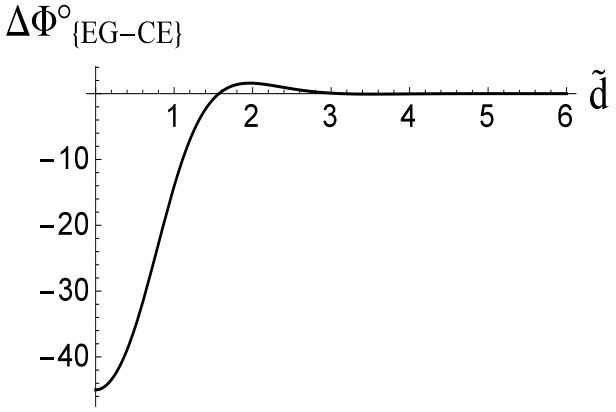

FIGURE 3.8: The predicted difference in angle between the Elipot and Gille solution and the classical Ekman solution for a steady wind ($\Delta\Phi_{\{EG-CE\}} = \Phi_{EG}+\pi/4$). Φ_{EG} is given by eq.(3.38).

In the previous part we analyzed sensitivity of steady Ekman flows to the presence of stratification, the strength of stratification in the pycnocline and the depth of the mixed layer, and for more general case when the wind is varying at different frequencies the sensitivity is also different i.e. the sensitivity depends on frequency

so that we analyzed the sensitivity for time-dependent Ekman flows by comparing two limiting cases: (a) the case of zero stratification in the second layer (Elipot and Gille [2009]), and (b) the case of no stratification (Ekman [1905]). By choosing different threshold $\delta_{\{EG-CE\}}$ which characterises the discrepancy between the models, we can estimate the depth of the mixed layer where it would feel the presence of stratification. We provide a table (3.2) which illustrates how the depth for various $\delta_{\{EG-CE\}}$ depends on frequencies.

$$\begin{aligned} d_{\delta_{\{EG-CE\}}} &\approx \frac{-1}{\sqrt{2}} \left(\left(\frac{f+\omega}{\nu_{e1}} \right)^2 \right)^{-1/4} \ln \left(\frac{\delta_{\{EG-CE\}}}{2} \right) \\ &= \frac{-1}{\sqrt{2}} \left(\left| \frac{f+\omega}{\nu_{e1}} \right| \right)^{-1/2} \ln \left(\frac{\delta_{\{EG-CE\}}}{2} \right) . \end{aligned} \tag{3.41}$$

TABLE 3.2: Depth of the mixed layer for different frequencies.

ω rad s^{-1}	ν_e m^{2}s^{-1}	$d_{0.1}$ m	$d_{0.2}$ m	$d_{0.3}$ m	$d_{0.5}$ m
$2\pi/1$hr	2.4×10^{-3}	2.4	1.9	1.5	1.1
	5×10^{-3}	3.5	2.7	2.2	1.6
	7×10^{-3}	4.1	3.2	2.6	1.9
	10^{-2}	4.9	3.8	3.1	2.3
	10^{-1}	15.6	12	10	7.2
	1	49.3	37.9	31.2	22.8
$2\pi/10$hr	2.4×10^{-3}	6.2	4.8	4	3
	5×10^{-3}	9	6.9	5.7	4.2
	7×10^{-3}	10.7	8.2	6.8	4.9
	10^{-2}	12.8	9.8	8	5.9
	10^{-1}	40.4	31	25.6	18.7
	1	127.8	98.3	81	59.2
$\omega \ll f$	2.4×10^{-3}	10.4	8	6.6	4.8
	5×10^{-3}	15	11.5	9.5	6.9
	7×10^{-3}	17.7	13.6	11.2	8.2
	10^{-2}	21.2	16.3	13.4	9.8
	10^{-1}	67	51.5	42.4	31
	1	211.8	162.8	134.1	98

Comparison of the classical Ekman and two-layer solutions

The difference between the classical Ekman and two-layer ($\boldsymbol{U}_{TL}$) solutions is found similarly, it reads,

$$\begin{aligned}
\boldsymbol{U}_{TL}(\tilde{z}) =& \frac{\boldsymbol{\tau} e^{-i\pi/4}}{\rho\sqrt{\nu_{e1} f}} \frac{\sqrt{\nu_{e1}}\cosh[(1+i)(\tilde{d}-\tilde{z})] + \sqrt{\nu_{e2}}\sinh[(1+i)(\tilde{d}-\tilde{z})]}{\sqrt{\nu_{e2}}\cosh[(1+i)\tilde{d}] + \sqrt{\nu_{e1}}\sinh[(1+i)\tilde{d}]} \\
=& \frac{\boldsymbol{\tau}_0 e^{-i\pi/4}}{\rho\sqrt{\nu_{e1} f}} \frac{\cosh[(1+i)(\tilde{d}-\tilde{z})] + \sqrt{\nu_{e2}/\nu_{e1}}\sinh[(1+i)(\tilde{d}-\tilde{z})]}{\sinh[(1+i)\tilde{d}] + \sqrt{\nu_{e2}/\nu_{e1}}\cosh[(1+i)\tilde{d}]} \\
=& \frac{\boldsymbol{\tau}_0 e^{-i\pi/4}}{\rho\sqrt{\nu_{e1} f}} \frac{\cosh[(1+i)(\tilde{d}-\tilde{z})]\left(1+\sqrt{\eta}\tanh[(1+i)(\tilde{d}-\tilde{z})]\right)}{\sinh[(1+i)\tilde{d}]\left(1+\sqrt{\eta}\coth[(1+i)\tilde{d}]\right)} \\
\approx& \frac{\boldsymbol{\tau}_0 e^{-i\pi/4}}{\rho\sqrt{\nu_{e1} f}} \frac{\cosh[(1+i)(\tilde{d}-\tilde{z})]}{\sinh[(1+i)\tilde{d}]} \left(1+\sqrt{\eta}\tanh[(1+i)(\tilde{d}-\tilde{z})]\right) \times \\
& \left(1-\sqrt{\eta}\coth[(1+i)\tilde{d}]\right) \\
\approx& \boldsymbol{U}_{EG}\left(1+\sqrt{\eta}\tanh[(1+i)(\tilde{d}-\tilde{z})]\right)\left(1-\sqrt{\eta}\coth[(1+i)\tilde{d}]\right), \qquad (3.42)
\end{aligned}$$

where $\eta = \nu_{e2}/\nu_{e1}$.

The angle between the surface current and wind direction is given by:

$$\begin{aligned}
\tan(\Phi_{TL}) =& \frac{(\nu_{e1}-\nu_{e2})\sin(2\tilde{d}) + (\nu_{e1}+\nu_{e2})\sinh(2\tilde{d}) + 2\sqrt{\nu_{e1}\,\nu_{e2}}\cosh(2\tilde{d})}{(\nu_{e1}-\nu_{e2})\sin(2\tilde{d}) - (\nu_{e1}+\nu_{e2})\sinh(2\tilde{d}) - 2\sqrt{\nu_{e1}\,\nu_{e2}}\cosh(2\tilde{d})} \\
=& \frac{(1-\nu_{e2}/\nu_{e1})\sin(2\tilde{d}) + (1+\nu_{e2}/\nu_{e1})\sinh(2\tilde{d}) + 2\sqrt{\nu_{e2}/\nu_{e1}}\cosh(2\tilde{d})}{(1-\nu_{e2}/\nu_{e1})\sin(2\tilde{d}) - (1+\nu_{e2}/\nu_{e1})\sinh(2\tilde{d}) - 2\sqrt{\nu_{e2}/\nu_{e1}}\cosh(2\tilde{d})}. \qquad (3.43)
\end{aligned}$$

For $\nu_{e1} \gg \nu_{e2}$:

$$\begin{aligned}
\tan(\Phi_{TL}) =& \frac{\sin(2\tilde{d}) + \sinh(2\tilde{d}) + 2\sqrt{\nu_{e2}/\nu_{e1}}\cosh(2\tilde{d})}{\sin(2\tilde{d}) - \sinh(2\tilde{d}) - 2\sqrt{\nu_{e2}/\nu_{e1}}\cosh(2\tilde{d})} \\
=& \frac{(\sin(2\tilde{d}) + \sinh(2\tilde{d}))/\cosh(2\tilde{d}) + 2\sqrt{\nu_{e2}/\nu_{e1}}}{(\sin(2\tilde{d}) - \sinh(2\tilde{d}))/\cosh(2\tilde{d}) - 2\sqrt{\nu_{e2}/\nu_{e1}}} \\
=& \frac{a(1 + 2\sqrt{\eta}/a)}{b(1 - 2\sqrt{\eta}/b)} \\
\approx& \frac{a}{b}(1 + 2\sqrt{\eta}/a)(1 - 2\sqrt{\eta}/b) \\
\approx& \tan(\Phi_{EG})\,(1 + 2\sqrt{\eta}/a))\,(1 - 2\sqrt{\eta}/b)\ , \qquad (3.44)
\end{aligned}$$

where

$$a = (\sin(2\tilde{d}) + \sinh(2\tilde{d}))/\cosh(2\tilde{d}) \quad \text{and} \quad b = (\sin(2\tilde{d}) - \sinh(2\tilde{d}))/\cosh(2\tilde{d})\,.$$

Figure (3.9) shows the angle between the surface current of two-layer and classical Ekman models. The following expression gives the difference between the classical Ekman and two-layer model steady solutions

$$\boldsymbol{\Delta}_{\{TL-CE\}} = \boldsymbol{U}_{TL}(0) - \boldsymbol{U}_{CE}(0) = c\,(1-i)\left[\frac{\sqrt{\nu_{e1}}\,(e^{\zeta} + e^{\zeta - \zeta}) + \sqrt{\nu_{e2}}\,(e^{\zeta} - e^{-\zeta})}{\sqrt{\nu_{e2}}\,(e^{\zeta} + e^{-\zeta}) + \sqrt{\nu_{e1}}\,(e^{\zeta} - e^{-\zeta})} - 1\right]; \qquad (3.45)$$

$$c = \frac{\boldsymbol{\tau}_0}{\rho\sqrt{2\nu_{e1}f}}, \quad \zeta = (1+i)\tilde{d},$$

$$\begin{aligned}
\boldsymbol{\Delta}_{\{TL-CE\}} =& c\,(1-i)\,\frac{2(\sqrt{\nu_{e1}} - \sqrt{\nu_{e2}})\,e^{-2\zeta}}{(\sqrt{\nu_{e1}} + \sqrt{\nu_{e2}})\,\left[1 + \frac{\sqrt{\nu_{e2}} - \sqrt{\nu_{e1}}}{\sqrt{\nu_{e2}} + \sqrt{\nu_{e1}}}\,e^{-2\zeta}\right]} \\
\approx& 2\,c_1\,\frac{(\sqrt{\nu_{e1}} - \sqrt{\nu_{e2}})\,e^{-2\zeta}}{(\sqrt{\nu_{e1}} + \sqrt{\nu_{e2}})}\,\left(1 + \frac{\sqrt{\nu_{e1}} - \sqrt{\nu_{e2}}}{\sqrt{\nu_{e1}} + \sqrt{\nu_{e2}}}\,e^{-2\zeta}\right) \\
\approx& 2\,c_1\,\left(1 - 2\sqrt{\frac{\nu_{e2}}{\nu_{e1}}}\right)\,e^{-2\zeta}\,\left(1 + \left(1 - 2\sqrt{\frac{\nu_{e2}}{\nu_{e1}}}\right)\,e^{-2\zeta}\right). \qquad (3.46)
\end{aligned}$$

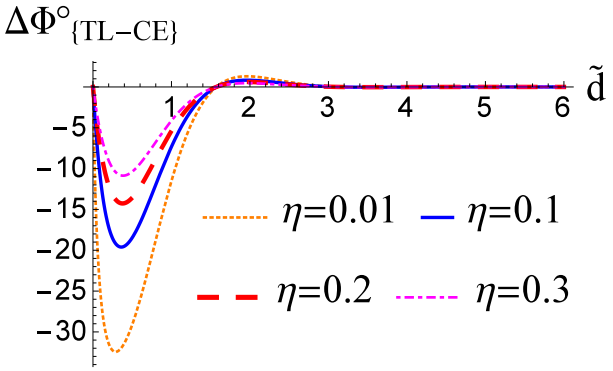

FIGURE 3.9: The predicted difference in angle between the two-layer model and the classical Ekman model ($\Delta\Phi_{\{TL-CE\}} = \Phi_{TL} + 45°$) for the steady state solution at the surface for the following set of parameters: $\eta = 0.01,\ 0.1,\ 0.2,\ 0.3$ ($\eta = \nu_{e2}/\nu_{e1}$). Φ_{TL} is given by eq.(3.43).

A relative difference ($\boldsymbol{\Delta}_1$) of two-layer model and the classical model is given by

$$\boldsymbol{\Delta}_{1\{TL-CE\}} = \frac{|\boldsymbol{\Delta}_{\{TL-CE\}}|}{|\boldsymbol{U}_{CE}(0)|} \approx \left| 2\left(1 - 2\sqrt{\frac{\nu_{e2}}{\nu_{e1}}}\right) e^{-2\zeta} \left(1 + \left(1 - 2\sqrt{\frac{\nu_{e2}}{\nu_{e1}}}\right) e^{-2\zeta}\right) \right|$$
$$= \delta_{\{TL-CE\}}\,. \tag{3.47}$$

By taking the leading order term only we obtain

$$|e^{-2\zeta}| = \frac{\delta_{\{TL-CE\}}}{2c_2} \quad \Longrightarrow e^{-2\tilde{d}} = \frac{\delta_{\{TL-CE\}}}{2c_2} \quad \Longrightarrow \tilde{d} = \frac{1}{2}\ln\left(\frac{2c_2}{\delta_{\{TL-CE\}}}\right). \tag{3.48}$$

where $c_2 = 1 - 2\sqrt{\nu_{e2}/\nu_{e1}}$. Thus, for the time-dependent Ekman flows, we derived an estimate of the mixed layer depth for which the normalised discrepancy between predictions of the two-layer model and the classical Ekman model exceeds a chosen threshold value $\delta_{\{TL-CE\}}$ by comparing two limiting cases: (a) the case of stratified second layer (two-layer model), and (b) the case of no stratification (Ekman [1905]).

$$d_{\{TL-CE\}} \approx \frac{-1}{\sqrt{2}} \left(\left(\frac{f+\omega}{\nu_{e1}}\right)^2\right)^{-1/4} \ln\left(\frac{\delta_{\{TL-CE\}}}{2\,c_2}\right)$$
$$= \frac{-1}{\sqrt{2}} \left(\left|\frac{f+\omega}{\nu_{e1}}\right|\right)^{-1/2} \ln\left(\frac{\delta_{\{TL-CE\}}}{2\,c_2}\right). \tag{3.49}$$

and, the difference in predicted velocity of the surface between two-layer and Elipot and Gille solutions is as follows

$$\begin{aligned}\boldsymbol{\Delta}_{\{TL-EG\}} =&\boldsymbol{U}_{TL}(0)-\boldsymbol{U}_{EG}(0)\\ =&c\,(1-i)\left[\frac{\sqrt{\nu_{e1}}\,(e^{\zeta}+e^{-\zeta})+\sqrt{\nu_{e2}}\,(e^{\zeta}-e^{-\zeta})}{\sqrt{\nu_{e2}}\,(e^{\zeta}+e^{-\zeta})+\sqrt{\nu_{e1}}\,(e^{\zeta}-e^{-\zeta})}-\frac{(e^{\zeta}+e^{-\zeta})}{(e^{\zeta}-e^{-\zeta})}\right]\\ =&c\,(1-i)\,\frac{\sqrt{\nu_{e2}}\,(\tanh\zeta-\coth\zeta)}{\sqrt{\nu_{e2}}+\sqrt{\nu_{e1}}\,\tanh\zeta}\\ =&c\,(1-i)\,\frac{-4\sqrt{\nu_{e2}}}{(e^{2\zeta}-e^{-2\zeta})\,(\sqrt{\nu_{e2}}+\sqrt{\nu_{e1}}\,\tanh\zeta)}\,,\end{aligned}\tag{3.50}$$

where

$$c=\frac{\boldsymbol{\tau}_0}{\rho\sqrt{2\nu_{e1}f}},\quad \zeta=(1+i)\tilde{d}\,.$$

For $\nu_{e1}\gg\nu_{e2}$ and $e^{-2\zeta}\ll 1$:

$$\boldsymbol{\Delta}_{\{TL-EG\}}\approx -4\,c\,e^{-i\pi/4}\sqrt{\frac{\nu_{e2}}{\nu_{e1}}}\,e^{-2\zeta}\,\coth(\xi)\,.\tag{3.51}$$

The second order approximation:

$$\begin{aligned}\boldsymbol{\Delta}_{\{TL-EG\}} =&c\,(1-i)\,\frac{-4\sqrt{\nu_{e2}}}{(e^{2\zeta}-e^{-2\zeta})\,(\sqrt{\nu_{e2}}+\sqrt{\nu_{e1}}\,\tanh\zeta)}\\ \approx&c\,(1-i)\,\frac{-4\sqrt{\nu_{e2}/\nu_{e1}}}{(e^{2\zeta}-e^{-2\zeta})\tanh\zeta}\\ \approx&c\,(1-i)\,\frac{-4\sqrt{\nu_{e2}/\nu_{e1}}\,\coth\zeta}{e^{2\zeta}(1-e^{-4\zeta})}\\ \approx&-4\,c\,(1-i)\,\sqrt{\nu_{e2}/\nu_{e1}}\,e^{-2\zeta}\,(1+e^{-4\zeta})\,\coth\zeta\,.\end{aligned}\tag{3.52}$$

and, in order to compare the two-layer model and Elipot and Gille [2009], a relative quantity ($\boldsymbol{\Delta}_{1\{TL-EG\}}$) is introduced:

$$\boldsymbol{\Delta}_{1\{TL-EG\}}=\left|\frac{\boldsymbol{U}_{TL}(0)-\boldsymbol{U}_{EG}(0)}{\boldsymbol{U}_{EG}(0)}\right|=\left|\frac{-4\,\sqrt{\nu_{e2}}}{(e^{\zeta}+e^{-\zeta})^2\,(\sqrt{\nu_{e2}}+\sqrt{\nu_{e1}}\,\tanh\zeta)}\right|.\tag{3.53}$$

The magnitude of $\boldsymbol{\Delta}_{1\{TL-EG\}}$ for various parameters are plotted in figure (3.10), also the difference between the angle of the surface current ($\Delta\Phi_{\{TL-EG\}}=\Phi_{TL}-\Phi_{EG}$) of

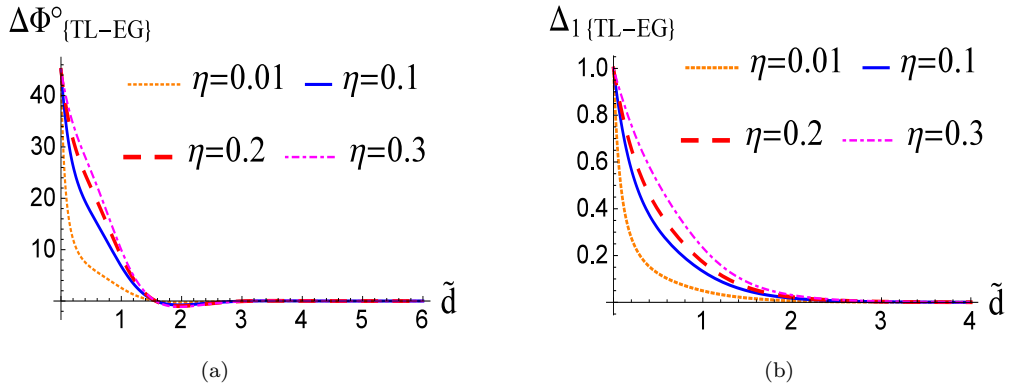

FIGURE 3.10: (a) The predicted angle of the surface current of two-layer model compared with Elipot and Gille model ($\Delta\Phi_{\{TL-EG\}} = \Phi_{TL} - \Phi_{EG}$) for a steady wind. (b) Dependence of normalised discrepancy ($\boldsymbol{\Delta}_{1\{TL-EG\}} = |\boldsymbol{U}_{TL}(0) - \boldsymbol{U}_{EG}(0)|/|\boldsymbol{U}_{EG}(0)|$) on the non-dimensional depth $\tilde{d}$ for particular values of parameters: $\eta = 0.01, 0.1, 0.2, 0.3$ ($\eta = \nu_{e2}/\nu_{e1}$). Φ_{TL} and Φ_{EG} are given by eqs.(3.43) and (3.38) respectively.

both models: Two-layer model and Elipot and Gille [2009] is shown in figure (3.10).

3.4 Can stratification profile be probed remotely by HF radar?

Of great importance would have been a possibility of remote sensing of turbulence level in the mixed layer, the presence/absence of diurnal stratification, the depth of the mixed layer and strength of stratification in the pycnocline. In the previous section we examined how the speed and direction of the surface current depend on the depth of the mixed layer, eddy viscosity in the mixed layer and below within the framework of two-layer model. The surface velocity now is measured remotely from satellites with improving accuracy and resolution, from the shore by various techniques. High-frequency (HF) radar devices are a widely used tool of monitoring of the sea-surface. In particular, the sea-echo Doppler spectra of HF radars are used for probing surface currents (e.g. Broche et al. [1987], Paduan and Graber [1997], Wyatt [2000]), while the search continues for ways of remote sensing of other aspects of air-sea interaction (Shrira and Forget [2015]). Here we briefly discuss additional

possibilities provided by HF radars in view of remote sensing of the characteristics of the upper ocean listed above. The HF (high frequency) radar measurements are utilising the fact that in the HF range of frequencies electromagnetic waves are scattered by random wavy water surface in the Bragg regime, where a monochromatic electromagnetic wave emitted with a wavenumber k_E is reflected back primarily by the resonant Bragg wave number $k_B = k_E/2$ of the water surface. By analysing the Doppler spectra which exhibit easily identifiable Bragg peaks it is straightforward to find the phase velocity of the wave components associated with the peaks. By subtracting the phase velocities prescribed by the linear dispersion one gets a correction due to surface currents. Although the main contribution to the EM scattering comes from the Bragg resonant wave of length $2\pi/k_B$, water waves are nonlinear and each free Fourier component has also bound waves. The second in importance contribution is due to bound waves having the same resonant wavenumber k_B which are associated with a free wave of wavelength twice the Bragg one (Shrira et al. [2001]). The correction due to surface current depends on the wavenumber under consideration. With a good accuracy it could be approximated by the Stewart-Joy formula (Stewart and Joy [1974]). Applying the Stewart-Joy formula to the wave corresponding to the main Bragg peak and to the second contributor to the scattering - the wave of twice the the Bragg wavelength one gets two integrals of the current,

$$\boldsymbol{U}_{(1)} = 2|\boldsymbol{k}_B| \int_0^\infty \boldsymbol{U}(z,t) e^{-2|\boldsymbol{k}_B|z} dz, \qquad \boldsymbol{U}_{(2)} = |\boldsymbol{k}_B| \int_0^\infty \boldsymbol{U}(z,t) e^{-|\boldsymbol{k}_B|z} dz. \tag{3.54}$$

where $\boldsymbol{U}(z,t)$ is the velocity profile and $|\boldsymbol{k}| = 2\pi/\lambda$ is the Bragg wavenumber. In our further consideration we have chosen a commonly used radar frequency 12 MHz? which corresponds to the wavelength $\lambda = 18\,m$. In the previous section we examined how the properties of the upper ocean manifest themselves in the field of surface velocity $\boldsymbol{U}_0$. The surface velocity is often measured by HF radars and $\boldsymbol{U}_{(1)}$ is usually taken as $\boldsymbol{U}_0$. Here we will attempt to find out when the difference between the integrated velocities $\boldsymbol{U}_{(1)}$ and $\boldsymbol{U}_{(2)}$ and the true surface velocity $\boldsymbol{U}_0$ is noticeable and to discuss the implications for remote sensing of the upper ocean.

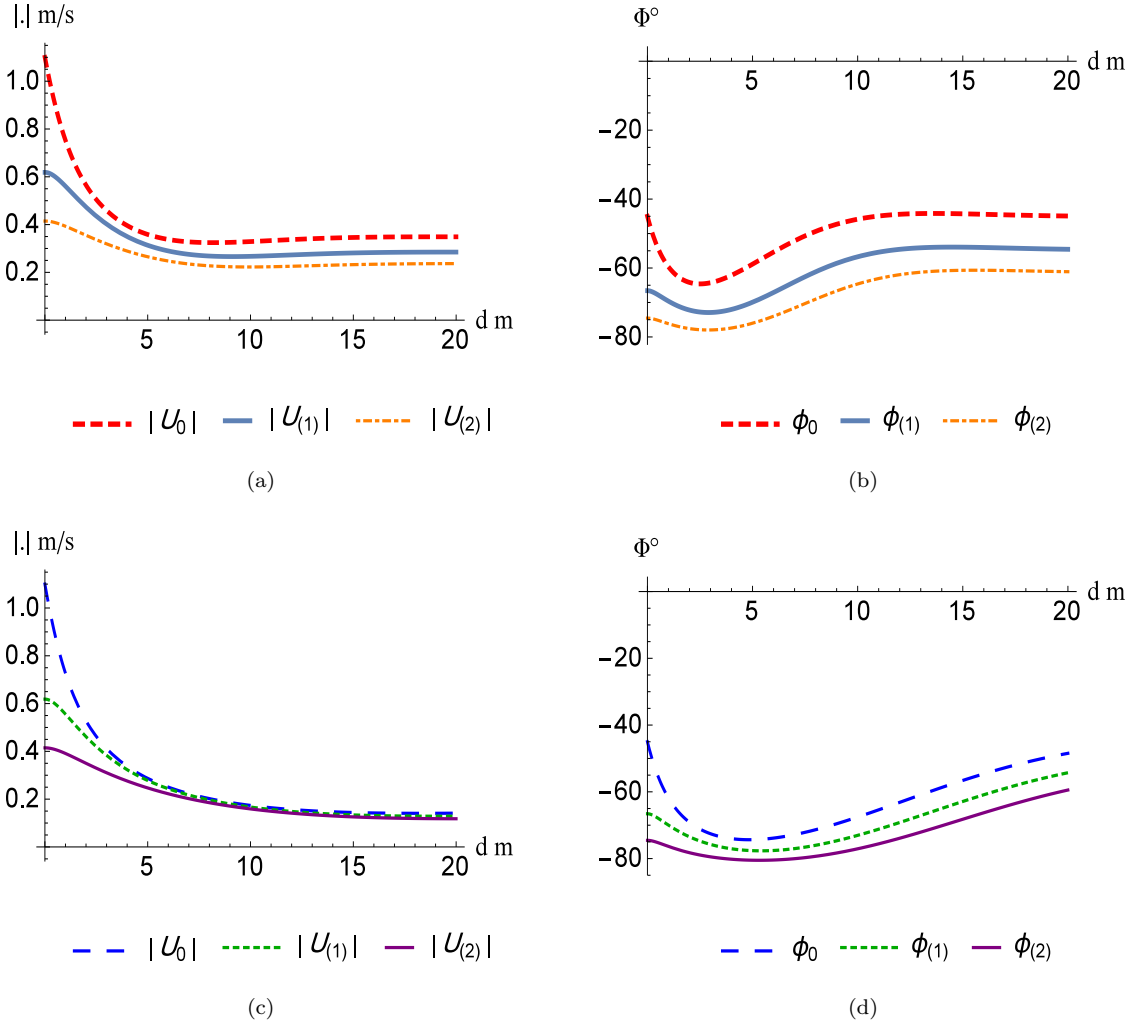

FIGURE 3.11: The velocity fields $\boldsymbol{U}_0$ (velocity at the surface), $\boldsymbol{U}_{(1)}$ and $\boldsymbol{U}_{(2)}$ of the steady flow, when the wind speed (U_{10}) is equal to 10 m/s and viscosity in the lower layer $\nu_{e2} = 2.4 \times 10^{-4}$ $\mathrm{m^2 s^{-1}}$: (a,b) assume turbulent viscosity $\nu_{e1} = 2.4 \times 10^{-3}$ $\mathrm{m^2 s^{-1}}$ in the upper layer, while in (c,d), ν_{e1} taken five times larger. Other parameters values are $f = 10^{-4} \mathrm{s^{-1}}$, $\rho = 1027 \mathrm{kg\ m^{-3}}$ and $\tau_0 = 0.175 \mathrm{N\ m^{-2}}$.

The evolution of surface current for a variety of parameters is shown in figures (3.15, 3.16, 3.17, 3.18). For small value of ν_2 ($O(10^{-5})$,$O(10^{-6})$), the surface current of the two-layer model coincide with a total suppression of turbulence (Elipot and Gille [2009]) model (see figures 3.17, 3.18), while all three models with constant eddy viscosity (classical Ekman model, Elipot and Gille's model and two-layer model) coincide for large depth of the mixed layer ($d = 50$, $d = 100$ m).

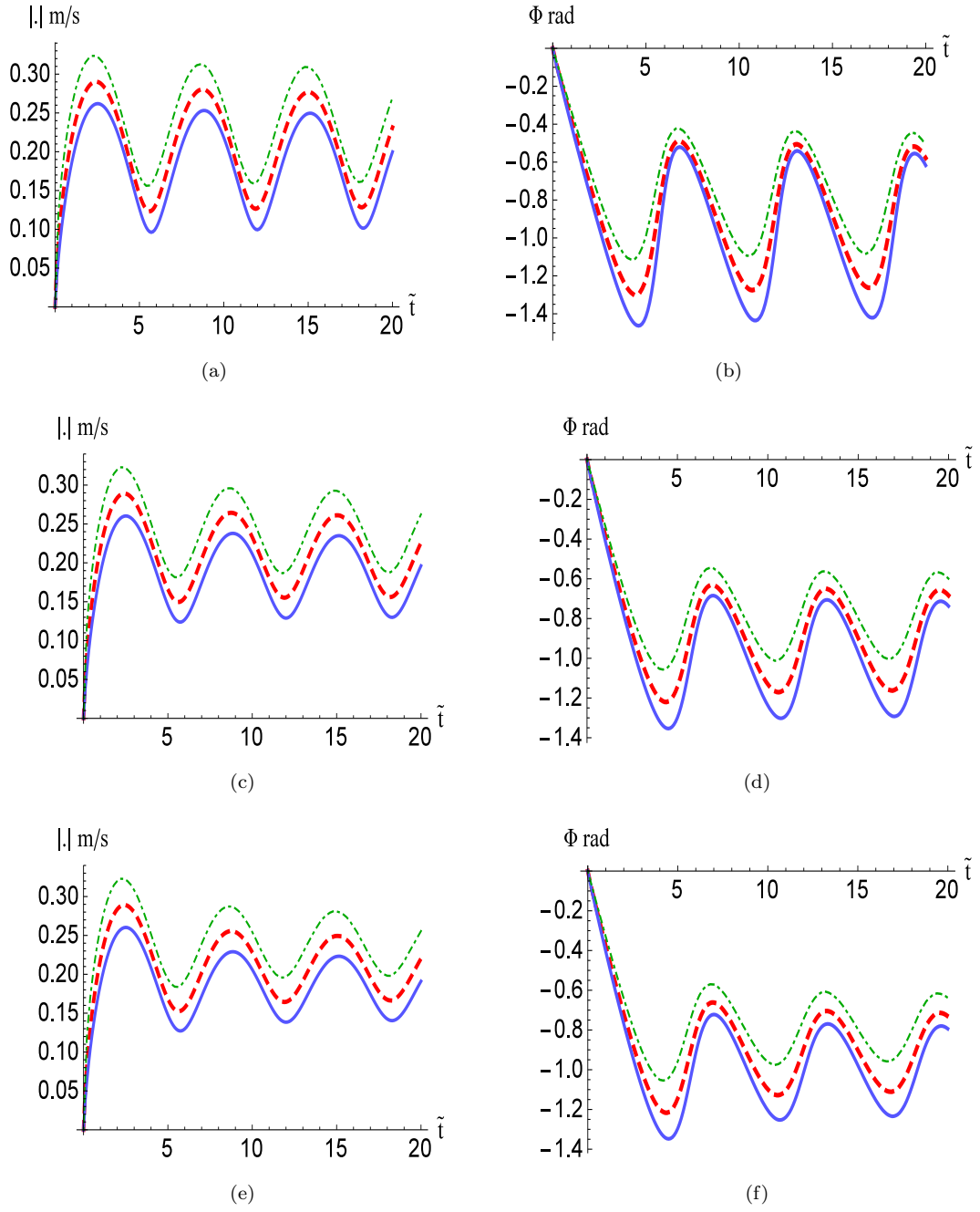

FIGURE 3.12: Differences in surface currents caused by rapid increase of wind from 0 to 10 m s^{-1} as seen by HF radar for various characteristics of mixed layer and stratification. $\boldsymbol{U}_0$ (dot-dashed line), $\boldsymbol{U}_{(1)}$ (dashed line), $\boldsymbol{U}_{(2)}$ (solid line). (a,b): $d = 20$ m; (c,d): $d = 30$ m; (e,f): $d = 40$ m. Other parameters values are $f = 10^{-4}\text{s}^{-1}$, $\rho = 1027\text{kg m}^{-3}$, $\tau_0 = 0.175\text{N m}^{-2}$, $\nu_{e1} = 5 \times 10^{-3}$ m^2s^{-1} and $\nu_{e1} = 5 \times 10^{-3}$ m^2s^{-1}, $\nu_{e2} = 5 \times 10^{-5}$ m^2s^{-1}.

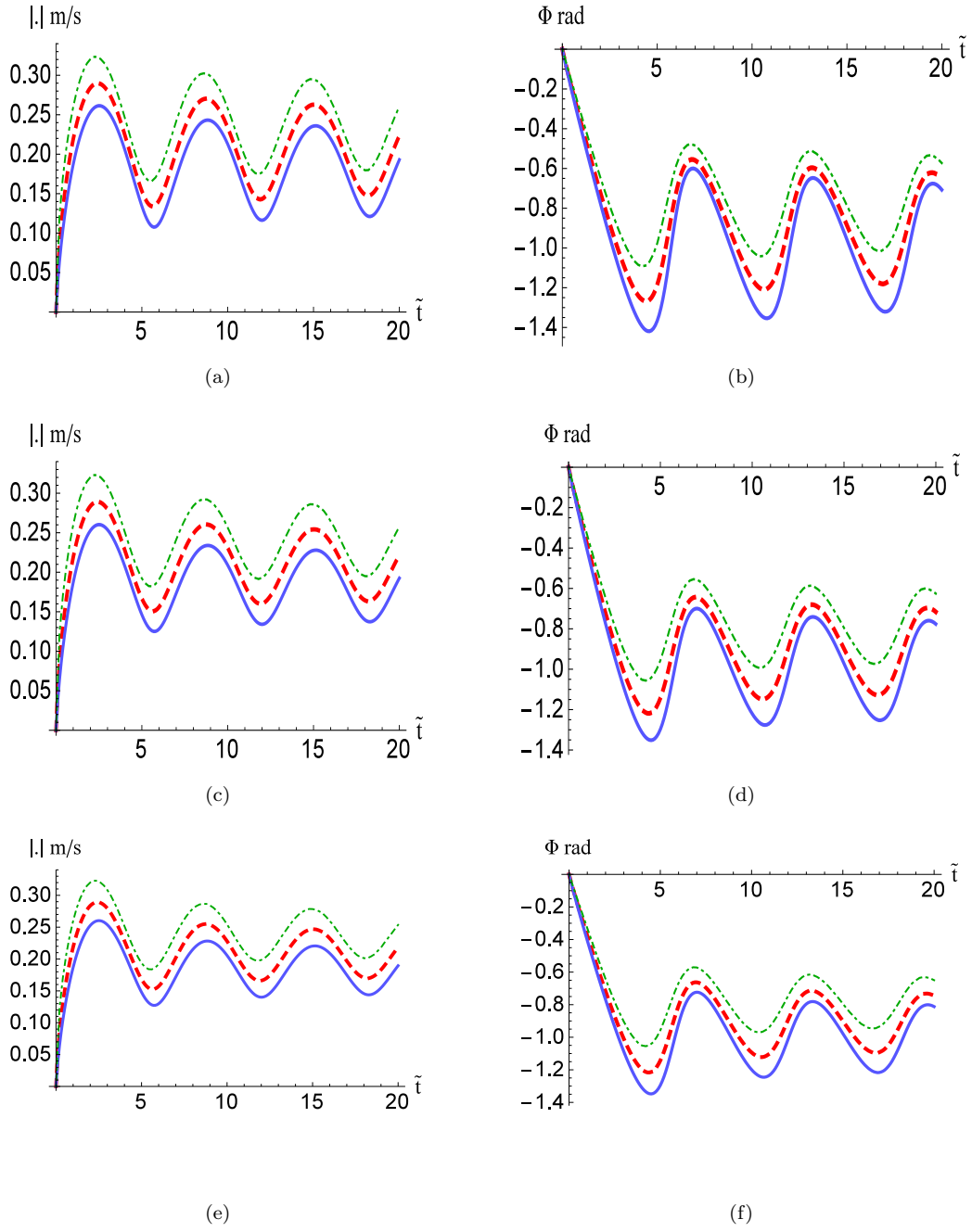

FIGURE 3.13: The velocity fields $\boldsymbol{U}_0$ (velocity at the surface), $\boldsymbol{U}_{(1)}$ and $\boldsymbol{U}_{(2)}$ of the unsteady flow caused by a sharp increase of wind (from 0 to 10m s^{-1}). (a,b): $d = 20$ m; (c,d): $d = 30$ m; (e,f): $d = 40$ m. Other parameters values are $f = 10^{-4}s^{-1}$, $\rho = 1027$kg m^{-3}, $\tau_0 = 0.175$N m^{-2}, $\nu_{e1} = 5 \times 10^{-3}$ m^2s^{-1} and $\nu_{e2} = 5 \times 10^{-4}$ m^2s^{-1}.

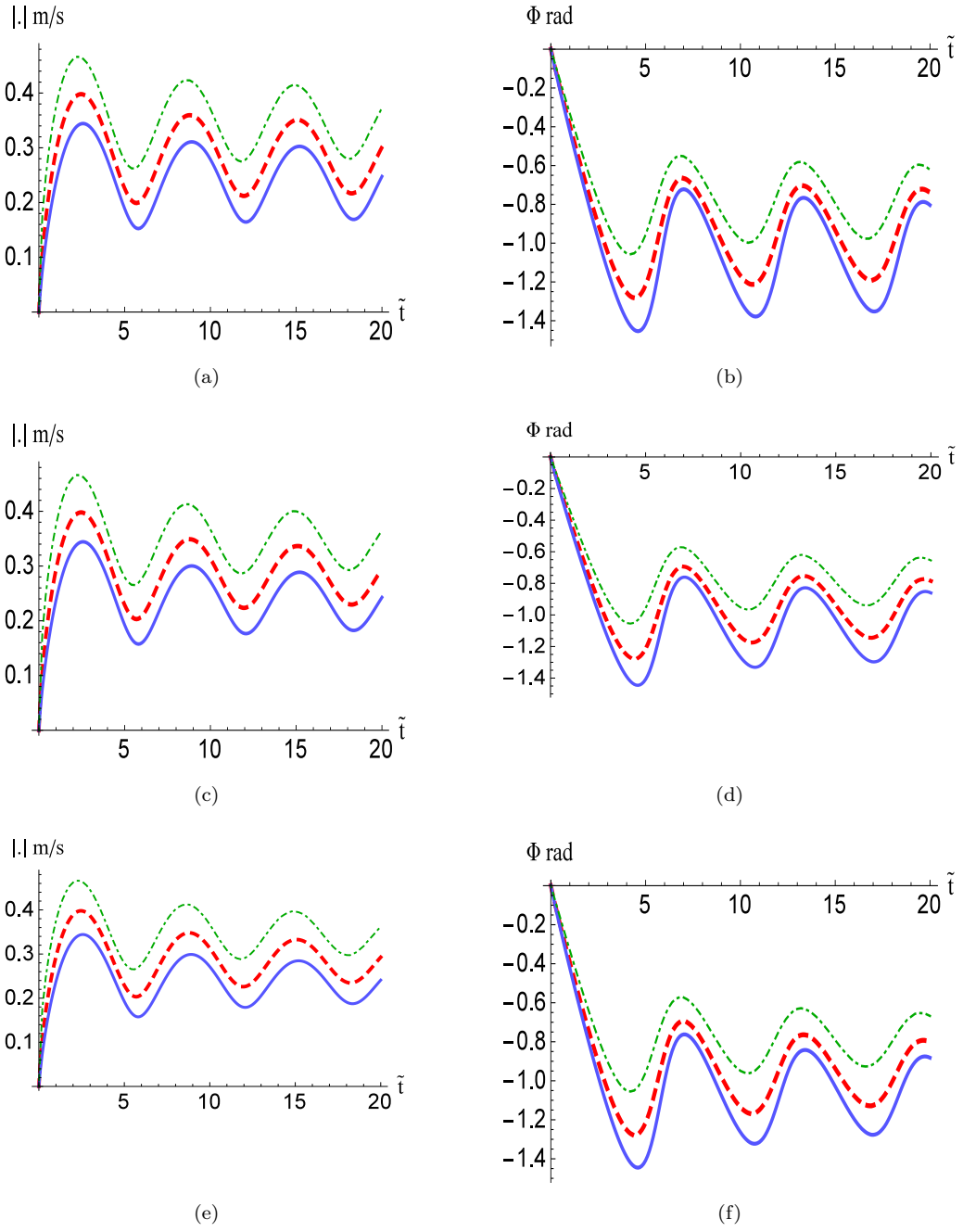

FIGURE 3.14: Another example of the differences in surface currents caused by rapid increase of wind from 0 to 10 m s^{-1} as seen by HF radar for various characteristics of mixed layer and stratification. $\boldsymbol{U}_0$ (velocity at the surface), $\boldsymbol{U}_{(1)}$ and $\boldsymbol{U}_{(2)}$. (a,b): $d = 20$ m; (c,d): $d = 30$ m; (e,f): $d = 40$ m. $\nu_{e1} = 2.4 \times 10^{-3}$ $m^2 s^{-1}$, $\nu_{e2} = 2.4 \times 10^{-4}$ $m^2 s^{-1}$.

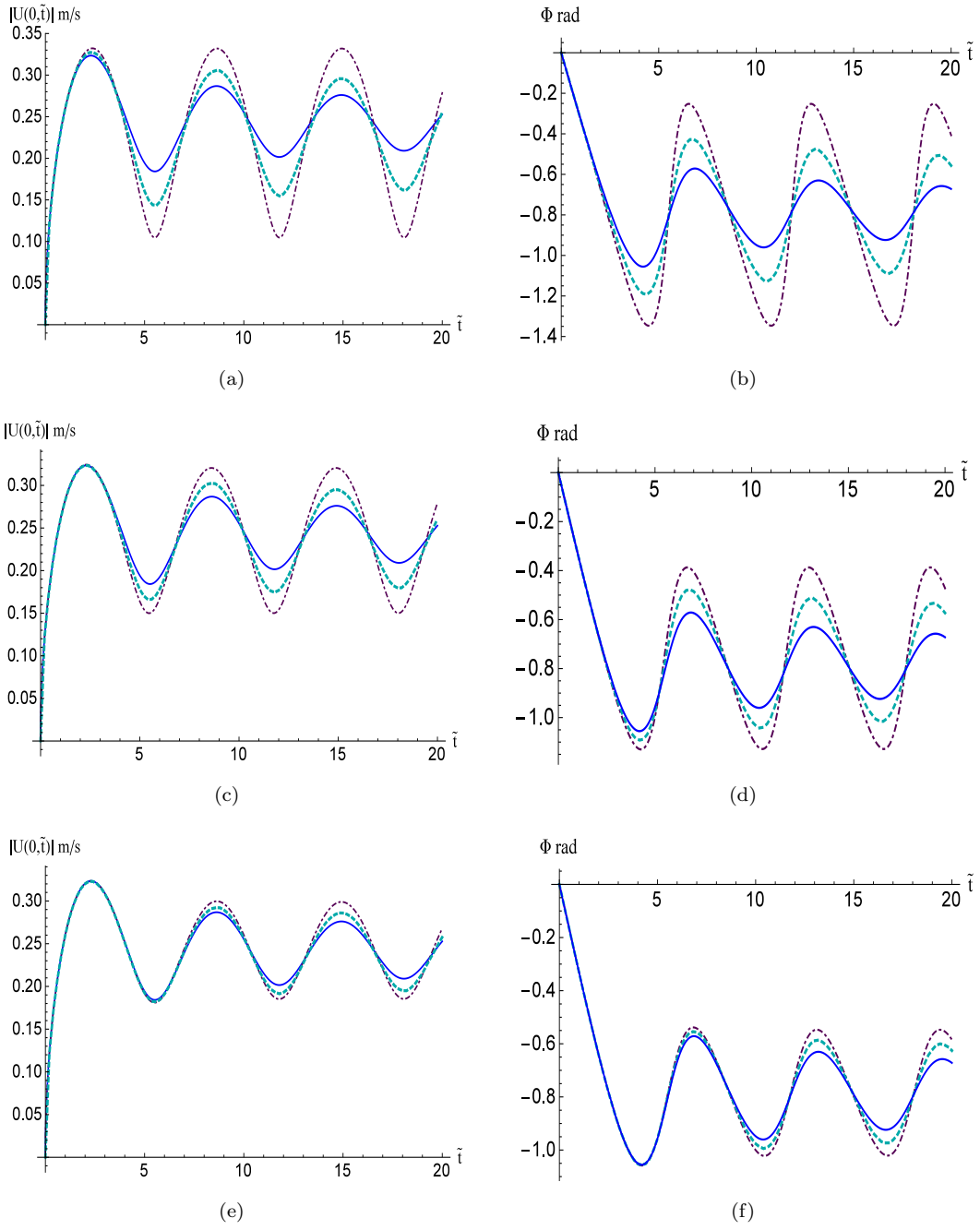

FIGURE 3.15: Differences in the evolution of the surface current for different models: the classical Ekman model (solid line), one-layer model with vanishing shear stress at the bottom of the mixed layer (dot-dashed line), and the two-layer model (dotted line). (a,b): $d = 15$ m; (c,d): $d = 20$ m; (e,f): $d = 30$ m. Other parameters values are $f = 10^{-4}\text{s}^{-1}$, $\rho = 1027\text{kg m}^{-3}$, $\tau_0 = 0.175\text{N m}^{-2}$, $\nu_{e1} = 5 \times 10^{-3}$ m^2s^{-1} and $\nu_{e2} = 5 \times 10^{-4}$ m^2s^{-1}.

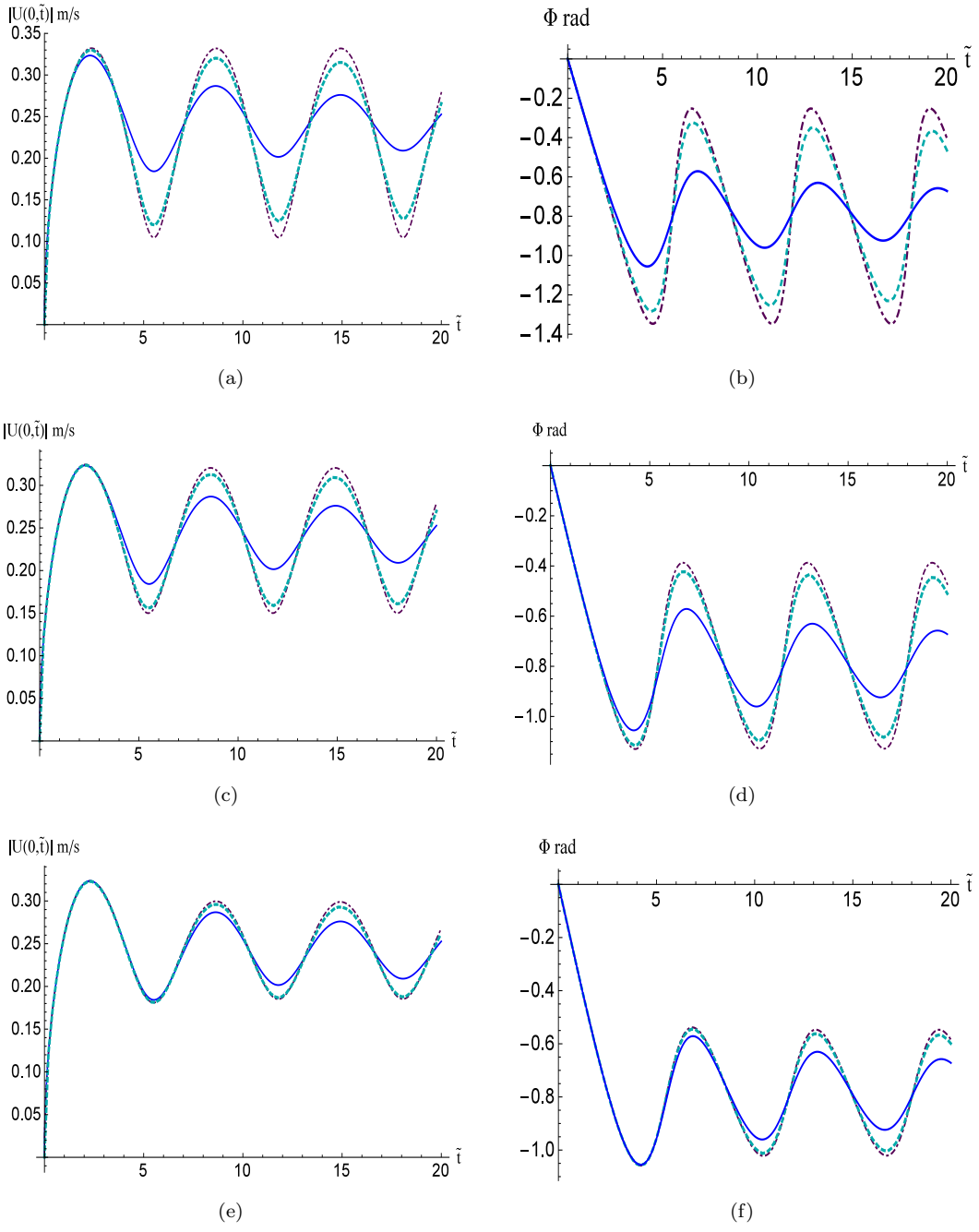

FIGURE 3.16: The development of the surface current due to a sudden increase of wind. Current magnitude at the surface and the angle between the surface current and the wind: the classical Ekman solution is shown by solid line, unsteady Ekman solution satisfying the boundary condition $\boldsymbol{U}' = 0$ at the bottom of the mixed layer is shown by dot-dashed line, and the two-layer solution is shown by dotted line. (a,b): $d = 15$ m; (c,d): $d = 20$ m; (e,f): $d = 30$ m. Other parameters values are $f = 10^{-4}\text{s}^{-1}$, $\rho = 1027\text{kg m}^{-3}$, $\tau_0 = 0.175\text{N m}^{-2}$, $\nu_{e1} = 5 \times 10^{-3}\,\text{m}^2\text{s}^{-1}$ and $\nu_{e2} = 5 \times 10^{-5}\ \text{m}^2\text{s}^{-1}$.

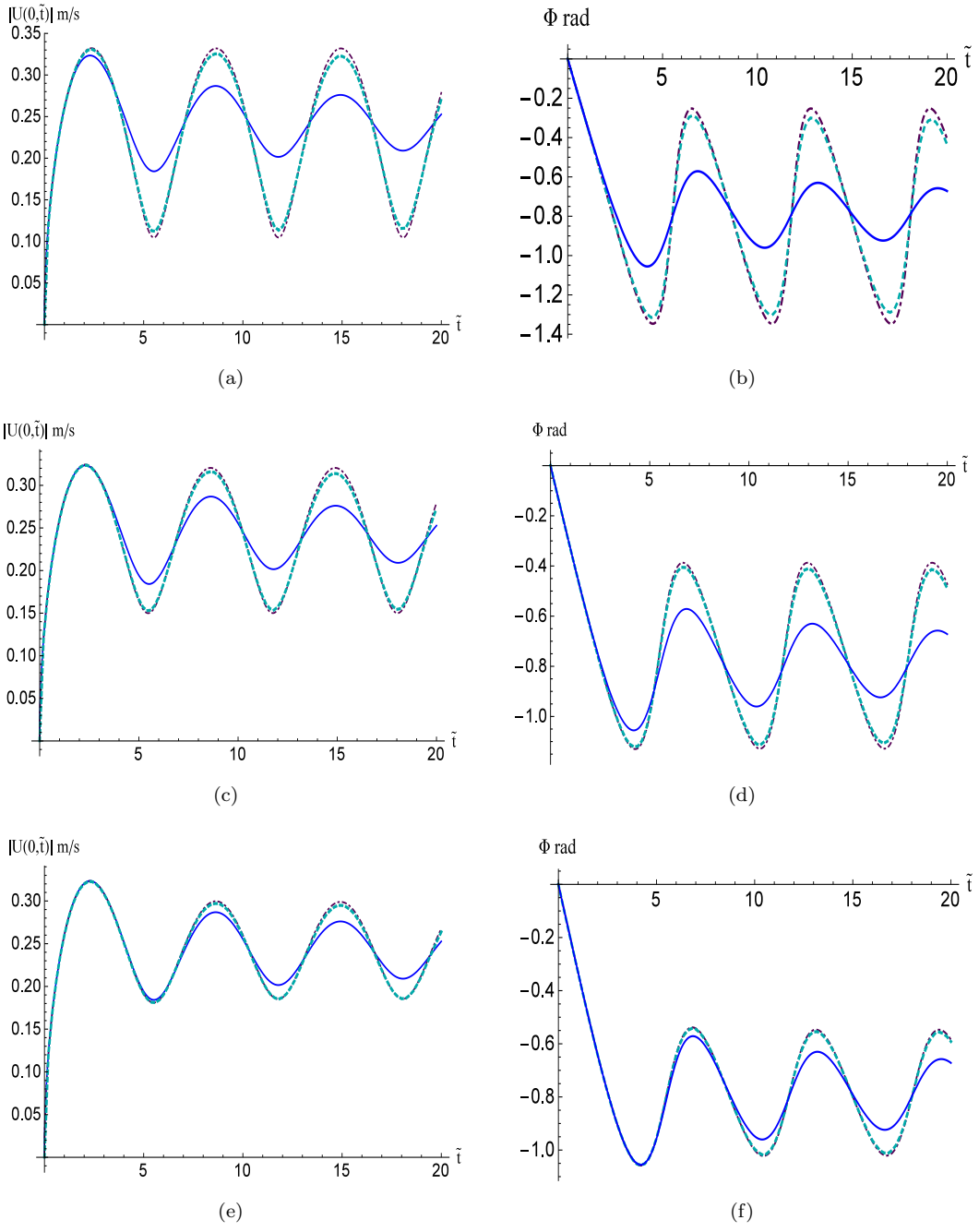

FIGURE 3.17: The development of the surface current due to a sudden increase of wind. Current magnitude at the surface and the angle between the surface current and the wind: the classical Ekman solution is shown by solid line, unsteady Ekman solution satisfying the boundary condition $\boldsymbol{U}' = 0$ at the bottom of the mixed layer is shown by dot-dashed line, and the two-layer solution is shown by dotted line. (a,b): $d = 15$ m; (c,d): $d = 20$ m; (e,f): $d = 30$ m. Other parameters values are $f = 10^{-4}\text{s}^{-1}$, $\rho = 1027\text{kg m}^{-3}$, $\tau_0 = 0.175\text{N m}^{-2}$, $\nu_{e1} = 5 \times 10^{-3}$ m^2s^{-1} and $\nu_{e2} = 10^{-5}$ m^2s^{-1}.

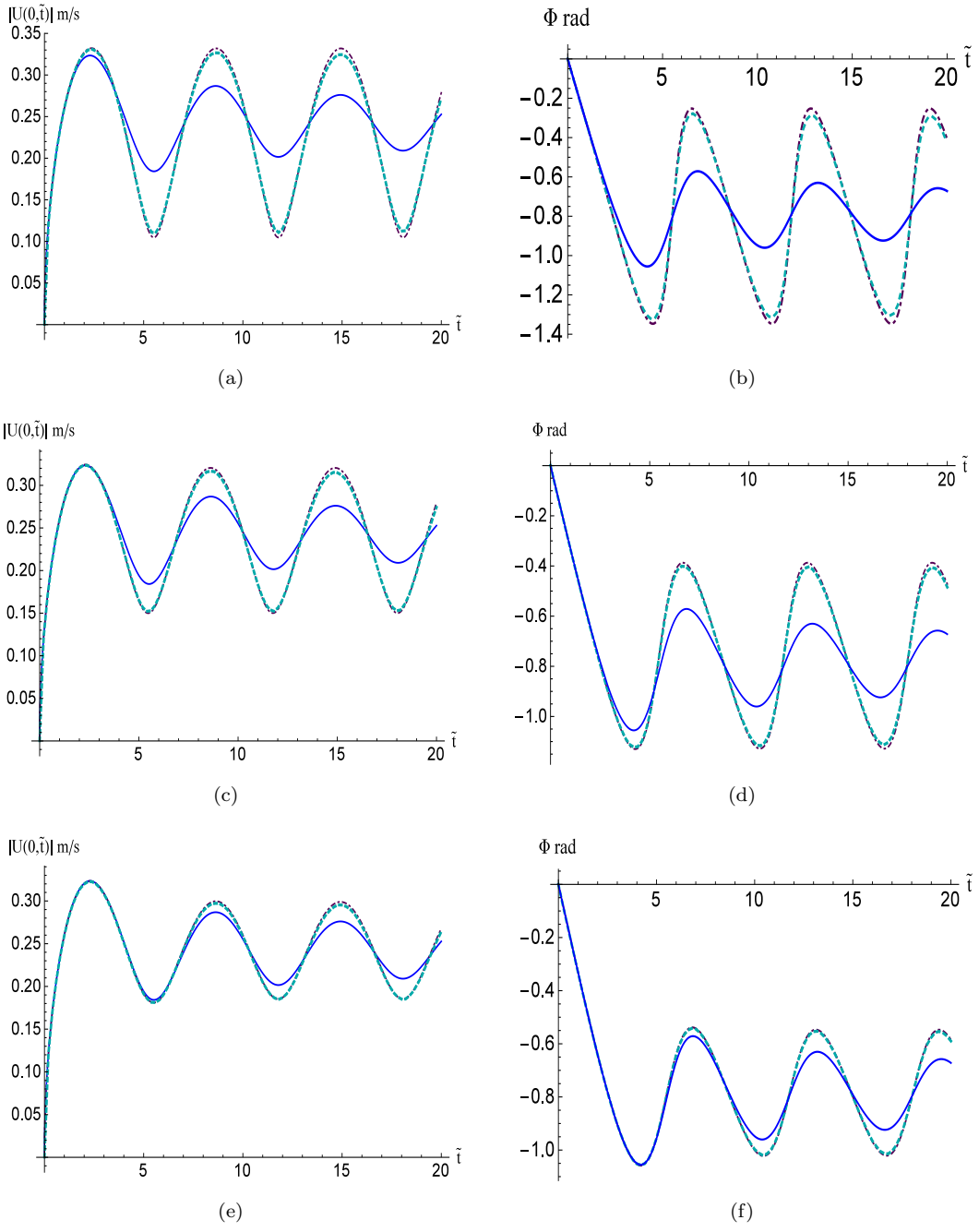

FIGURE 3.18: The development of the surface current due to a sudden increase of wind. Current magnitude at the surface and the angle between the surface current and the wind: the classical Ekman solution is shown by solid line, unsteady Ekman solution satisfying the boundary condition $\boldsymbol{U}' = 0$ at the bottom of the mixed layer is shown by dot-dashed line, and the two-layer solution is shown by dotted line. (a,b): $d = 15$ m; (c,d): $d = 20$ m; (e,f): $d = 30$ m. Other parameters values are $f = 10^{-4}\text{s}^{-1}$, $\rho = 1027\text{kg m}^{-3}$, $\tau_0 = 0.175\text{N m}^{-2}$, $\nu_{e1} = 10^{-2}/2$ m^2s^{-1} and $\nu_{e2} = 10^{-5}/2$ m^2s^{-1}.

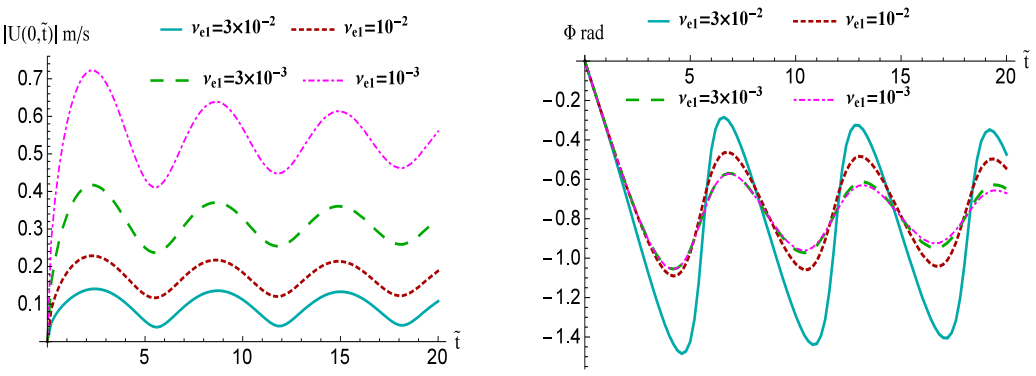

FIGURE 3.19: Evolution of the surface current for two-layer model with different eddy viscosity values (ν_{e1}) in the upper layer. (a) The magnitude of the surface current. (b) The deflection angle of the surface current to the wind direction. Parameters values: $f = 10^{-1}\,\mathrm{s}^{-1}$, $\rho = 1027\,\mathrm{kg\,m}^{-3}$, $\tau_0 = 0.175\,\mathrm{N\,m}^{-2}$, $\nu_{e2} = 3\times10^{-4}\,\mathrm{m}^2\mathrm{s}^{-1}$ and $d = 30\,\mathrm{m}$.

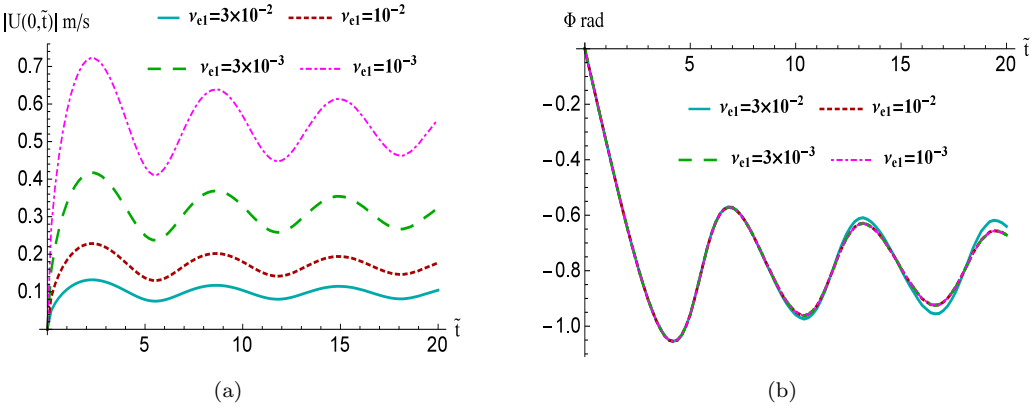

FIGURE 3.20: Evolution of the surface current for two-layer model with different eddy viscosity values (ν_{e1}) in the upper layer. (a) The magnitude of the surface current. (b) The deflection angle of the surface current to the wind direction. Parameters values: $f = 10^{-1}\,\mathrm{s}^{-1}$, $\rho = 1027\,\mathrm{kg\,m}^{-3}$, $\tau_0 = 0.175\,\mathrm{N\,m}^{-2}$, $\nu_{e2} = 3\times10^{-4}\,\mathrm{m}^2\mathrm{s}^{-1}$ and $d = 100\,\mathrm{m}$.

Figures (3.19) and (3.20) illustrate sensitivity of the Ekman transient current caused by a sharp increase of wind to the value of eddy viscosity in the mixed layer and its thickness within the framework of the two-layer model. The main conclusions are very simple and robust: (i) An order of magnitude increase of eddy viscosity leads to a more than twofold decrease of the mean Ekman current speed and amplitude of near-inertial oscillations, independently of the depth of the mixed layer. (ii) The deflection of the current to the direction of wind is sensitive to viscosity only in

the case of shallow mixed layer, then, counterintuitively, inertial oscillations of the direction are most pronounced for the largest viscosity; in the case of a thick mixed layer neither the mean deflection nor the its inertial oscillations are sensitive to the viscosity. Our overall conclusion is the Ekman response is sensitive to the value of viscosity on the mixed layer, we note increase of the timescale of the Ekman layer development with increase of viscosity. The periods of near-inertial oscillations do not depend on viscosity.

An overview of the collection of examples presented in this section enables us to conclude that there are measurable discrepancies between the true surface velocity $\boldsymbol{U}_0$ and the surface velocities $\boldsymbol{U}_{(1)}$, $\boldsymbol{U}_{(2)}$ retrieved by HF radars for a very wide range conditions. The conditions have been outlined within the framework of the two-layer model. These discrepancies can provide quantitative estimates of the level of turbulence in the mixed layer and thickness of of the mixed layer. To a lesser extent these discrepancies can constrain the estimates of the stratification in the pycnocline. Once applied to real field observations the above results can provide a valuable insight into an important aspect of air-sea interaction.

3.5 Dynamics in case of wind switch-off

To understand the response of decreasing wind, here we consider a complete switch-off of the wind assuming the eddy viscosity to remain constant in both layers.

We divide this section into two parts: in the first one we give the mathematical formulation of the governing equations, while the Laplace inversion scheme and "the Stehfest inversion algorithm" are explained in the other part.

3.5.0.1 Governing equations and Laplace transform

The governing equations are the same equations (3.1):

$$\frac{\partial \boldsymbol{U}_1}{\partial t} + if\boldsymbol{U}_1 = \nu_{e1}\frac{\partial^2 \boldsymbol{U}_1}{\partial z^2}; \quad 0 \le z \le d\,, \qquad \frac{\partial \boldsymbol{U}_2}{\partial t} + if\boldsymbol{U}_2 = \nu_{e2}\frac{\partial^2 \boldsymbol{U}_2}{\partial z^2}; \quad d \le z < \infty\,.$$

The initial conditions are provided by the solution for the steady Ekman current:

$$\boldsymbol{U}_1(z,0) = \boldsymbol{V}_0\left(\sqrt{\nu_{e2}}\sinh\left[\beta_1(d-z)\right] + \sqrt{\nu_{e1}}\cosh\left[\beta_1(d-z)\right]\right), \tag{3.55a}$$

$$\boldsymbol{U}_2(z,0) = \sqrt{\nu_{e1}}\,\boldsymbol{V}_0\exp\left[\beta_2(d-z)\right], \tag{3.55b}$$

where

$$\begin{aligned}\boldsymbol{V}_0 =& \frac{\boldsymbol{\tau}_0\, e^{-i\,\pi/4}}{\rho\sqrt{f\nu_{e1}}\left(\sqrt{\nu_{e1}}\sinh(\beta_1 d) + \sqrt{\nu_{e2}}\cosh(\beta_1 d)\right)},\\ \beta_1 =& (1+i)\sqrt{\frac{f}{2\nu_{e1}}},\\ \beta_2 =& (1+i)\sqrt{\frac{f}{2\nu_{e2}}}.\end{aligned}$$

The boundary conditions for $t \geq 0$ are:

$$\frac{\partial \boldsymbol{U}_1}{\partial z} = 0 \qquad at \quad z = 0, \tag{3.56a}$$

$$\nu_{e1}\frac{\partial \boldsymbol{U}_1}{\partial z} = \nu_{e2}\frac{\partial \boldsymbol{U}_2}{\partial z} \quad at \quad z = d, \tag{3.56b}$$

$$\boldsymbol{U}_1 = \boldsymbol{U}_2 \qquad at \quad z = d, \tag{3.56c}$$

$$\boldsymbol{U}_2 \to 0 \qquad as \quad z \to \infty. \tag{3.56d}$$

Applying the Laplace transform with respect to t:

$$\hat{\boldsymbol{U}}(z,s) = \int_0^\infty e^{st}\,\boldsymbol{U}(z,t)\,dt, \quad Re(s) \geq 0. \tag{3.57}$$

leads to ordinary differential equations

$$\nu_{e1}\frac{d^2\hat{\boldsymbol{U}}_1(z,s)}{dz^2} = (if+s)\,\hat{\boldsymbol{U}}_1(z,s) - \boldsymbol{U}_1(z,0), \tag{3.58a}$$

$$\nu_{e2}\frac{d^2\hat{\boldsymbol{U}}_2(z,s)}{dz^2} = (if+s)\,\hat{\boldsymbol{U}}_2(z,s) - \boldsymbol{U}_2(z,0). \tag{3.58b}$$

The general solution of the equation (3.58a) is

$$\hat{\boldsymbol{U}}_1(z,s) = \hat{\boldsymbol{U}}_{1h}(z,s) + \hat{\boldsymbol{U}}_{1p}(z,s), \tag{3.59}$$

where $\hat{\boldsymbol{U}}_{1h}(z,s)$ is the general solution of the homogeneous problem.

$$\hat{\boldsymbol{U}}_{1h}(z,s) = A\,\exp\left[\beta_3\, z\right] + B\,\exp\left[-\beta_3\, z\right]\,, \tag{3.60}$$

where

$$\beta_3 = \sqrt{\frac{s+if}{\nu_{e1}}}\,.$$

The particular solution is

$$\hat{\boldsymbol{U}}_{1p}(z,s) = \frac{\boldsymbol{V}_0}{s}\left(\sqrt{\nu_{e2}}\sinh\left[\beta_1(d-z)\right] + \sqrt{\nu_{e1}}\cosh\left[\beta_1(d-z)\right]\right)\,, \tag{3.61}$$

so that, the general solution of the upper layer can be written as:

$$\hat{\boldsymbol{U}}_1(z,s) = A\,\exp\left[\beta_3\, z\right] + B\,\exp\left[-\beta_3\, z\right] + \frac{\boldsymbol{V}_0}{s}\left(\sqrt{\nu_{e2}}\sinh\left[\beta_1(d-z)\right] + \sqrt{\nu_{e1}}\cosh\left[\beta_1(d-z)\right]\right)\,. \tag{3.62}$$

Similarly, the general solution of the equation (3.58b) is

$$\hat{\boldsymbol{U}}_2(z,s) = c_1\exp\left[\beta_4 z\right] + c_2\exp\left[-\beta_4 z\right] + \frac{\sqrt{\nu_{e1}}\,\boldsymbol{V}_0}{s}\exp\left[\beta_2(d-z)\right]\,, \tag{3.63}$$

where

$$\beta_4 = \sqrt{\frac{s+if}{\nu_{e2}}}\,.$$

After applying the transformed boundary conditions, the solution of the upper layer in the Laplace space can be written as

$$\hat{\boldsymbol{U}}_1(z,s) = A\,\exp\left[\beta_3\, z\right] + B\,\exp\left[-\beta_3\, z\right] + \frac{\boldsymbol{V}_0}{s}\left(\sqrt{\nu_{e2}}\sinh\left[\beta_1(d-z)\right] + \sqrt{\nu_{e1}}\cosh\left[\beta_1(d-z)\right]\right)\,,$$

where

$$\begin{aligned} A =& \big(\boldsymbol{V}_0\big(-\beta_1 e^{\beta_3 d}\big(\beta_3\nu_{e1}+\beta_4\nu_{e2}\big)\big(\sqrt{\nu_{e1}}\sinh[\beta_1 d]+\sqrt{\nu_{e2}}\cosh[\beta_1 d]\big)+ \\ & \beta_3\beta_1\sqrt{\nu_{e2}}\nu_{e1}-\beta_3\beta_2\sqrt{\nu_{e1}}\nu_{e2}\big)\big)/\big(2\beta_3 s\big(\beta_4\nu_{e2}\cosh[\beta_3 d]+\beta_3\nu_{e1}\sinh[\beta_3 d]\big)\big)\,, \end{aligned}$$

$$B = \big(\boldsymbol{V}_0 e^{-\beta_3 d}\big(-\beta_1\big(\beta_3\nu_{e1} - \beta_4\nu_{e2}\big)\big(\sqrt{\nu_{e1}}\sinh[\beta_1 d] + \sqrt{\nu_{e2}}\cosh[\beta_1 d]\big) + \beta_3\beta_1\sqrt{\nu_{e2}}\nu_{e1}e^{\beta_3 d} - \beta_3\beta_2\sqrt{\nu_{e1}}\nu_{e2}e^{\beta_3 d}\big)\big)/\big(2\beta_3 s\big(\beta_4\nu_{e2}\cosh[\beta_3 d] + \beta_3\nu_{e1}\sinh[\beta_3 d]\big)\big)\,.$$

The lower layer solution is

$$\hat{\boldsymbol{U}}_2(z,s) = c_2\exp\left[-\beta_4 z\right] + \frac{\sqrt{\nu_{e1}}\,\boldsymbol{V}_0}{s}\exp\left[\beta_2(d-z)\right]\,,$$

where

$$c_2 = -\big(\sqrt{\nu_{e1}}\boldsymbol{V}_0 e^{\beta_4 d}\big(\beta_1\sqrt{\nu_{e1}}\sqrt{\nu_{e2}}(\cosh[\beta_1 d] - \cosh[\beta_3 d]) + \beta_2\nu_{e2}\cosh[\beta_3 d] + \beta_1\nu_{e1}\sinh[\beta_1 d]\big)\big)/\big(s\big(\beta_4\nu_{e2}\cosh[\beta_3 d] + \beta_3\nu_{e1}\sinh[\beta_3 d]\big)\big)\,.$$

The Bromwich integral (the inverse Laplace transform) can not be evaluated easily analytically because of the complexity of the integration function derived above. Therefore a numerical inversion method is required. In the following subsection, one of the most common numerical methods "the Stehfest method" is discussed (e.g. Stehfest [1970]; Wang and Zhan [2015]).

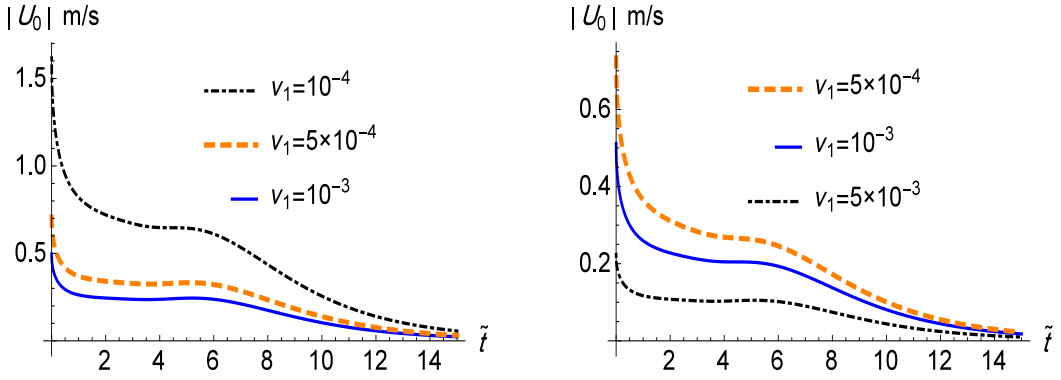

FIGURE 3.21: Evolution of the surface current (the magnitude of the surface current and the angle between the wind and surface current) after the wind switch off for characteristic sample values of parameters: $\tilde{d} = 1.5$. (a): $\nu_{e2} = 10^{-5}\,\mathrm{m^2 s^{-1}}$. (b): $\nu_{e2} = 10^{-4}\,\mathrm{m^2 s^{-1}}$

3.5.0.2 Numerical inverse Laplace transform method

The Stehfest method was developed in the late 1960s, and has been used widely due to its simplicity and good performance. The approximate formula for the inversion of Laplace transform we employ is as follows

$$\mathtt{f}(t) = \frac{ln2}{t} \sum_{\mathtt{j}=1}^{n} M_{\mathtt{j}}\, \mathtt{F}\left(\mathtt{j}\frac{ln2}{t}\right), \tag{3.64}$$

where the coefficient $M_{\mathtt{j}}$ is given by

$$M_{\mathtt{j}} = (-1)^{\mathtt{j}+\frac{n}{2}} \sum_{\mathtt{k}=\frac{\mathtt{j}+1}{2}}^{min(\mathtt{j},\frac{n}{2})} \frac{\mathtt{k}^{(n/2)}(2\mathtt{k})!}{(\frac{n}{2}-\mathtt{k})!\mathtt{k}!(\mathtt{k}-1)!(\mathtt{j}-\mathtt{k})!(2\mathtt{k}-\mathtt{j})!}. \tag{3.65}$$

in which, the number of terms n must be an even integer. The accuracy of the method depends on the choice of n. Increasing n leads to an increase in the precision of results first but then and due to increasing round-off errors, the accuracy declines. Cheng et al. [1994] pointed out that the ideal choice of n should range from 6 to 20. Here, to investigate the sensitivity of the Ekman currents to the values of eddy viscosity we considered a situation of "diurnal pycnocline" as a specific example. Figure (3.21) shows that the magnitude of surface velocity is decreasing gradually and it is quite sensitive to the value of ν_{e1}, while its deflection angle depends quite weakly on it.

3.6 Conclusions

In this chapter we examined a novel two-layer model of Ekman boundary layer which utilises the great disparity in magnitudes of eddy viscosity in the turbulent mixed layer and in stratified flow below. In the model, the top layer is characterized by a constant with respect to depth and time value of eddy viscosity, while the bottom layer has a much smaller viscosity also assumed to be constant. Assuming time dependence of horizontally uniform wind stress $\boldsymbol{\tau}(t)$ on the surface to be given we

have found the boundary layer response to such varying surface stress $\boldsymbol{\tau}(t)$ in a closed analytical form.

1. For an arbitrary $\boldsymbol{\tau}(t)$ we found time-dependent solution which describes dynamics of the Ekman boundary layer in such a model which is an exact solution to the full Navier-Stokes equations under the rigid lid approximation. We examined various steady and unsteady regimes within the framework of the adopted model. It has been shown that in the corresponding limits the solutions tends to the classical Ekman solution for infinitely deep fluid or to the EG one in the limit of vanishing eddy viscosity in the stratified layer. The solution enables one to check a posteriori the validity of the solution and reveals the limitations of the model. Under stronger winds at the bottom of the boundary layer the solution exhibits strong shear, which can cause instability of the interface, which might provide the physical mechanism of the mixed layer deepening and entrainment. To quantify this entrainment mechanism one has to choose one of the existing parameterisations of the eddy viscosity in the stratified fluid, which goes beyond the scope of this study. In the regime of deepening of the mixed layer a more appropriate boundary condition at the bottom of the mixed layer would be constancy of the Richardson number, $Ri = 1/4$.

2. For the steady wind we found and examined explicit solution governing the Ekman flow. The solution suggests a likely strong instability and, hence, enhanced mixing and break down of the assumed horizontal uniformity of the flow. This requires reconsidering the basic assumptions of the Ekman models.

3. In view of advancing remote sensing of the basic characteristics of the mixed layer (such as its thickness, the characteristic value of eddy viscosity and stratification below) we analysed sensitivity of the surface manifestations of the Ekman currents provided by the time-dependent solution for the surface current $\boldsymbol{U}_0(t)$ for various regimes. It has been found that for a very wide range of parameters and regimes of evolution the presence of stratification does manifest in the field of the surface current $\boldsymbol{U}_0(t)$, which is most sensitive to the nondimensional depth of the mixed layer $\tilde{d} = d/\delta_1$, $\delta_1 = \sqrt{2\nu_{e1}/f}$. The manifestations on the

surface are sizeable for $\tilde{d} < 1.5$. Under strong winds the surface manifestations of seasonal stratification are always present. The possibility of getting a new insight by using HF radars measuring the surface currents by integrating the boundary layer of two different depth has been also demonstrated.

Chapter 4

Ocean response to varying wind in models with time and depth dependent eddy viscosity

4.1 Introduction

The unifying feature of the existing theoretical developments of the Ekman theory is that they do not take into account time dependence of the eddy viscosity, which is an obvious oversimplification and a stark neglect of a key feature of reality. Here we extend the Ekman model by considering time (and depth) dependent eddy viscosity. The turbulence in the Ekman layer is known to be time dependent (Soloviev and Lukas [2013]), it is affected by many physical processes, not fully understood yet. We mention just a few: it depends on wind through the wind induced shear and waves, primarily through wave breaking, which is sensitive to the instantaneous wind and wave age (e.g. Komen et al. [1996]; Babanin [2011]); the turbulence is affected by solar heating and heat exchange, which might create density stratification and thus suppress the turbulence; it might be also affected by near-inertial waves trapped

near the surface (Shrira and Forget [2015]), and it has its own dynamics. Here we are not aiming at describing and accounting for specific mechanisms of turbulence temporal variability, we explore how a presumed wind determined time dependence of eddy viscosity manifests in the dynamics of the Ekman current. We choose the (Zikanov et al. [2003]) relation between the eddy viscosity and wind obtained on the basis of large-eddy-simulations for steady regimes; we hope that for not too fast changes of wind the adopted relation captures reality. Even if this is not true, it is important to explore the effects due to time dependent eddy viscosity. We show that once the eddy viscosity closure and tangential stress parametrization of wind effect have been adopted, the Navier-Stokes equations with viscosity varying both in depth and time admit a broad class of novel exact solutions describing dynamics of the Ekman currents. These solutions demonstrate significance of taking into account time dependence of eddy viscosity. This enables us to get a new insight into the vertical and temporal variability of the Ekman currents.

The chapter is organized as follows. First, in §4.2 we formulate the mathematical model and discuss the underpinning assumptions. In §4.3 we derive a class of exact Ekman type solutions for the situations with time and depth dependent eddy viscosity. In §4.4 we examine three basic scenarios of varying wind (all others can be viewed just as combinations of those three): an increase, a decrease, and a periodic variation. We show emergence of fast instabilities of the evolving Ekman currents and strong sensitivity of their parameters to the adopted models of eddy viscosity. In §4.5 we derive general solution for the power law depth dependence of eddy viscosity and arbitrary time dependence of wind. In §5.6 the analysis of the unsteaday Ekman current response is extended by taking into account time dependent surface wave Stokes drift. In the concluding §4.7 we summarise our findings and new questions they generate.

4.2 The mathematical model

The generalization of the Ekman model (1.22) with the boundary conditions (1.23), (1.24) and (1.25) provides the basis of the present study focussed upon elucidating

the effects of time dependent eddy viscosity.

As was discussed in the introduction, the specific time dependence of the eddy viscosity depends on a variety of physical mechanisms, not fully understood yet. Hence, for most of the study, unless we explicitly state an alternative, we assume that the eddy viscosity scales as friction velocity squared, u_*^2, where $u_* = \sqrt{|\boldsymbol{\tau}|/\rho}$ is friction velocity in water. This link between ν_e and u_* has been established for steady flows in (Zikanov et al. [2003]), here, we assume it will hold for sufficiently slowly varying winds. We adopt the constant of proportionality and its latitude dependence established by the simulations of (Zikanov et al. [2003]).

4.3 Solvable model

For an arbitrary $v_e(z,t)$ the only way to proceed is to simulate numerically the boundary value problem (1.22, 1.23, 1.24, 1.25). Here, to advance analytically we consider a particular class of eddy viscosity depth and time dependence assuming $\nu_e(z,t)$ to be in separable form, i.e. $\nu_e(z,t) = \tilde{\nu}_{e1}(t)g(z)$. Then the substitution

$$\boldsymbol{U}(z,t) = e^{-ift}\,\boldsymbol{W}(T,z); \quad T = \int_0^t \tilde{\nu}_{e1}(\xi)d\xi\,, \tag{4.1}$$

turns the governing equation (1.22) into the diffusion equation with a given vertical dependence of the diffusion coefficient $g(z)$:

$$\frac{\partial \boldsymbol{W}}{\partial T} = \frac{\partial}{\partial z}\left(g(z)\frac{\partial \boldsymbol{W}}{\partial z}\right). \tag{4.2a}$$

The boundary and initial conditions take the form:

$$\frac{\partial \boldsymbol{W}}{\partial z} = \frac{-e^{ift(T)}\,\boldsymbol{\tau}(t(T))}{\rho\,\nu_e(z,t(T))} \equiv \boldsymbol{F}(t) \quad \text{at} \quad z = 0\,, \tag{4.2b}$$

$$\frac{\partial \boldsymbol{W}}{\partial z} \to 0 \quad \text{as} \quad z \to \infty, \tag{4.2c}$$

$$\boldsymbol{W}(z,t)|_{t=0} = \boldsymbol{U}(z,0)\,. \tag{4.2d}$$

Under the adopted assumption of the separable form of the eddy viscosity, $\nu_e(z,t) = \tilde{\nu}_{e1}(t)g(z)$, its vertical dependence $g(z)$ by definition does not vary with time. *A priori*, this might be relevant for capturing the real situations when for the timescales under consideration $g(z)$ either remains frozen, e.g. for a situation with a strong pycnocline layer fluid, or $g(z)$ is a linear function, say, $g(z) = g_0 + g_1 z$. The first class of situations could be relevant for a finite thickness mixed layer with vertically uniform or linearly varying with depth time dependent eddy viscosity, such models (although without time dependence) were employed byElipot and Gille [2009]. In this work we do not consider the effects due to stratification (at least explicit effects) and examine a more general class of models with the power law depth dependence of eddy viscosity. However, in the next section we focus on the simplest model of that class that with linear $g(z)$.

4.3.1 Eddy viscosity linearly dependent on depth: $g(z) = g_0 + g_1 z$

Here, we consider eddy viscosity linearly dependent on depth, a more general power law depth dependence will be considered in §4.5. On substituting $\nu_e = \tilde{\nu}_{e1}(t)(g_0+g_1 z)$ into eq.(4.2a) we obtain:

$$\frac{\partial \boldsymbol{W}}{\partial T} = \frac{\partial}{\partial z}\left((g_0 + g_1 z)\frac{\partial \boldsymbol{W}}{\partial z}\right). \tag{4.3}$$

Taking the Laplace transform with respect to T ($\mathcal{L}\{\boldsymbol{W}(T)\} = \hat{\boldsymbol{W}}(s)$) yields:

$$\frac{d}{dz}\left((g_0 + g_1 z)\frac{d\hat{\boldsymbol{W}}}{dz}\right) - s\,\hat{\boldsymbol{W}} = -\boldsymbol{U}(z,0), \qquad \hat{\boldsymbol{W}}(z,s) = \int_0^\infty \boldsymbol{W}(z,T)\,e^{-sT}\,dT. \tag{4.4}$$

Its general solution is expressed in terms of the modified Bessel functions $I_0[.]$ and $K_0[.]$, of the first and second kind, respectively

$$\hat{\boldsymbol{W}}(z,s) = I_0\left[2\sqrt{\frac{(z_0+z)\,s}{g_1}}\right]\left(A - \frac{2}{g_1}\int_0^z K_0\left[2\sqrt{\frac{(z_0+\chi)s}{g_1}}\right]\boldsymbol{U}(\chi,0)d\chi\right) + K_0\left[2\sqrt{\frac{(z_0+z)\,s}{g_1}}\right]\left(B + \frac{2}{g_1}\int_0^z I_0\left[2\sqrt{\frac{(z_0+\chi)s}{g_1}}\right]\boldsymbol{U}(\chi,0)d\chi\right). \quad (4.5)$$

where $z_0 = g_0/g_1$ is the roughness length, A and B are unspecified functions. On applying the bottom and surface boundary condition the solution in terms of the Laplace transform of the solution $\hat{\boldsymbol{W}}(z,s)$ takes the form

$$\hat{\boldsymbol{W}}(z,s) = K_0\left[2\sqrt{\frac{(z_0+z)\,s}{g_1}}\right]\left(\frac{\sqrt{g_1 z_0}}{\sqrt{s}\,K_1\left[2\sqrt{\frac{sz_0}{g_1}}\right]}\,L\left\{\frac{e^{ift(T)}\,\boldsymbol{\tau}(t(T))}{\rho\,\nu_e(0,t(T))}\right\} + \frac{2\sqrt{z_0}\,\boldsymbol{U}(0,0)\,K_0\left[2\sqrt{\frac{sz_0}{g_1}}\right]\,I_0\left[2\sqrt{\frac{sz_0}{g_1}}\right]}{\sqrt{g_1 s}\,K_1\left[2\sqrt{\frac{sz_0}{g_1}}\right]} + \frac{2}{g_1}\int_0^z I_0\left[2\sqrt{\frac{(z_0+\chi)s}{g_1}}\right]\boldsymbol{U}(\chi,0)d\chi\right). \quad (4.6)$$

Then, in the original variables, the solution reads

$$\boldsymbol{U}(z,t) = e^{-ift}\,\boldsymbol{W}(z,T), \quad \boldsymbol{W}(z,T) = \frac{1}{2\,\pi i}\int_{c-i\infty}^{c+i\infty}\hat{\boldsymbol{W}}(z,s)e^{sT}\,ds; \quad c \geq 0. \quad (4.7)$$

This is the general solution for logarithmic boundary layer corresponding to linearly varying viscosity, $g(z) = g_0 + g_1 z$, under arbitrarily varying wind and time dependent viscosity with any current profile $\boldsymbol{U}(z,0)$ at the initial moment. The solution can be simplified for particular cases of interest considered below.

4.3.2 Particular cases

4.3.2.1 Time-dependent viscosity model with $g_0 = 0$ and $\boldsymbol{U}(z,0) = 0$

Often, the linear growth of viscosity with depth is so strong that, when our main interest is in processes in the first meters or tens of meters below the surface, the

nonzero eddy viscosity value at the surface is so insignificant that it can be neglected. When $g_0 = 0$ and $\boldsymbol{U}(z,0) = 0$, the solution takes the form

$$\boldsymbol{U}(z,t) = e^{-ift}\boldsymbol{W}(z,T), \quad \boldsymbol{W}(z,T) = \frac{1}{g_1}\frac{e^{ift(T)}\,\boldsymbol{\tau}(t(T))}{\rho\,\tilde{\nu}_{e1}(t(T))} *_{(T)} \frac{1}{T}e^{-z/g_1 T}, \tag{4.8}$$

where $\Upsilon *_{(T)} \Psi$ is the convolution with respect to T,

$$\Upsilon *_{(T)} \Psi = \int_0^T \Upsilon(T-\xi)\Psi(\xi)d\xi\,.$$

If we set $\tilde{\nu}_{e1}$ to be a constant the solution (4.8) coincides with that of Madsen [1977].

Often, of special interest is the Ekman transport $\boldsymbol{S}$ – the total fluid flux integrated over the Ekman layer. To find the Ekman transport we just integrate the current given by.(4.8) over entire depth,

$$\boldsymbol{S}(t) = e^{-ift}\int_0^T \frac{e^{ift(\zeta)}\boldsymbol{\tau}(t(\zeta))}{\rho\,\tilde{\nu}_{e1}(t(\zeta))}d\zeta = \frac{e^{-ift}}{\rho}\int_0^t e^{if\Theta}\boldsymbol{\tau}(\Theta)d\Theta\,. \tag{4.9}$$

Thus, we verified that in accordance with Sverdrup [1947] the Ekman transport does not depend on the specific viscosity profile and its time dependence.

4.3.2.2 Time-dependent viscosity model with uniform viscosity ($g_1 = 0$) and $\boldsymbol{U}(z,0) = 0$

This is the most direct generalization of the Ekman model with varying in time depth independent viscosity. It might be appropriate for shallow well mixed layers for relatively short time scales. In this case it is easier to get solution directly from the basic equations than from the general solution (4.7). Applying the Laplace transform with respect to T to the diffusion equation and boundary conditions (eqs.(4.2)) we find the general solution in the form

$$\boldsymbol{U}(z,t) = e^{-ift}W(T,z); \quad T = \int_0^t \nu_{e1}(\xi)d\xi, \tag{4.10a}$$

where

$$\boldsymbol{W}(z,T) = \frac{e^{ift(T)}\,\boldsymbol{\tau}(t(T))}{\rho\,\tilde{\nu}_{e1}(t(T))} *_{(T)} \frac{e^{-z^2/4T}}{\sqrt{\pi T}}\,. \tag{4.10b}$$

The found solution (4.10) describes time dependent current in terms of Green's function for an infinite homogeneous ocean when the eddy viscosity varies with time only. When $\tilde{\nu}_{e1}$ is constant, the solution coincides with the Ekman solution. The Ekman transport for this case has the same form as in the general case given by eq.(4.9).

In the next section to elucidate the effect of time dependence of eddy viscosity we examine the basic scenarios of the ocean response to the varying wind within the framework of model (4.2).

4.4 The basic scenarios of the Ekman current response to varying wind

We consider three basic scenarios of varying wind (all others can be viewed just as combinations of these three): (i) an increase or turn of wind ending up with a plateau, (ii) a decrease, and, (iii) a periodic wind. In this section we examine the Ekman current response in each of this scenarios within the framework of the system (4.2) and compare these predictions with those of the models with constant in time eddy viscosity.

4.4.1 Periodic wind

First consider ocean response to an idealized common situation of breeze; for simplicity we model it by assuming a strictly sinusoidal unidirectional wind with diurnal period,

$$\tau(t) = \tau_0\, H(t)\sin^2(\Omega^* \mathrm{t})\,\mathrm{sign}(U_{10}), \quad \text{where} \quad \mathrm{U}_{10} = |\mathrm{U}_{10}^0|\sin(\Omega^* \mathrm{t}), \tag{4.11}$$

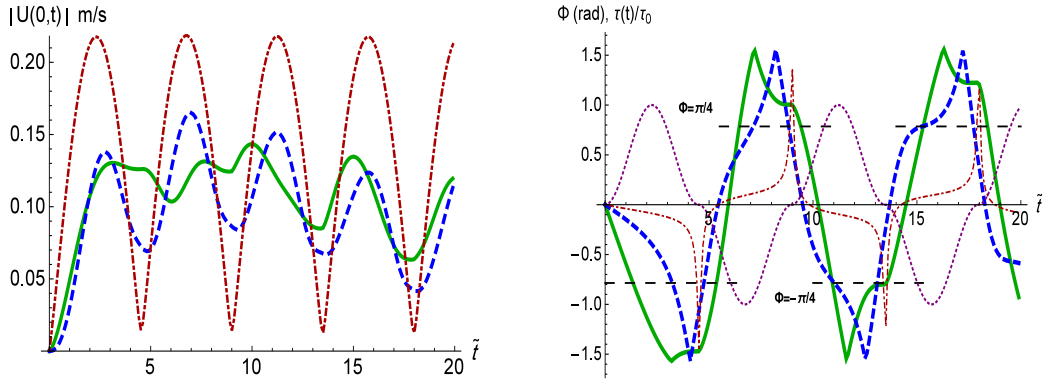

(a) (b)

FIGURE 4.1: Evolution of the Ekman current from rest under a suddenly turned on periodic wind in three different models: time-depth dependent viscosity model (4.7) is shown by dot-dashed line (brown online), the time-dependent viscosity model (4.10) is shown by solid line (green online), the classical Ekman solution with constant eddy viscosity by dashed line (blue online). (a) Current magnitude at the surface $|\boldsymbol{U}(0,t)|$. (b) The angle Φ between the wind and the surface current. $\tilde{t} = ft$. The parameter values are: $f = 10^{-4}\mathrm{s}^{-1}$, $\Omega^* = 0.7f\,\mathrm{rad\,s}^{-1}$, $\nu_0 \approx 2\times10^{-2}\mathrm{m}^2\mathrm{s}^{-1}$, $\rho = 1027\,\mathrm{kg\,m}^{-3}$, $\tau_0 = 0.175\mathrm{N\ m}^{-2}$, $|U_{10}| = 10\mathrm{m\ s}^{-1}$.

where $\tau_0 = \rho_a C_D |\mathrm{U}_{10}^0|^2$, $\rho_a = 1.25\,kg\,m^{-3}$ is the air density, C_D is the drag coefficient taken to be 1.4×10^{-3}, $H(t)$ is the Heaviside Function, Ω^* is the diurnal frequency, and U_{10} is the wind velocity measured at 10m above the still water level. Recall, that in this section $\nu_e(z,t)$ is $\nu_e(z,t) = \tilde{\nu}_{e1}(t)[g_0 + g_1 z]$ and by virtue of (1.23) $\nu_e(0,t)\partial_z \boldsymbol{U}|_{z=0} = -\boldsymbol{\tau}(t)/\rho$.

Figure (4.1) shows an example of evolution of a mid-latitude Ekman current under periodic unidirectional wind (4.11) for two models with time dependent eddy viscosity (with and without linear depth dependence) and the classical Ekman model with constant viscosity as a reference. There are noticeable discrepancies between the predictions of all three models, which shows importance of taking into account of both the time and depth dependence of the eddy viscosity. The model accounting for both the time and depth dependence of viscosity predicts the strongest variation of the surface current magnitude and the sharpest turns of its direction with respect to wind. Note an important feature of the Ekman response: most of the time the surface current is directed windward, in contrast to the steady Ekman response characterized by a significant deflection ($\pi/4$ in the classical Ekman model). Overall, the Ekman currents generated by periodic wind (in all models) show very little resemblance

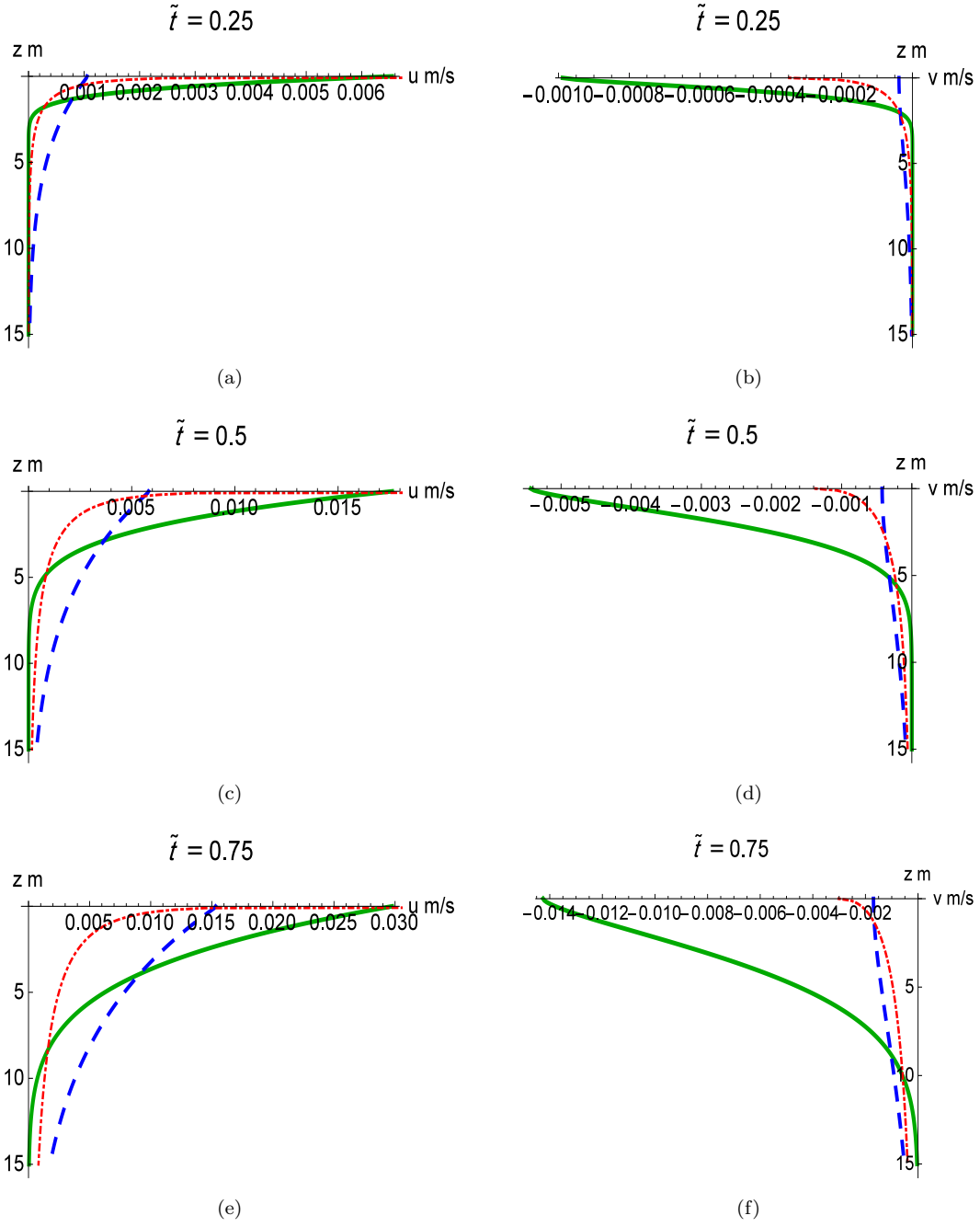

FIGURE 4.2: Vertical profiles of the x and$y$ velocity components generated by a suddenly turned-on periodic wind at three sample moments in three different models: time-depth dependent viscosity model (4.7) is shown by dot-dashed line (red online), the time-dependent viscosity model (4.10)) is shown by solid line (green online), the classical Ekman solution with constant eddy viscosity is plotted by dashed line (blue online). The parameters and expressions for eddy viscosity are the same as in figure 4.1.

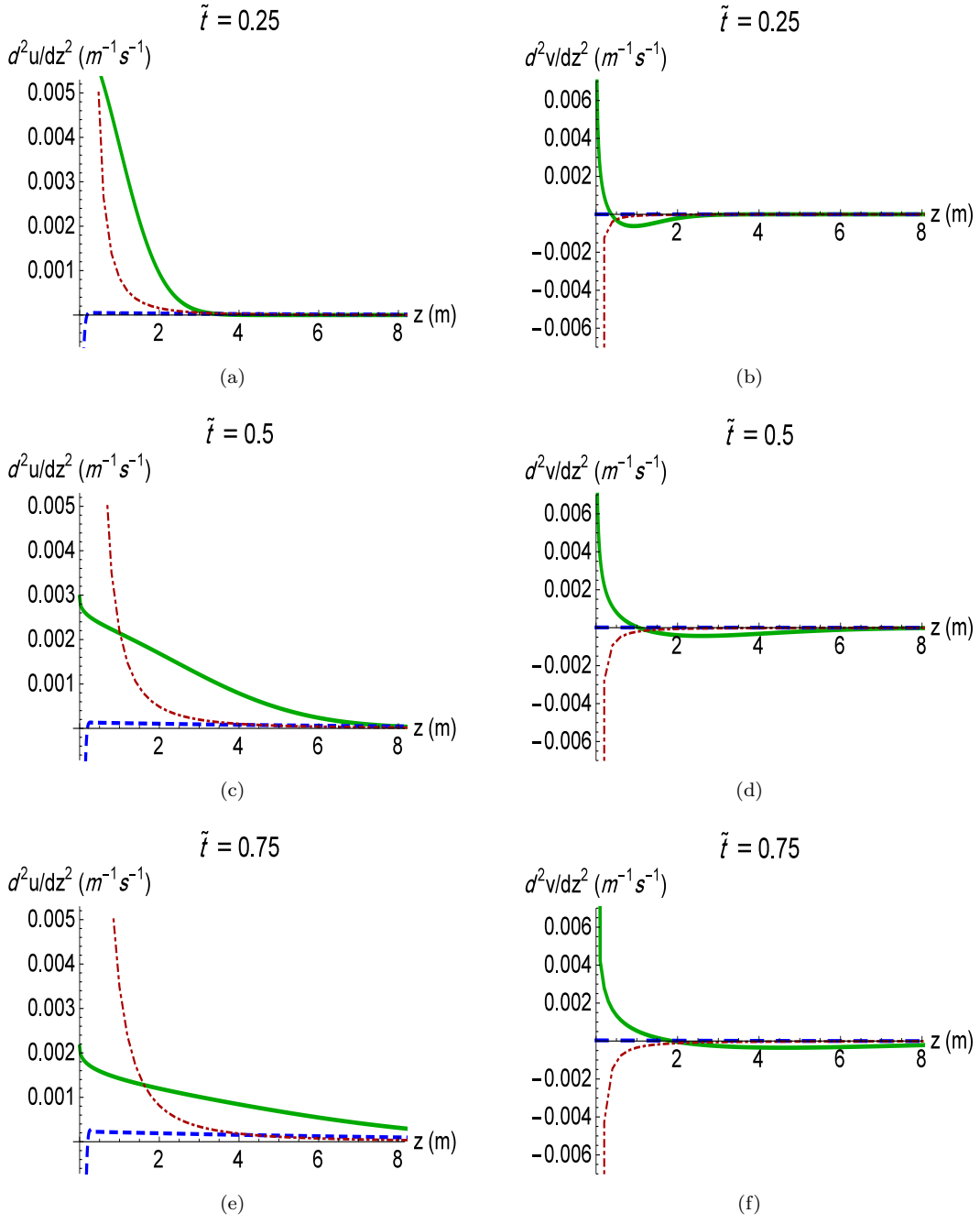

FIGURE 4.3: The second derivative of the profiles shown in figure (4.2).

to the steady solutions, although the diurnal period is not small and, a priori, an adiabatic quasi-steady evolution of the Ekman layer might have been considered as a possibility. This suggests that the characteristic timescale of approaching the steady solution noticeably exceeds the inertial period. With increase/decrease of latitude the pattern of the Ekman current evolution under the same periodic wind remains qualitatively similar: the amplitude of the oscillations differs slightly from those in figure (4.1a), it decreases/increases by about 10% at the latitudes 70 and 20 degrees, respectively, while the evolution of the deflection angle Φ (the between the surface velocity and wind direction) proved to be independent of latitude and, hence, exactly coincides (in units of time scaled with f) with that shown in figure (4.1b).

The discrepancies between the predictions of all three models are not confined to the ocean surface, the really profound differences occur beneath the surface. To give an idea on the flow evolution we draw instantaneous profiles of the current and its second derivatives sampled at three consecutive moments chosen somewhat arbitrarily ($\tilde{t} = 0.25, 0.5, 0.75$) in figures (4.2 and 4.3). All three models show gradual increase of the current and its slow rotation. Figure (4.2) shows that the rates of flow acceleration, the rotation of the current direction, the thickness of the boundary layer all differ substantially in the three models. However, the most profound difference becomes apparent in the profiles of second derivatives shown in figure (4.3).

The evolving current profiles with time invariably exhibit inflection point and, therefore, by virtue of the Rayleigh criterion, become linearly unstable. The emergence of inflection points in the current profiles $u(z,t)$ and $v(z,t)$ in all three models is illustrated in figure (4.3). At the sampled moments the profiles predicted by the model with time dependent eddy viscosity and the classical Ekman model exhibit a change of curvature sign for all sampled moments, which suggests strong essentially inviscid instability, while in the model with viscosity varying with time and depth inflection points develop only at later times not illustrated by the figure. The characteristics of the instabilities can be obtained only by solving numerically the Orr-Sommerfeld boundary value problem for each instant of time and for each model, which goes beyond the scope of this work. Usually, such inviscid instabilities have high growth

TABLE 4.1: Parameters of short scale instabilities for a sample transient Ekman current.

$\tilde{t}$	model of eddy viscosity	$\mathrm{Im}\,\omega$ (s^{-1})	k^* (m^{-1})
0.25	constant	2.37×10^{-5}	0.1
	time dependent	6.76×10^{-4}	0.03
0.5	constant	6.5×10^{-7}	0.03
	time dependent	2.58×10^{-5}	0.1
0.75	constant	1.1×10^{-6}	0.02
	time dependent	3.6×10^{-5}	0.06

rates and we can expect almost instant (compared to the inertial timescale) development of larger vortices in the already turbulent flow. Here, we confine ourselves to addressing the most basic questions about these instabilities: (i)Are the instabilities robust or sensitive to the employed viscosity model? (ii) What are the most unstable the characteristic scales of perturbations and how they evolve? (iii) What are the most unstable directions and how they evolve? Are the instabilities important for the evolution of Ekman current? The answers, certainly not comprehensive, could be deduced from the results of numerical study of the boundary value problem which

are summarised in table (4.1), where the maximal growth rates $\mathrm{Im}\,\omega$ and the wave number k^* are given.

First, it is easy to see that the instabilities are very sensitive to the eddy viscosity model: the profiles obtained with the time and depth dependent viscosity proved to be stable (for the chosen moments), while the growth rates in the models with constant and time dependent viscosity differ by more than an order of magnitude. For the examined sample profiles the most unstable perturbations are propagating perpendicular to the wind and have characteristic wavelengths of the order of a hundred meters. In the example at hand the model with time dependent viscosity yields growth timescales which are much faster than the characteristic timescale of the unperturbed motion, and, therefore, the instability might completely change the evolution predicted by the exact solutions of the Navier-Stokes equations within the framework of the Ekman paradigm. In our samples the instabilities in the classical Ekman model with a constant viscosity proved to be much weaker, which could justify their neglect when we are interested only in a relatively short timesclaes of the order of a few hours, but not for timescales exceeding several days. The instabilities are certainly not confined to the regime of periodic wind. We will return to discussion of such instabilities in the next section, where we consider situations of gradual increase of unidirectional wind ending up with a plateau.

4.4.2 An increase of wind ending up with a plateau

Consider an increase of unidirectional wind ending up with a plateau with the surface shear stress in the form

$$U_{10} = U_{10}^0 \left(1 - e^{-t/\delta}\right), \quad \tau(t) = \tau_0\, H(t)\, u_*^2(t). \tag{4.12}$$

The specific details of the increase are not particularly important and therefore its specific form was chosen primarily for convenience, but the characteristic time scale is essential, we specify it by parameter δ. A few examples of the evolution of the Ekman current in infinitely deep and homogeneous ocean caused by a gradual increase

of wind are shown in figures (4.4). The evolution of the Ekman current is plotted for several values of wind increase timescale δ and for the same three models (time-depth dependent viscosity, viscosity dependent only on time and the classical Ekman model with constant viscosity). Figure (4.4) illustrates the evolution of the surface current (the magnitude and its direction with respect to the wind). Although the general pattern of the evolution is qualitatively similar in all cases: with increase of wind the magnitude of the surface current also increases with the same time scale, while its direction is being deflected to the right. The figure demonstrates the sensitivity of the response both to the timescale of the wind increase and the choice of the model. Although the magnitude of the surface current weakly depends on the timescale of the wind increase, its orientation with respect to the wind proved to be sensitive to this scale, the deflection is the smallest for the fastest growth of wind. The increase of the surface current is always followed by inertial oscillations which are most pronounced for the model with eddy viscosity dependent only on time, and the least pronounced for the model with the time and depth dependent viscosity. As might have been expected, the amplitude of the oscillations increases with decrease of the wind timescale δ. An unexpected feature of the surface current dynamics is significantly smaller deflection predicted by the the model with the time and depth dependent viscosity.

Note that the latitude dependence in the time-depth dependent model is relatively weak for such regimes: the rate of growth for the surface current does not depend on the latitude (when the time units are scaled with f), but the duration of the growth stage and, correspondingly, the eventual magnitude of the current slightly decrease with increase of the latitude; for example, if we consider a two hour gradual increase of wind from zero to 10 m/s then at $\tilde{t} = 20$ the magnitude of the current at the surface $|U(0)|$ is 0.28 m/s for twenty degrees, 0.264 m/s for forty five and 0.24 m/s for seventy degrees.

The most profound implications of the found solutions are concerned with the evolving current profiles caused by increasing wind: as in the case of periodic wind, the evolving profiles invariably exhibit inflection point and become linearly unstable. The emergence of the inflection point in the current profiles $u(z,t)$ and $v(z,t)$ in

all three models is illustrated in figure (4.5). Here we do not quantify the growth rates of these instabilities, which goes beyond the scope of this work. Usually, such instabilities have high growth rates and we can expect almost instant (compared to the inertial timescale) development of larger vortices in the already turbulent flow. Certainly, the adopted model where momentum is transferred by diffusion with the coefficient derived under steady conditions is no longer applicable for such situations. To our knowledge, none of the existing much more sophisticated models of turbulent closures employed for modelling the surface boundary layer dynamic can overcome this difficulty and its very existence has not been realised.

4.4.3 Switch-off of the wind, decaying turbulence

To reveal the main features of a wind decrease scenario, here we consider complete switch-off of the wind and assume the turbulence in the water to decay as free turbulence. The prevailing view is that free turbulence decays in a power-like manner, while there is no consensus regarding the exponent. We assume for simplicity the eddy viscosity $\nu_e(t)$ to be a function of time only,

$$\nu_e(t) = \nu_0 \left(\frac{t}{t_0}\right)^{-n} + \nu; \quad \frac{t}{t_0} \geq 1, \tag{4.13}$$

where n is an unspecified yet exponent and ν is molecular viscosity. Counterintuitively, taking molecular viscosity into account in this manner proves to be essential.

The momentum equation in this case remains the same Ekman equation,

$$\frac{\partial \boldsymbol{U}}{\partial t} + if\boldsymbol{U} = \nu_e(t)\frac{\partial^2 \boldsymbol{U}}{\partial z^2}, \tag{4.14}$$

where $\nu_e(t)$ is now given by (4.13). The boundary conditions differ from those employed in the previous cases.

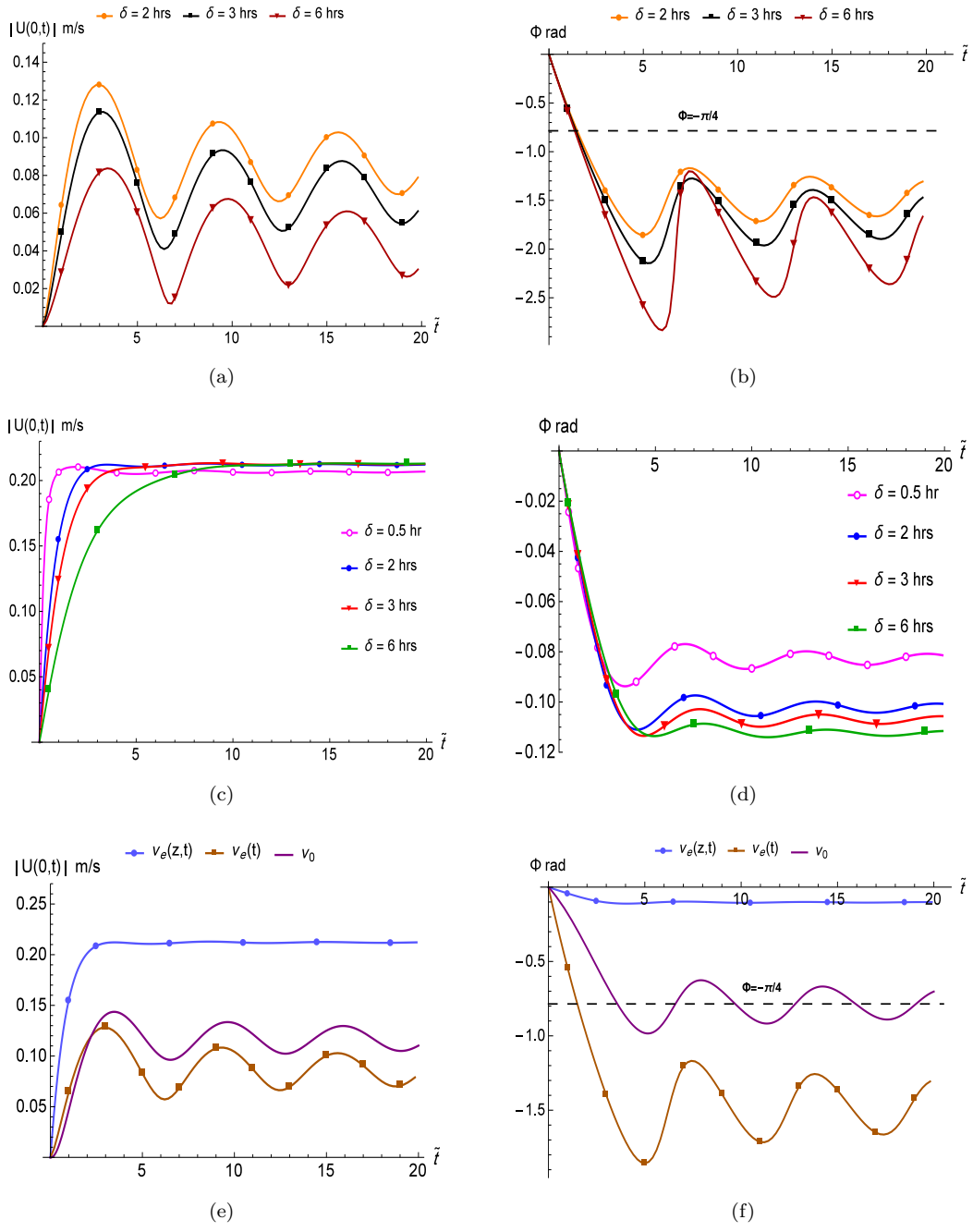

FIGURE 4.4: Evolution of the Ekman current under growing wind with different growth timesscales δ. The magnitude of the current surface velocity and the angle of its deflection from the wind: (a,b) for the time-dependent viscosity model, (c,d) for the time-depth dependent viscosity. (e,f) Comparison between the models with the time-dependent viscosity, time-depth dependent viscosity and the constant viscosity. The parameters and expressions for eddy viscosity are the same as in figure 4.1.

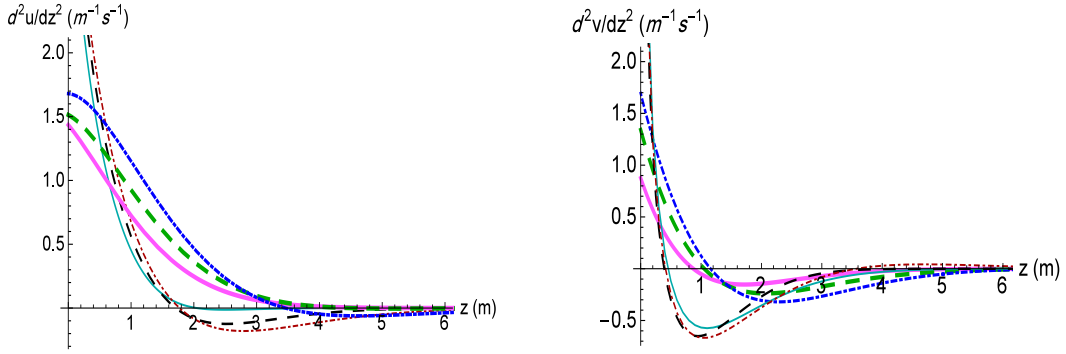

(a) (b)

FIGURE 4.5: The second derivative of the solution of the classical Ekman model (thick lines) and time-dependent viscosity model (thin lines) when $\delta = 3$ hrs and at different times: $\tilde{t} = 2$ (solid lines), $\tilde{t} = 3$ (dashed lines) and $\tilde{t} = 5$ (dotted lines). (a) The second derivative of x-component. (b) The second derivative of y-component. $f = 10^{-4}\mathrm{s}^{-1}$, $\nu_0 = 10^{-4}\mathrm{m}^2\mathrm{s}^{-1}$.

We assume that just before instantly switching off the wind at $t = t_0$ we had a steady Ekman current, that is $\boldsymbol{U}(z, t_0) = \boldsymbol{U}(z)$,

$$\boldsymbol{U}(z) = \frac{(1-i)\,\tau_0}{\rho\sqrt{2f\nu_0}}\,\exp\left[-(1+i)z\sqrt{\frac{f}{2\nu_0}}\right].$$

The natural boundary conditions after switch-off of the wind are the conditions of no stress at the surface and decay at infinity,

$$\frac{\partial \boldsymbol{U}}{\partial z} = 0 \quad \text{at} \quad z = 0, \qquad\qquad \boldsymbol{U}' \to 0 \quad \text{as} \quad z \to \infty. \tag{4.15}$$

The general solution of the Ekman equation (4.14) satisfying the boundary and initial conditions is

$$\boldsymbol{U}(z,t) = e^{-ift}\,\boldsymbol{W}(z,T), \tag{4.16a}$$

where,

$$\boldsymbol{W}(z,T) = \frac{-\tau_0\, e^{ift_0}}{\rho\,\nu_0\,\sqrt{\pi}} \left(e^{i\,f\,T/\nu_0} *_{(T)} \frac{e^{-z^2/4T}}{\sqrt{T}} \right) + \frac{(1-i)\,\tau_0\, e^{ift_0}}{\rho\,\sqrt{2f\nu_0}}\, e^{i\,f\,T/\nu_0}\, e^{-(1+i)z\sqrt{\frac{f}{2\nu_0}}}, \tag{4.16b}$$

and,

$$T = \int_{t_0}^{t} \left[\nu_0 \left(\frac{\xi}{t_0} \right)^{-n} + \nu \right] d\xi = \nu_0\, t_0^n \left[\frac{t^{-n+1} - t_0^{-n+1}}{-n+1} \right] + \nu(t - t_0);\ n > 1. \tag{4.16c}$$

Thus we have got a closed expression for evolving Ekman current $\boldsymbol{U}(z,t)$. Without wind the currents decays and generates decaying near-inertial oscillations. We will not dwell upon its depth-time evolution, just note a peculiar feature of the solution: unless $\nu \neq 0$, the downward diffusion of momentum stalls because the eddy viscosity decreases too fast. Taking into account molecular viscosity, i.e. assuming $\nu \neq 0$, eliminates this paradox.

Consider the current at the surface. For $\boldsymbol{U}(0,t)$ we get an explicit expression in terms of error functions

$$\boldsymbol{U}(0,t) = e^{-ift}\, \boldsymbol{W}(0,T), \tag{4.17a}$$

where

$$\boldsymbol{W}(0,T) = \frac{e^{-i\pi/4}\,\tau_0\, e^{if(t_0+T/\nu_0)}}{\rho\,\sqrt{f\nu_0}} \left[1 - \operatorname{erf}\left(\sqrt{\frac{ifT}{\nu_0}} \right) \right] = \frac{e^{-i\pi/4}\,\tau_0\, e^{if(t_0+T/\nu_0)}}{\rho\,\sqrt{f\nu_0}} \operatorname{erfc}\left(\sqrt{\frac{ifT}{\nu_0}} \right). \tag{4.17b}$$

Here, $\operatorname{erf} x = (2/\sqrt{\pi}) \int_0^x e^{-x'^2} dx'$ and $\operatorname{erfc} x = 1 - \operatorname{erf} x$ are the Gauss error function and complementary error function (e.g. Abramowitz and Stegun [1964]) and $T(t)$ is specified by (4.16c).

For large t ($t \gg t_0$), $T(t)$ can be simplified to

$$T = \frac{\nu_0 t_0}{n-1} + \nu\, t. \tag{4.18}$$

Then,

$$\boldsymbol{U}(0,t) = e^{-ift}\left(\frac{e^{-i\pi/4}\,\tau_0}{\rho\sqrt{f\nu_0}}\,\exp\left[if\left(\frac{nt_0}{n-1}+\frac{\nu t}{\nu_0}\right)\right]\operatorname{erfc}\left(\sqrt{if\left(\frac{t_0}{n-1}+\frac{\nu t}{\nu_0}\right)}\right)\right) \tag{4.19}$$

Since $\nu_0 \gg \nu$, we retain the terms with ν_0 despite the inequality $t \gg t_0$.

For arbitrary times the Ekman flux decays as

$$\boldsymbol{S} = \frac{e^{-i\pi/2}\tau}{\rho f}\,e^{if(t+t_0)}. \tag{4.20}$$

When ν_e is a constant, the Ekman flux is equal to $e^{-i\pi/2}\tau_0 e^{ift}/\rho f$ (Gonella [1971]).

4.5 Time-dependent viscosity model with $g(z) = \nu_0(1+z/\bar{\delta})^\mu$ and finite depth

Although linear dependence of eddy viscosity on depth we adopted in the previous sections is supported by both naive translation of the wall layer ideology and large eddy simulations by Zikanov et al. [2003], the observations in the ocean often reveal a more complicated picture. There is a number of studies which reports observations of a logarithmic layer near the surface as a universal phenomenon (e.g. Csanady [2001]), while the other authors report a more complicated picture (e.g. Kudryavtsev et al. [2008]) and some more complicated empirical parameterisations of $\nu_e(z)$ were put forward (e.g. Large et al. [1994]). It is not clear whether the aggregated data were controlled for the absence of solar heating and night convection which violate our basic assumptions. Anyway, in the oceanographic community there is a need in nonlinear parameterisations of $\nu_e(z)$, especially for the finite depth situations. Here, we generalise our previous results by considering a wider class of separable profiles,

$$\nu_e(z,t) = \tilde{\nu}_{e1}(t)\left[\nu_0(1+z/\bar{\delta})^\mu\right], \quad (\mu > 0), \tag{4.21}$$

where $\bar{\delta}$ is a real constant. For viscosity constant in time the problem was thoroughly examined by Jordan and Baker [1980]. Here, employing their results we obtain solutions for the time and depth dependent profiles given by (4.21). Since nonlinear parametrizations of $\nu_e(z)$ are more likely to be encountered in finite depth situations, here, in contrast to the rest of the paper, we consider fluid of finite depth D.

On using substitution (4.10a) and by taking the Laplace transform with respect to T ($\mathcal{L}\{\boldsymbol{W}(T)\} = \hat{\boldsymbol{W}}(s)$), the Ekman equation (1.22) becomes:

$$\frac{d}{dz}\left(g(z)\frac{d\hat{\boldsymbol{W}}}{dz}\right) - s\hat{\boldsymbol{W}} = 0, \quad \hat{\boldsymbol{W}}(z,s) = \int_0^\infty \boldsymbol{W}(z,T)e^{-sT}dT, \tag{4.22}$$

where $g(z) = \nu_0(1 + z/\bar{\delta})^\mu$, ν_0 and μ are positive constants and $\bar{\delta}$ is a real constant. Its general solution is (Jordan and Baker [1980]):

$$\hat{\boldsymbol{W}}(z,s) = \mathtt{S}^{(1/2)[(1-\mu)/(1-\mu/2)]}\left(c_1 J_\sigma(i\mathtt{S}\sqrt{s}) + c_2 N_\sigma(i\mathtt{S}\sqrt{s})\right); \tag{4.23}$$

with

$$\mathtt{S} = \nu_0^{-1/2}\left|\frac{\bar{\delta}}{1-\mu/2}\right|(1 + z/\bar{\delta})^{1-\mu/2} \tag{4.24}$$

where $J_{\tilde{\sigma}}$ and $N_{\tilde{\sigma}}$ are the Bessel and Neumann functions of order $\tilde{\sigma} = \frac{1}{2}\left|\frac{1-\mu}{1-\mu/2}\right|$.

Using the identities (e.g. Abramowitz and Stegun [1964])

$$xJ'_{\tilde{\sigma}}(x) \pm \tilde{\sigma}J_{\tilde{\sigma}}(x) = \pm xJ_{\tilde{\sigma}\mp 1}(x)$$
$$xN'_{\tilde{\sigma}}(x) \pm \tilde{\sigma}N_{\tilde{\sigma}}(x) = \pm xN_{\tilde{\sigma}\mp 1}(x),$$

the surface boundary condition

$$g(0)\,\hat{\boldsymbol{W}}'(0,s) = \hat{\boldsymbol{F}}(s), \;\; \hat{\boldsymbol{F}}(s) = \mathcal{L}\left\{-e^{ift(T)}\boldsymbol{\tau}(t(T))/(\rho\,\tilde{\nu}_{e1}(t(T)))\right\},$$

becomes

$$\pm(-s)^{\pm\tilde{\sigma}/2}\nu_0^{1\mp\tilde{\sigma}}\left(\frac{\bar{\delta}}{1-\mu/2}\right)\left|\frac{\bar{\delta}}{1-\mu/2}\right|^{-2\pm2\tilde{\sigma}}\zeta(0)^{1\mp\tilde{\sigma}}\left[c_1J_{\tilde{\sigma}\mp1}(\zeta(0))+c_2N_{\tilde{\sigma}\mp1}(\zeta(0))\right]=\hat{\boldsymbol{F}}(s), \tag{4.25}$$

where

$$\zeta(z)=i\left(\frac{s}{\nu_0}\right)^{1/2}\left|\frac{\bar{\delta}}{1-\mu/2}\right|(1+z/\bar{\delta})^{1-\mu/2}. \tag{4.26}$$

The no slip boundary condition at the bottom $z=D$, $\left(\hat{\boldsymbol{W}}(D,s)=0\right)$, requires

$$c_1J_{\tilde{\sigma}}(\zeta(D))+c_2N_{\tilde{\sigma}}(\zeta(D))=0. \tag{4.27}$$

The constants c_1 and c_2 are found by solving equations (4.25) and (4.27), which yields

$$c_1=\frac{-N_{\tilde{\sigma}}(\zeta(D))}{J_{\tilde{\sigma}}(\zeta(D))}\left[\frac{\boldsymbol{G}}{-N_{\tilde{\sigma}}(\zeta(D))J_{\tilde{\sigma}\mp1}(\zeta(0))/J_{\tilde{\sigma}}(\zeta(D))+N_{\tilde{\sigma}\mp1}(\zeta(0))}\right] \tag{4.28}$$

$$c_2=\frac{\boldsymbol{G}}{-N_{\tilde{\sigma}}(\zeta(D))J_{\tilde{\sigma}\mp1}(\zeta(0))/J_{\tilde{\sigma}}(\zeta(D))+N_{\tilde{\sigma}\mp1}(\zeta(0))}, \tag{4.29}$$

where

$$\boldsymbol{G}=\frac{\hat{\boldsymbol{F}}(s)}{\pm(-s)^{\pm\tilde{\sigma}/2}\,\nu_0^{1\mp\tilde{\sigma}}\,\left(\frac{\bar{\delta}}{1-\mu/2}\right)\left|\frac{\bar{\delta}}{1-\mu/2}\right|^{-2\pm2\tilde{\sigma}}\,\zeta(0)^{1\mp\tilde{\sigma}}}. \tag{4.30}$$

In the original variables the general solution of the Ekman equation (1.22) takes the form,

$$\boldsymbol{U}(z,t)=e^{-ift}\boldsymbol{W}(z,T);\quad T=\int_0^t\tilde{\nu}_{e1}(\xi)d\xi,\quad \boldsymbol{W}(z,T)=(1/2\pi i)\int_{c-i\infty}^{c+i\infty}\hat{\boldsymbol{W}}(z,s)e^{sT}ds, \tag{4.31}$$

where $c\geq0$.

We cannot claim that the solutions obtained in this section are better in describing reality than those obtained in the previous sections, since we do not have data

controlled for the absence of the factors not considered accounted in the model. However, at the very least these results extend the spectre of possibilities in modelling of Ekman currents.

4.6 Stokes-Ekman layer in model with time and depth dependent eddy viscosity

The picture of the ocean Ekman current dynamics outlined above does not take into account the ubiquitous surface waves, whenever there is wind wind waves are always present. Their account can essentially modify the Ekman current dynamics compared to the classical Ekman model, as was first suggested by Huang [1979]. The effect of the wave induced Stokes drift on Ekman currents was examined in a substantial number of works (see e.g. McWilliams et al. [1997], Lewis and Belcher [2004], Xu and Bowen [1994], Polton et al. [2005], Ardhuin et al. [2009], Sullivan and McWilliams [2010]), it has been confirmed that this effect can be indeed essential: the deflection of the current from the wind direction was found to be strongly affected (McWilliams et al. [1997], Lewis and Belcher [2004]). However in the literature the consideration was confined to somewhat oversimplified models. In particular, the eddy viscosity was assumed to be either constant (both in space and time) and isotropic, or constant in time and linearly varying with depth (Lewis and Belcher [2004]), while the wave spectrum was often modelled by a single harmonic, crucially, the Stokes drift dynamics caused by wave field evolution was ignored. As we discussed earlier, in reality, it is questionable to assume the eddy viscosity to be constant, it is even more questionable to consider Ekman currents subjected to variable winds while assuming the Stokes drift to be constant. In this section we consider how the account of the time dependent Stokes drift with realistic vertical profile could be incorporated into the picture of Ekman current dynamics without these too restrictive assumptions.

With account of the Stokes drift the horizontal momentum "Stokes-Ekman" equations take the form (e.g. Xu and Bowen [1994], Sullivan and McWilliams [2010]),

$$\frac{\partial \boldsymbol{U}}{\partial t} + if(\boldsymbol{U} + \boldsymbol{U}_s) = \frac{\partial}{\partial z}\left(\nu_e(z,t)\frac{\partial \boldsymbol{U}}{\partial z}\right). \tag{4.32}$$

where $\boldsymbol{U}_s = U_s(z,t)\,\boldsymbol{e}_U$ is the Stokes drift due to surface waves as a function of time and depth, $\boldsymbol{e}_U$ is unit vector in the mean direction of wave propagation (not necessarily coinciding with the direction of wind), the rest of the notations we retain from the previous sections: $\boldsymbol{U} = U(z,t)+iV(z,t)$, $\nu_e = \nu_e(z,t)$. To leading order the Stokes drift is provided by integration in the wavevector space over all wavevectors of the wave spectrum:

$$\boldsymbol{U}_s(z,t) = \frac{1}{(2)}\int_0^{\omega_c}\int_0^{2\pi} \omega \boldsymbol{k}(\omega,\theta)E(\omega,\theta,t)e^{-2|\boldsymbol{k}|z}d\omega d\theta, \tag{4.33}$$

where $E(\omega,\theta,t)$ is the directional energy spectrum presumed to be given in our context, ω is frequency of a monochromatic wave component with a wavevector $\boldsymbol{k}$, ω_c is a cut-off frequency; the specific choice of the cut-off scale is of little significance. Strictly speaking the z-dependence of each spectral component is not exponential, as is well known from available solutions of the boundary value problem for waves upon a sheared current (e.g. Kirby and Chen [1989]). The usually neglected $O(\boldsymbol{kU}|_{(z=0)}/\omega)$ correction depends on the profile and direction of the Ekman current. The neglect of this dependence of surface mode vertical structure on the boundary layer profile decouples $\boldsymbol{U}_s$ from $\boldsymbol{U}(z,t)$ and dramatically simplifies the problem. Although here we follow the line and neglect the effect of the Ekman current on the mode structure, we note that in doing so we are neglecting a wave-current interaction mechanism which might prove important in a different context. In contrast to local ocean response in the classical Ekman models, the time dependence of the directional wave spectrum $E(\omega,\theta,t)$ is determined not by the local wind but by a long history of wind over a large area. Here, assuming it to be known from a wave model, we just note that the characteristic timescales of $\boldsymbol{U}_s$ could be either comparable to characteristic timescales of wind variability or exceed them.

It is convenient to rewrite equation (4.32) as a the standard homogeneous Ekman equation with a right-hand side due to the Stokes drift,

$$\frac{\partial \boldsymbol{U}}{\partial t} + if\boldsymbol{U} - \frac{\partial}{\partial z}\left(\nu_e(z,t)\frac{\partial \boldsymbol{U}}{\partial z}\right) = -i\,f\,\boldsymbol{U}_s(z,t)\,. \tag{4.34}$$

The term ifU_s is often referred to as the "Coriolis-Stokes forcing". The motions are subjected to the same boundary conditions given by (1.23,1.25). Similarly to §3.1, by assuming separability of the eddy viscosity and using the substitution:

$$\boldsymbol{U}(z,t) = e^{-ift}\,\boldsymbol{W}(z,T)\,; \quad (T = \int_0^t \tilde{\nu}_{e1}(\xi)d\xi\,, \nu_e(z,t) = \nu_{e1}(t)\,g(z)), \tag{4.35}$$

we rewrite the Ekman equation (4.34) as an inhomogeneous equation with time and depth dependent right-hand side which we denote as $\boldsymbol{F}_1(z,t)$,

$$\frac{\partial \boldsymbol{W}}{\partial T} - \frac{\partial}{\partial z}\left(g(z)\frac{\partial \boldsymbol{W}}{\partial z}\right) = \frac{-if\,\boldsymbol{U}_s(z,t(T))}{\tilde{\nu}_{e1}(t(T))} \equiv \boldsymbol{F}_1(z,T)\,. \tag{4.36}$$

Taking the Laplace transform with respect to T ($\mathcal{L}\{\boldsymbol{W}(T)\} = \hat{\boldsymbol{W}}(s)$) yields

$$\frac{d}{dz}\left(g(z)\frac{d\hat{\boldsymbol{W}}}{dz}\right) - s\hat{\boldsymbol{W}} = -\hat{\boldsymbol{F}}_1(z,s)\,. \tag{4.37}$$

For simplicity only, here, we confine ourselves to linear $g(z)$: $g(z) = g_1(z+z_0)$. More general separable profiles (4.21) could be handled similarly. The general solution is a sum of the general solution of the homogeneous equation $\hat{\boldsymbol{W}}_h(z,s)$ derived in §(3.1) and given by (4.5), and a particular solution $\hat{\boldsymbol{W}}_p(z,s)$ of equation (4.37), thus,

$$\hat{\boldsymbol{W}}(z,s) = \hat{\boldsymbol{W}}_h(z,s) + \hat{\boldsymbol{W}}_p(z,s)\,. \tag{4.38}$$

Since the fundamental solutions of the homogeneous equation are known, it is straightforward to find a particular solution of the inhomogeneous equation

$$\frac{d^2\hat{\boldsymbol{W}}}{dz^2} + \frac{1}{z+z_0}\frac{d\hat{\boldsymbol{W}}}{dz} - \frac{s}{g_1(z+z_0)}\hat{\boldsymbol{W}} = \frac{-\hat{\boldsymbol{F}}_1(z,s)}{g_1(z+z_0)}\,, \tag{4.39}$$

expressed in terms of modified Bessel functions I_0 and K_0

$$\hat{\boldsymbol{W}}_p = \frac{2}{g_1}\int_0^z \hat{\boldsymbol{F}}_1(\chi,s)\Bigg(- I_0\left[2\sqrt{\frac{(z+z_0)s}{g_1}}\right]\, K_0\left[2\sqrt{\frac{(\chi+z_0)s}{g_1}}\right] + K_0\left[2\sqrt{\frac{(z+z_0)s}{g_1}}\right]\, I_0\left[2\sqrt{\frac{(\chi+z_0)s}{g_1}}\right]\Bigg)\, d\chi\,. \tag{4.40}$$

Then, the general solution satisfying the lower boundary condition ($\hat{\boldsymbol{W}} \to 0 \quad \text{as} \quad z \to \infty$) becomes,

$$\hat{\boldsymbol{W}}(z,s) = K_0\left[2\sqrt{\frac{(z+z_0)s}{g_1}}\right]\left(c_2 + (2/g_1)\int_0^z \hat{\boldsymbol{F}}_1(\chi,s)\, I_0\left[2\sqrt{\frac{(\chi+z_0)s}{g_1}}\right]\, d\chi\right)\,. \tag{4.41}$$

The arbitrary constant c_2 is specified by the boundary condition at the surface $z = 0$. To this end the first derivative of the found general solution

$$\frac{d\hat{\boldsymbol{W}}}{dz} = \frac{2}{g_1}\, I_0\left[2\sqrt{\frac{(z+z_0)s}{g_1}}\right]\, K_0\left[2\sqrt{\frac{(z+z_0)s}{g_1}}\right]\, \hat{\boldsymbol{F}}_1(z,s) - \frac{\sqrt{s}}{\sqrt{g_1\,(z+z_0)}}\, K_1\left[2\sqrt{\frac{(z+z_0)s}{g_1}}\right]\left(c_2 + (2/g_1)\int_0^z \hat{\boldsymbol{F}}_1(\chi,s)\, I_0\left[2\sqrt{\frac{(\chi+z_0)s}{g_1}}\right]\, d\chi\right) \tag{4.42}$$

is substituted into the boundary condition at the surface ($\hat{\boldsymbol{W}}'(0,s) = \hat{\boldsymbol{G}}_1(s)$), which yields a closed expression for c_2:

$$c_2 = \frac{\sqrt{g_1 z_0}}{\sqrt{s}\, K_1\left[2\sqrt{\frac{sz_0}{g_1}}\right]}\left(\frac{2}{g_1}\, I_0\left[2\sqrt{\frac{sz_0}{g_1}}\right]\, K_0\left[2\sqrt{\frac{sz_0}{g_1}}\right]\, \hat{\boldsymbol{F}}_1(0,s) - \hat{\boldsymbol{G}}_1(s)\right)\,. \tag{4.43}$$

Finally, we can now express the solution in terms of the original variables by taking the inverse Laplace transform as follows:

$$\boldsymbol{U}(z,t) = e^{-ift}\,\boldsymbol{W}(z,T)\,;\; T = \int_0^t \tilde{\nu}_{e1}(\xi)d\xi\,, \tag{4.44}$$

where

$$\boldsymbol{W}(z,T) = \frac{1}{2\pi\, i}\int_{c-i\infty}^{c+i\infty} \hat{\boldsymbol{W}}(z,s)\, e^{sT}\, ds; \quad c \geq 0; \tag{4.45}$$

$$\tag{4.46}$$

with $\hat{\boldsymbol{W}}(z,s)$ and c_2: given by (4.42) and (4.43). More general separable profiles (4.21) could be handled similarly. Note, that for applying the obtained formulae the time dependence of the Stokes drift has to be prescribed, to this end one needs to know the history of evolution of wave spectra over a considerable area. For example, if we are interested in describing Ekman currents dynamics on time scales of, say, 10h and 10 days, we would need to model evolution of wave spectra over fetches of about $4 \cdot 10^2$ and 10^4 km and know the wave spectra history over 10h and 10 days respectively. Since wave modelling on such a scale is rouinely carried out by global and regional wave models, therefore it is tempting to add an Ekman current block to wave models. Wave spectra evolution is in its turn affected by Ekman currents, a better description of these currents would help in improving wave modelling.

4.7 Concluding remarks

Our main conclusions could be briefly summarized as follows. We showed that the Ekman theory could be easily extended to take into account time and depth dependent eddy viscosity, which is expected to be a better reflection of reality. Under the assumption of an arbitrary power law depth dependence of eddy viscosity and arbitrary time dependence of wind we found exact general solution to the Navier-Stokes equations with time and depth dependent viscosity which describes dynamics of the Ekman boundary layer in terms of the Green's function. This novel class of exact solutions to the Navier-Stokes equations is of independent interest. An examination of the basic scenarios demonstrates that taking into account both depth and time dependence of eddy viscosity leads to substantial changes in the Ekman current response. Under the adopted Zikanov et al. [2003] parametrization of eddy viscosity we found also considerable dependence of the response on latitude.

The results were further extended for the Ekman currents under variable winds taking into account the time and depth dependent Stokes drift created by evolving wave spectra. General solution of the corresponding Stokes-Ekman equations has been derived to fill the gap in the existing literature. Possibilities of coupling of existing wave models with the Stokes-Ekman equations and unaccounted yet mechanisms of coupling were also discussed.

Since in nature the eddy viscosity does depend on time (although the dependence might be more complicated than the simplest u_*^2 scaling we adopted), there is a potential for extension of this approach by considering nonlocal relations between wind and eddy viscosity. We did not attempt a comparison with data. The fact that our solutions for time dependent linear in depth viscosity predict noticeably smaller surface current deflection to the wind direction, which better agrees with the observations, seems encouraging. An unexpected outcome from the analysis of Ekman currents forced by varying wind is that that the solutions rarely resemble the steady state solutions, even if the wind is varying slowly.

The characteristic timescales of the transient Ekman currents are of the order of inertial period for any model of viscosity, which is comparable to the period of the Earth rotation and is much smaller than spin up timescale. The transient Ekman timescales increase with increase of viscosity. Under any circumstance the Ekman response timescales are much larger than the periods of wind gusts. On the other hand, the time of wind increase in a storm or hurricane could be comparable to the transient Ekman timescale.

Our most surprising and, we believe, significant finding is that of major limitations of the applicability of the Ekman type models and all their generalizations used for modelling of the oceanic surface boundary layer under varying wind conditions. To our knowledge these limitations have not been discussed in the literature. Subjected to growing or turning wind the Ekman current response develops profiles unstable with respect to inviscid inflectional instability. Although a detailed examination of these instabilities is beyond the scope of the present work, we did consider a few examples. We found that the instabilities are small scale (with wavelengths

$\sim 10^2$ m) and very sensitive to the adopted model of eddy viscosity. Crucially, the instabilities could be fast compared to the inertial time scale and comparable to the characteristic timescales of Ekman current evolution. This raises questions about the fundamentals of the Ekman type models. When such instabilities occur we could expect dramatically enhanced "spike" mixing (compared to the models assuming merely diffusion of momentum) in the corresponding parts of the water column. Thus, we could expect two-scale mixing characterised by widely separated temporal scales: "normal" diffusion of momentum and a "spike mixing" caused by the inflectional instabilities. The fast evolving part of the current profile is expected to reach stable configuration at the timescale of instability, then only the slow evolution of the current will continue, until the varying wind creates another instance of strongly unstable inflectional profile. An immediate implication of this new qualitative picture is that a gusty wind should produce a broader boundary layer than a smooth wind of comparable strength. The occurrence of such strong instabilities of transient Ekman currents undermines the very existence of the Ekman paradigm. In principle, it might be possible to interpret Ekman models only in a coarse grain sense (averaging over certain time and spatial scales and using bulk viscosity). For example, the presence of Langmuir circulations which breaks down the key assumption of horizontal isotropy of eddy viscosity is dealt with by considering non-diagonal tensor of Reynolds stresses Wirth [2010]. However, at present it is not clear how to apply such an averaging and how the scale of averaging is linked to parameters of Langmuir circulations. This example is aimed to highlight general lack of clarity regarding the scales of spatial and temporal averaging implicit in the Ekman type models. We conclude that the established Ekman paradigm needs a radical revision. The present work has just highlighted the problem, the issue certainly needs a dedicated study and will be further explored elsewhere.

Chapter 5

Conclusions and Discussion

5.1 Conclusions

1. In the literature the Ekman current response to varying winds was studied under the Boussinesq hypothesis and assuming constant in time eddy viscosity with various simple dependencies on depth. Here, explicit exact general solution of the Navier-Stokes equations in terms of the Green's function describing response of infinitely deep non-stratified ocean to an arbitrary time dependent wind has been derived under the assumption of constant in time eddy viscosity with a vertical profile obtained by Zikanov et al (2003) by Large Eddy Simulations (LES) method. A thorough comparison with the available models employing more simple eddy viscosity profiles lacking the LES validation has been carried out. The range of situations where much simpler models can be used with acceptable accuracy has been identified.

2. A fundamental open question on how the vertical profile of stratification affects the surface current caused by wind varying in time has been examined within the framework of a two-layer Ekman model with uniform turbulent upper layer adjacent to the rigid lid surface and an infinitely deep stratified layer with much

smaller eddy viscosity. Within the framework of this idealized model of upper ocean with pronounced seasonal stratification, it has been found under what conditions the surface velocity vector is noticeably affected by the presence of seasonal stratification. The parameter controlling whether the presence of stratification will manifest itself on the surface is the nondimensional thickness of the mixed layer $\tilde{d} = d/\delta_{e1}$, ($\delta_1 = \sqrt{2\nu_{e1}/f}$), where ν_{e1} is the eddy viscosity in the mixed layer. For the stratification to have visible effects on the ocean surface nondimensional thickness should not exceed 1.5. Under strong winds the Ekman currents always feel the seasonal stratification for any depth of the mixed layer. It has been found that under these conditions the surface velocity field is quite sensitive to the depth of the mixed layer, but is much less sensitive to the strength of stratification. Under the hurricane winds the Ekman current shears at the bottom of the mixed layer become so strong, that the adopted model becomes inapplicable, the interface becomes unstable, an entrainment of stratified fluid and widening of the mixed layer occurs. These processes are not captured by the adopted simplest model, but the results suggest the way of how to generalise the model to capture them. From the perspective of potential for remote sensing of the characteristics of stratification it has been found that the use of HF radars utilizing the main and the second harmonics peaks in the Doppler spectra of scattered electromagnetic field opens new possibilities.

3. A novel extension of the Ekman model has been proposed and examined. In contrast to all other theoretical studies eddy viscosity was considered as function of both time and depth. Explicit exact general solution of the Navier-Stokes equations describing response of infinitely deep non-stratified ocean to an arbitrary time dependent wind has been derived. The basic scenarios (sharp increase of wind, periodic wind and wind switch-off) have been analysed in detail. It has been shown that taking into account time dependence of eddy viscosity significantly affects dynamics of the Ekman currents.

4. It has been found that in all the models the transient Ekman current caused by an arbitrary time dependent wind evolves in such a way that it becomes unstable with respect to strong inviscid inflectional instabilities. Thus, the

exact solutions of the Navier-Stokes equations we found proved to be unstable. The emergence of instabilities breaks down the key assumption of a smooth transfer of momentum. Hence the very notion of eddy viscosity in this context has to be revisited and the spatial and temporal scales over which the averaging is taking place have to be rethought.

5. The surface wave induced Stokes drift was known to affect the Ekman currents in the simplest models. Here, the most general formulation of the Stokes-Ekman equations with an arbitrary time dependent spectrum of surface waves and time and depth dependent eddy viscosity has been analysed. The exact general solution of the Stokes-Ekman equations in terms of the Green's function has been derived for separable eddy viscosity profiles.

5.2 Discussion

To put our results into context, here we briefly discuss the broader picture and most promising directions of further research.

First, we very briefly formulate our main conclusions in plain words. We showed that the Ekman theory could be easily extended to take into account time and depth dependent eddy viscosity, which is expected to be a better reflection of reality. An examination of the basic scenarios demonstrated that taking into account both depth and time dependence of eddy viscosity leads to substantial changes in the Ekman current response. The Ekman theory was further extended by taking into account the time and depth dependent Stokes drift created by evolving wave spectra. General solutions of the corresponding Ekman and Stokes-Ekman equations have been derived. To the best of our knowledge this is also the first work where the effect of stratification on the Ekman layer dynamics has been examined. Within the framework of a simplified two-layer model the general solution in terms of the Green's function describing the Ekman response to time dependent wind has been derived

and thoroughly examined. Thus, from a narrow mathematical viewpoint the problem of describing the Ekman response to time dependent wind in both the density stratified and homogeneous ocean has been solved. However, to what extent these results can improve description of the Ekman current in the ocean remains to be investigated. We briefly discuss what lines of the presented research can and should be continued. There is also a number of open fundamental questions which we highlight.

It is not clear how good is the adopted parametrization of the time dependence of eddy viscosity. We have assumed it to be local in time and scaled it as u_*^2. It is certainly better than ignoring the time dependence, which is the common practice, but obviously this is an oversimplification, eddy viscosity in the whole water column cannot vary simultaneously. The issue has to be clarified by working with more sophisticated closure models and direct numerical simulations. Since in nature the eddy viscosity does depend on time (although the dependence is certainly more complicated than the simplest u_*^2 scaling we adopted), there is a potential for further extension of this approach by considering nonlocal in time relations between the wind and eddy viscosity. The same uncertainty regarding the true value of eddy viscosity applies to the Stokes-Ekman model as well. Assuming that our parametrization is valid for a certain range of timescales, the obtained solutions of the Stokes-Ekman model can be incorporated as block into one of the global or local wave models, taking into account the feedback of the resulting Ekman currents on wave evolution. An iterative procedure will be required. Technically the procedure is straightforward. This might improve modelling of both wave propagation and the Ekman current response.

The adopted consideration of density stratification where it manifests only through suppression of turbulence and reduced eddy viscosity is certainly oversimplified. Its decisive advantage is that it enables us to address the most basic questions on the range of parameters where the presence of stratification below the mixed layer can be observed on the ocean surface through its effect on surface current. This line of research seems to be very promising and can be pursued further by detailing the link between the stratification and the eddy viscosity in the stratified layer. Even

in its current simple form the model provides clear predictions which can be tested against the data. The model reveals what to expect and when, further elaboration of the model to improve the quantitative predictions is a possible line of research. The promising line we just outlined but didn't pursue within the framework of the same two-layer model is the possibility of intense mixing at the bottom of the mixed layer and the corresponding entrainment. This is of prime importance for tropical hurricane modelling, since entrainment of the colder heavier fluid cools the mixed layer and thus reduces the hurricane intensity.

Our most significant finding is that of major limitations of the applicability of the Ekman type models. To our knowledge the issue has never been discussed in the literature, although instabilities of steady Ekman currents were examined. Subjected to growing or turning wind the Ekman current response develops profiles unstable with respect to inviscid inflectional instability. Although a detailed examination of these instabilities is beyond the scope of the present work, we considered a few examples and found that the instabilities are small scale (with wavelengths $\sim 10^2$ m) and very sensitive to the adopted model of eddy viscosity. Crucially, the instabilities could be very fast compared to the inertial time scale and the characteristic timescales of Ekman current evolution, which are of the order of the inertial period. This raises questions about the fundamentals of the Ekman type models. When such instabilities occur we could expect dramatically enhanced "spike" mixing (compared to the models assuming merely diffusion of momentum) in the corresponding parts of the water column. Thus, we could expect two-scale mixing characterised by widely separated temporal scales: "normal" diffusion of momentum and a "spike mixing" caused by the inflectional instabilities. The fast evolving part of the current profile is expected to reach stable configuration at the timescale of instability, then only the slow evolution of the current will continue, until the varying wind creates another instance of strongly unstable inflectional profile. An immediate implication of this new qualitative picture is that a gusty wind should produce a broader boundary layer than a gradually varying wind of comparable strength. The second verifiable prediction is that in the instant measurements of vertical profiles of turbulence there

should be spots of much higher intensity. The spikes of turbulence in the subsurface layer were observed, but a thorough analysis is needed to claim that these spikes are indeed caused by the inflectional instabilities of transient Ekman currents.

The occurrence of such strong instabilities of transient Ekman currents undermines the very existence of the Ekman paradigm. It suggests that the Ekman models should be interpreted only in a coarse grain sense, i.e. as averaged over certain time and spatial scales. At present it is not clear what scales of averaging are needed. We conclude that the established Ekman paradigm needs a radical revision and view the issue of clarifying the scales of averaging as central. The study in this direction has to be continued. First, a more detailed study of the instabilities will be carried out, then direct numerical simulation will help in clarifying this fundamental question.

We didn't attempt a comparison with data. However we mention that our solutions for time dependent linear in depth viscosity predict noticeably smaller surface current deflection with respect to the wind direction, compared to models with constant in time viscosity. This behaviour better agrees with the observations, which seems encouraging, but might prove to be just a coincidence. A detailed comparison with observations is needed, which requires a dedicated work.

Bibliography

Milton Abramowitz and Irene A Stegun. *Handbook of mathematical functions: with formulas, graphs, and mathematical tables*, volume 55. Courier Corporation, 1964.

Fabrice Ardhuin, Louis Marié, Nicolas Rascle, Philippe Forget, and Aron Roland. Observation and estimation of lagrangian, stokes, and eulerian currents induced by wind and waves at the sea surface. *Journal of Physical Oceanography*, 39(11): 2820–2838, 2009.

Alexander Babanin. *Breaking and dissipation of ocean surface waves*. Cambridge University Press, 2011.

P Broche, P Forget, JC De Maistre, JL Devenon, and M Crochet. Vhf radar for ocean surface current and sea state remote sensing. *Radio Science*, 22(01):69–75, 1987.

Alexander HD Cheng, Paston Sidauruk, and Younane Abousleiman. Approximate inversion of the laplace transform. *Mathematica Journal*, 4(2):76–82, 1994.

TK Chereskin. Direct evidence for an ekman balance in the california current. *Journal of Geophysical Research: Oceans*, 100(C9):18261–18269, 1995.

Gary Neil Coleman, JH Ferziger, and PR Spalart. A numerical study of the turbulent ekman layer. *Journal of Fluid Mechanics*, 213:313–348, 1990.

Alex DD Craik and Sidney Leibovich. A rational model for langmuir circulations. *Journal of Fluid Mechanics*, 73(3):401–426, 1976.

Gabriel T Csanady. *Air-sea interaction: laws and mechanisms*. Cambridge University Press, 2001.

Benoit Cushman-Roisin and Jean-Marie Beckers. Introduction to geophysical fluid dynamics-physical and numerics aspects. 2007.

Eric A D'Asaro and Geoffrey T Dairiki. Turbulence intensity measurements in a wind-driven mixed layer. *Journal of physical oceanography*, 27(9):2009–2022, 1997.

Vagn Walfrid Ekman. On the influence of the earth's rotation on ocean-currents. 1905.

S Elipot and ST Gille. Ekman layers in the southern ocean: spectral models and observations, vertical viscosity and boundary layer depth. *Ocean Science Discussions*, 6(2), 2009.

A Gill. Atmospheric-ocean dynamics. *Int. Geophys. Ser.*, 30:662, 1982.

Joseph Gonella. A local study of inertial oscillations in the upper layers of the ocean. In *Deep Sea Research and Oceanographic Abstracts*, volume 18, pages 775–788. Elsevier, 1971.

Maricarmen Guerra and Jim Thomson. Turbulence measurements from 5-beam acoustic doppler current profilers. *Journal of Atmospheric and Oceanic Technology*, (2017), 2017.

Norden E Huang. On surface drift currents in the ocean. *Journal of Fluid Mechanics*, 91(1):191–208, 1979.

Alastair D Jenkins and John AT Bye. Some aspects of the work of vw ekman. *Polar Record*, 42(1):15–22, 2006.

Thomas F Jordan and James R Baker. Vertical structure of time-dependent flow dominated by friction in a well-mixed fluid. *Journal of Physical Oceanography*, 10 (7):1091–1103, 1980.

Kyung Tae Jung, Hyoun-Woo Kang, Ho Jin Lee, and Mi Kyung Kim. Ekman motion in shallow open sea in the presence of time-harmonic variation of water depth. *Continental shelf research*, 27(9):1287–1302, 2007.

James T Kirby and Tsung-Muh Chen. Surface waves on vertically sheared flows: approximate dispersion relations. *Journal of Geophysical Research: Oceans*, 94 (C1):1013–1027, 1989.

Gerbrand Johan Komen, Luigi Cavaleri, and Mark Donelan. *Dynamics and modelling of ocean waves*. Cambridge university press, 1996.

Vladimir Kudryavtsev, Victor Shrira, Vladimir Dulov, and Vladimir Malinovsky. On the vertical structure of wind-driven sea currents. *Journal of Physical Oceanography*, 38(10):2121–2144, 2008.

William G Large, James C McWilliams, and Scott C Doney. Oceanic vertical mixing: A review and a model with a nonlocal boundary layer parameterization. *Reviews of Geophysics*, 32(4):363–403, 1994.

S Leibovich and SK Lele. The influence of the horizontal component of earth's angular velocity on the instability of the ekman layer. *Journal of Fluid Mechanics*, 150: 41–87, 1985.

Sidney Leibovich. On the evolution of the system of wind drift currents and langmuir circulations in the ocean. part 1. theory and averaged current. *Journal of Fluid Mechanics*, 79(4):715–743, 1977a.

Sidney Leibovich. Convective instability of stably stratified water in the ocean. *Journal of Fluid Mechanics*, 82(3):561–581, 1977b.

Yueng Djern Lenn. Observations of antarctic circumpolar current dynamics in the drake passage and small-scale variability near the antarctic peninsula. 2006.

DM Lewis and SE Belcher. Time-dependent, coupled, ekman boundary layer solutions incorporating stokes drift. *Dynamics of Atmospheres and Oceans*, 37(4): 313–351, 2004.

Ole Secher Madsen. A realistic model of the wind-induced ekman boundary layer. *Journal of Physical Oceanography*, 7(2):248–255, 1977.

James C McWilliams, Peter P Sullivan, and Chin-Hoh Moeng. Langmuir turbulence in the ocean. *Journal of Fluid Mechanics*, 334:1–30, 1997.

Fridtjof Nansen. *The Norwegian North polar expedition, 1893-1896: scientific results*, volume 6. Longmans, Green and Company, 1905.

Jeffrey D Paduan and Hans C Graber. Introduction to high-frequency radar: reality and myth. *Oceanography*, 10(2):36–39, 1997.

Owen M Phillips. The dynamics of the upper ocean. 1977.

Jeff A Polton, David M Lewis, and Stephen E Belcher. The role of wave-induced coriolis–stokes forcing on the wind-driven mixed layer. *Journal of Physical Oceanography*, 35(4):444–457, 2005.

James F Price and Miles A Sundermeyer. Stratified ekman layers. *Journal of Geophysical Research: Oceans*, 104(C9):20467–20494, 1999.

James F Price, Robert A Weller, and Robert Pinkel. Diurnal cycling: Observations and models of the upper ocean response to diurnal heating, cooling, and wind mixing. *Journal of Geophysical Research: Oceans*, 91(C7):8411–8427, 1986.

James F Price, Robert A Weller, and Rebecca R Schudlich. Wind-driven ocean currents and ekman transport. In *Proceedings of the 20th International CosmicRay Conference (Nauka, Moscow, 1987)*, volume 1, page 236. JSTOR, 1987.

Fernando Santiago-Mandujano and Eric Firing. Mixed-layer shear generated by wind stress in the central equatorial pacific. *Journal of physical oceanography*, 20(10): 1576–1582, 1990.

Victor I Shrira and Philippe Forget. On the nature of near-inertial oscillations in the uppermost part of the ocean and a possible route toward hf radar probing of stratification. *Journal of Physical Oceanography*, 45(10):2660–2678, 2015.

Victor I Shrira, Dmitry V Ivonin, Pierre Broche, and Jean C Maistre. On remote sensing of vertical shear of ocean surface currents by means of a single-frequency vhf radar. *Geophysical research letters*, 28(20):3955–3958, 2001.

Gerold Siedler, John Gould, and John A Church. *Ocean circulation and climate: observing and modelling the global ocean*, volume 103. Academic Press, 2001.

Alexander Soloviev and Roger Lukas. *The near-surface layer of the ocean: structure, dynamics and applications*, volume 48. Springer Science & Business Media, 2013.

Harald Stehfest. Algorithm 368: Numerical inversion of laplace transforms [d5]. *Communications of the ACM*, 13(1):47–49, 1970.

Robert H Stewart. *Introduction to physical oceanography*. Robert H. Stewart, 2008.

Robert H Stewart and Joseph W Joy. Hf radio measurements of surface currents. In *Deep Sea Research and Oceanographic Abstracts*, volume 21, pages 1039–1049. Elsevier, 1974.

Peter P Sullivan and James C McWilliams. Dynamics of winds and currents coupled to surface waves. *Annual Review of Fluid Mechanics*, 42, 2010.

Harald Ulrich Sverdrup. Wind-driven currents in a baroclinic ocean; with application to the equatorial currents of the eastern pacific. *Proceedings of the National Academy of Sciences*, 33(11):318–326, 1947.

Calvin C Teague, John F Vesecky, and Zackariah R Hallock. A comparison of multifrequency hf radar and adcp measurements of near-surface currents during cope-3. *IEEE Journal of Oceanic Engineering*, 26(3):399–405, 2001.

EA Terray, MA Donelan, YC Agrawal, WM Drennan, KK Kahma, A JIII Williams, PA Hwang, and SA Kitaigorodskii. Estimates of kinetic energy dissipation under breaking waves. *Journal of Physical Oceanography*, 26(5):792–807, 1996.

John H Thomas. A theory of steady wind-driven currents in shallow water with variable eddy viscosity. *Journal of physical oceanography*, 5(1):136–142, 1975.

Quanrong Wang and Hongbin Zhan. On different numerical inverse laplace methods for solute transport problems. *Advances in Water Resources*, 75:80–92, 2015.

Wei Wang and Rui Xin Huang. Wind energy input to the ekman layer. *Journal of Physical Oceanography*, 34(5):1267–1275, 2004.

Jan Erik Weber. Ekman currents and mixing due to surface gravity waves. *Journal of Physical Oceanography*, 11(10):1431–1435, 1981.

Robert A Weller. Observations of the velocity response to wind forcing in the upper ocean. *Journal of Geophysical Research: Oceans*, 86(C3):1969–1977, 1981.

Robert A Weller and James F Price. Langmuir circulation within the oceanic mixed layer. *Deep Sea Research Part A. Oceanographic Research Papers*, 35(5):711–747, 1988.

Achim Wirth. On the ekman spiral with an anisotropic eddy viscosity. *Boundary-layer meteorology*, 137(2):327–331, 2010.

Alan J Witten and John H Thomas. Steady wind-driven currents in a large lake with depth-dependent eddy viscosity. *Journal of Physical Oceanography*, 6(1):85–92, 1976.

Lucy R Wyatt. Limits to the inversion of hf radar backscatter for ocean wave measurement. *Journal of Atmospheric and Oceanic Technology*, 17(12):1651–1666, 2000.

Zhigang Xu and AJ Bowen. Wave-and wind-driven flow in water of finite depth. *Journal of Physical Oceanography*, 24(9):1850–1866, 1994.

Rong-Hua Zhang and Stephen E Zebiak. Effect of penetrating momentum flux over the surface boundary/mixed layer in az-coordinate ogcm of the tropical pacific. *Journal of physical oceanography*, 32(12):3616–3637, 2002.

Oleg Zikanov, Donald N Slinn, and Manhar R Dhanak. Large-eddy simulations of the wind-induced turbulent ekman layer. *Journal of Fluid Mechanics*, 495:343–368, 2003.